The Astrophysical Journal Supplement Series, 238:19 (36pp), 2018 October https://doi.org/10.3847/1538-4365/aaceae

The VLA Nascent Disk and Multiplicity Survey of Perseus Protostars (VANDAM). IV. Free–Free Emission from Protostars: Links to Infrared Properties, Outflow Tracers, and Protostellar Disk Masses

Łukasz Tychoniec[1,2], John J. Tobin[1,3], Agata Karska[4], Claire Chandler[5], Michael M. Dunham[6,7], Robert J. Harris[8],
Kaitlin M. Kratter[9], Zhi-Yun Li[10], Leslie W. Looney[8], Carl Melis[11], Laura M. Pérez[11,12], Sarah I. Sadavoy[6,13],
Dominique Segura-Cox[8], and Ewine F. van Dishoeck[1,14]
[1] Leiden Observatory, Leiden University, P.O. Box 9513, NL-2300RA Leiden, The Netherlands; tychoniec@strw.leidenuniv.nl
[2] Astronomical Observatory, Faculty of Physics, Adam Mickiewicz University, Słoneczna 36, PL-60268 Poznań, Poland
[3] Homer L. Dodge Department of Physics and Astronomy, University of Oklahoma, 440 W. Brooks Street, Norman, OK 73019, USA
[4] Centre for Astronomy, Nicolaus Copernicus University in Toruń, Faculty of Physics, Astronomy and Informatics, Grudziadzka 5, PL-87100 Toruń, Poland
[5] National Radio Astronomy Observatory, P.O. Box O, 1003 Lopezville Road, Socorro, NM 87801-0387, USA
[6] Harvard-Smithsonian Center for Astrophysics, 60 Garden St., Cambridge, MA, USA
[7] Department of Physics, State University of New York Fredonia, Fredonia, NY 14063, USA
[8] Department of Astronomy, University of Illinois, Urbana, IL 61801, USA
[9] Department of Astronomy and Steward Observatory, University of Arizona, 933 N Cherry Ave, Tucson, AZ 85721, USA
[10] Department of Astronomy, University of Virginia, Charlottesville, VA 22903, USA
[11] Center for Astrophysics and Space Sciences, University of California, San Diego, CA 92093, USA
[12] Universidad de Chile, Departamento de Astronoma, Camino El Observatorio 1515, Las Condes, Santiago, Chile
[13] Max-Planck-Institut für Astronomie, Königstuhl 17, D-69117 Heidelberg, Germany
[14] Max-Planck Institut für Extraterrestrische Physik, Giessenbachstrasse 1, D-85748 Garching, Germany

Received 2018 March 22; revised 2018 June 5; accepted 2018 June 6; published 2018 October 1

Abstract

Emission from protostars at centimeter radio wavelengths has been shown to trace the free–free emission arising from ionizing shocks as a result of jets and outflows driven by protostars. Therefore, measuring properties of protostars at radio frequencies can provide valuable insights into the nature of their outflows and jets. We present a C-band (4.1 and 6.4 cm) survey of all known protostars (Class 0 and Class I) in Perseus as part of the VLA Nascent Disk and Multiplicity (VANDAM) Survey. We examine the known correlations between radio flux density and protostellar parameters, such as bolometric luminosity and outflow force, for our sample. We also investigate the relationship between radio flux density and far-infrared line luminosities from *Herschel*. We show that free–free emission most likely originates from J-type shocks; however, the large scatter indicates that those two types of emission probe different time and spatial scales. Using C-band fluxes, we removed an estimation of free–free contamination from the corresponding Ka-band (9 mm) flux densities that primarily probe dust emission from embedded disks. We find that the compact ($<1''$) dust emission is lower for Class I sources (median dust mass 96 $M_\oplus$) relative to Class 0 (248 $M_\oplus$), but several times higher than in Class II (5–15 $M_\oplus$). If this compact dust emission is tracing primarily the embedded disk, as is likely for many sources, this result provides evidence of decreasing disk masses with protostellar evolution, with sufficient mass for forming giant planet cores primarily at early times.

Key words: protoplanetary disks – radio continuum: stars – stars: formation – stars: protostars – stars: winds, outflows – techniques: interferometric

Supporting material: figure sets, machine-readable tables

1. Introduction

Stars are born through a collapse of cold cores of dust and gas, usually within molecular clouds. A significant fraction of the parental core material is, however, dispersed by powerful outflows and jets rather than incorporated into the protostar (e.g., Arce & Sargent 2006; Offner & Arce 2014). Both outflows and jets are key features observed in star-forming regions toward most young stellar objects (Frank et al. 2014). Outflow properties are expected to reflect the age and activity of the embedded protostar. For example, studies have shown that outflows decrease in force with protostellar evolution (e.g., Bontemps et al. 1996; Yıldız et al. 2015) and outflow ejection rates correlate with accretion onto the central protostar (e.g., Shu et al. 1994; Mottram et al. 2017). Those characteristics suggest that the earliest stages of star formation are essential to investigate because this is the period where stars accumulate most of their mass and are interacting most vigorously with the core and cloud by means of outflows.

Ejecta from the protostar can have different forms. Fast, supersonic jets are well-collimated and they interact with cold gas around the protostar in shock events. While likely consisting of atomic gas, it has been observed that they can also be composed of high-velocity molecular gas, especially in very young sources (e.g., Bachiller et al. 1990; Tafalla et al. 2004; Hirano et al. 2010). Molecules, however, are most frequently observed in the much wider and slower outflow, which contains more mass than a jet. The relationship between the outflow and the jet is still strongly debated, but there is a growing body of evidence, from both observations (e.g., Nisini et al. 2015; Dionatos & Güdel 2017) and simulations (e.g., Machida 2014), suggesting that the collimated jet is also powering the wide molecular outflow.

Table 1
Protostars of the VANDAM Survey

Name[a]	R.A.[b] (J2000)	Decl.[b] (J2000)	Field[c]	Detected 6.4 cm	Detected 4.1 cm	Class	L_{bol}[d] ($L_{\odot}$)	T_{bol}[d] (K)
Per-emb-1	03:43:56.805	+32:00:50.201	PerC31	Y	Y	0	1.8 ± 0.1	27.0 ± 1.0
Per-emb-2	03:32:17.927	+30:49:47.825	PerC23	Y	Y	0	0.9 ± 0.1	27.0 ± 1.0
Per-emb-3	03:29:00.574	+31:12:00.204	PerC37	Y	Y	0	0.5 ± 0.1	32.0 ± 2.0
Per-emb-4	03:28:39.101	+31:06:01.800	PerC12	⋯	⋯	0	0.2 ± 0.0	31.0 ± 3.0
Per-emb-5	03:31:20.938	+30:45:30.273	PerC24	⋯	Y	0	1.3 ± 0.1	32.0 ± 2.0
Per-emb-6	03:33:14.404	+31:07:10.714	PerC38	Y	Y	0	0.3 ± 0.0	52.0 ± 3.0
Per-emb-7	03:30:32.681	+30:26:26.480	PerC15	⋯	⋯	0	0.1 ± 0.1	37.0 ± 4.0
Per-emb-8	03:44:43.981	+32:01:35.210	PerC25	Y	Y	0	2.6 ± 0.5	43.0 ± 6.0
Per-emb-9	03:29:51.831	+31:39:05.904	PerC6	Y	Y	0	0.6 ± 0.1	36.0 ± 2.0
Per-emb-10	03:33:16.424	+31:06:52.063	PerC38	⋯	Y	0	0.6 ± 0.1	30.0 ± 2.0
Per-emb-11	03:43:57.064	+32:03:04.788	PerC2	Y	Y	0	1.5 ± 0.1	30.0 ± 2.0
Per-emb-12	03:29:10.536	+31:13:30.933	PerC35	Y	Y	0	7.0 ± 0.7	29.0 ± 2.0
Per-emb-13	03:29:12.015	+31:13:08.031	PerC35	Y	Y	0	4.0 ± 0.3	28.0 ± 1.0
Per-emb-14	03:29:13.547	+31:13:58.150	PerC35	Y	Y	0	0.7 ± 0.1	31.0 ± 2.0
Per-emb-15	03:29:04.054	+31:14:46.236	PerC8	Y	Y	0	0.4 ± 0.1	36.0 ± 4.0
Per-emb-16	03:43:50.978	+32:03:24.101	PerC2	⋯	⋯	0	0.4 ± 0.0	39.0 ± 2.0
Per-emb-17	03:27:39.104	+30:13:03.067	PerC20	Y	Y	0	4.2 ± 0.1	59.0 ± 11.0
Per-emb-18	03:29:11.258	+31:18:31.072	PerC37	Y	Y	0	2.8 ± 1.7	59.0 ± 12.0
Per-emb-19	03:29:23.497	+31:33:29.172	PerC4	Y	Y	0	0.4 ± 0.1	60.0 ± 3.0
Per-emb-20	03:27:43.276	+30:12:28.780	PerC20	Y	Y	0	1.4 ± 0.2	65.0 ± 3.0
Per-emb-21	03:29:10.668	+31:18:20.191	PerC18	⋯	⋯	0	6.9 ± 1.9	45.0 ± 12.0
Per-emb-22	03:25:22.409	+30:45:13.257	PerC13	Y	Y	0	3.6 ± 0.5	43.0 ± 2.0
Per-emb-23	03:29:17.211	+31:27:46.302	PerC7	Y	Y	0	0.8 ± 0.1	42.0 ± 2.0
Per-emb-24	03:28:45.297	+31:05:41.693	PerC12	⋯	Y	0	0.4 ± 0.0	67.0 ± 10.0
Per-emb-25	03:26:37.510	+30:15:27.805	PerC21	Y	Y	0	1.2 ± 0.0	61.0 ± 12.0
Per-emb-26	03:25:38.874	+30:44:05.283	PerC29	Y	Y	0	8.4 ± 1.5	47.0 ± 7.0
Per-emb-27	03:28:55.569	+31:14:37.025	PerC8	Y	Y	0	19.0 ± 0.4	69.0 ± 1.0
Per-emb-28	03:43:51.007	+32:03:08.042	PerC2	Y	Y	0/I	0.7 ± 0.1	45.0 ± 2.0
Per-emb-29	03:33:17.877	+31:09:31.816	PerC38	⋯	⋯	0/I	3.7 ± 0.4	48.0 ± 1.0
Per-emb-30	03:33:27.303	+31:07:10.159	PerC38	Y	Y	0/I	1.1 ± 0.0	93.0 ± 6.0
Per-emb-31	03:28:32.547	+31:11:05.151	PerC11	⋯	⋯	0/I	0.2 ± 0.0	80.0 ± 13.0
Per-emb-32	03:44:02.403	+32:02:04.734	PerC31	⋯	⋯	0/I	0.3 ± 0.1	57.0 ± 10.0
Per-emb-33	03:25:36.379	+30:45:14.727	PerC29	Y	⋯	0	8.3 ± 0.8	57.0 ± 3.0
Per-emb-34	03:30:15.162	+30:23:49.232	PerC28	⋯	Y	I	1.8 ± 0.1	88.0 ± 13.0
Per-emb-35	03:28:37.090	+31:13:30.787	PerC11	Y	Y	I	11.1 ± 0.3	85.0 ± 26.0
Per-emb-36	03:28:57.373	+31:14:15.772	PerC8	Y	Y	I	6.9 ± 1.0	85.0 ± 12.0
Per-emb-37	03:29:18.964	+31:23:14.304	PerC5	⋯	⋯	0	0.5 ± 0.1	22.0 ± 1.0
Per-emb-38	03:32:29.197	+31:02:40.759	PerC22	⋯	⋯	I	0.5 ± 0.0	115.0 ± 21.0
Per-emb-39	03:33:13.781	+31:20:05.204	PerC3	⋯	⋯	I	0.0 ± 0.1	125.0 ± 47.0
Per-emb-40	03:33:16.669	+31:07:54.901	PerC38	Y	Y	I	1.5 ± 1.0	132.0 ± 25.0
Per-emb-41	03:33:20.341	+31:07:21.354	PerC38	⋯	⋯	I	0.2 ± 0.4	157.0 ± 72.0
Per-emb-42	03:25:39.135	+30:43:57.908	PerC29	⋯	⋯	I	0.7 ± 0.8	163.0 ± 51.0
Per-emb-43	03:42:02.160	+31:48:02.080	PerC39	⋯	⋯	I	0.1 ± 0.1	176.0 ± 42.0
Per-emb-44	03:29:03.763	+31:16:03.808	PerC8	Y	Y	0/I	32.5 ± 7.1	75.0 ± 52.0
Per-emb-45	03:33:09.569	+31:05:31.192	PerC38	⋯	⋯	I	0.1 ± 0.1	197.0 ± 93.0
Per-emb-46	03:28:00.414	+30:08:01.013	PerC16	⋯	Y	I	0.3 ± 0.1	221.0 ± 7.0
Per-emb-47	03:28:34.507	+31:00:50.990	PerC19	⋯	Y	I	1.2 ± 0.1	230.0 ± 17.0
Per-emb-48	03:27:38.268	+30:13:58.448	PerC20	Y	Y	I	0.9 ± 0.0	238.0 ± 14.0
Per-emb-49	03:29:12.956	+31:18:14.306	PerC18	Y	Y	I	1.1 ± 0.7	239.0 ± 68.0
Per-emb-50	03:29:07.768	+31:21:57.128	PerC10	Y	Y	I	23.2 ± 3.0	128.0 ± 23.0
Per-emb-51	03:28:34.536	+31:07:05.520	PerC12	⋯	⋯	I	0.1 ± 0.1	263.0 ± 115.0
Per-emb-52	03:28:39.699	+31:17:31.882	PerC9	⋯	⋯	I	0.2 ± 0.2	278.0 ± 119.0
Per-emb-53	03:47:41.591	+32:51:43.672	PerC26	Y	Y	I	4.7 ± 0.9	287.0 ± 8.0
Per-emb-54	03:29:01.548	+31:20:20.497	PerC10	Y	Y	I	16.8 ± 2.6	131.0 ± 63.0
Per-emb-55	03:44:43.298	+32:01:31.235	PerC25	Y	Y	I	1.8 ± 0.8	309.0 ± 64.0
Per-emb-56	03:47:05.450	+32:43:08.239	PerC27	⋯	⋯	I	0.5 ± 0.1	312.0 ± 1.0
Per-emb-57	03:29:03.331	+31:23:14.573	PerC10	Y	⋯	I	0.1 ± 0.5	313.0 ± 200.0
Per-emb-58	03:28:58.422	+31:22:17.480	PerC10	⋯	⋯	I	0.6 ± 0.5	322.0 ± 88.0
Per-emb-59	03:28:35.039	+30:20:09.884	PerC17	⋯	⋯	I	0.0 ± 0.1	341.0 ± 179.0
Per-emb-60	03:29:20.068	+31:24:07.488	PerC5	⋯	⋯	I	0.3 ± 1.1	363.0 ± 240.0
Per-emb-61	03:44:21.357	+31:59:32.514	PerC1	⋯	⋯	I	0.2 ± 0.2	371.0 ± 107.0
Per-emb-62	03:44:12.976	+32:01:35.412	PerC1	Y	Y	I	1.8 ± 0.4	378.0 ± 29.0
Per-emb-63	03:28:43.270	+31:17:32.930	PerC9	Y	Y	I	1.9 ± 0.4	436.0 ± 9.0

Table 1
(Continued)

Name[a]	R.A.[b] (J2000)	Decl.[b] (J2000)	Field[c]	Detected 6.4 cm	Detected 4.1 cm	Class	$L_{\rm bol}$[d] ($L_\odot$)	$T_{\rm bol}$[d] (K)
Per-emb-64	03:33:12.851	+31:21:24.020	PerC3	Y	Y	I	3.2 ± 0.6	438.0 ± 8.0
Per-emb-65	03:28:56.315	+31:22:27.797	PerC10	⋯	⋯	I	0.2 ± 0.2	440.0 ± 191.0
Per-emb-66	03:43:45.149	+32:03:58.607	PerC2	⋯	⋯	I	0.7 ± 0.2	542.0 ± 110.0
Per-bolo-58	03:29:25.463	+31:28:14.880	PerC7	⋯	⋯	0	0.1 ± 0.5	18.0 ± 18.0
Per-bolo-45	03:29:07.699	+31:17:16.800	PerC8	⋯	⋯	0	0.1 ± 0.1	18.0 ± 18.0
L1451-MMS	03:25:10.244	+30:23:55.058	PerC14	⋯	⋯	0	0.1 ± 0.1	18.0 ± 18.0
L1448IRS2E	03:25:25.660	+30:44:56.695	PerC13	⋯	⋯	0	0.1 ± 0.1	18.0 ± 18.0
B1-bN	03:33:21.209	+31:07:43.665	PerC38	⋯	⋯	0	0.3 ± 0.1	14.7 ± 1.0
B1-bS	03:33:21.355	+31:07:26.372	PerC38	⋯	⋯	0	0.7 ± 0.1	17.7 ± 1.0
L1448IRS1	03:25:09.448	+30:46:21.932	PerC36	Y	Y	I	⋯	⋯
L1448NW	03:25:35.670	+30:45:34.192	PerC29	Y	Y	0	1.4 ± 0.1	22.0 ± 1.0
L1448IRS3A	03:25:36.499	+30:45:21.880	PerC29	Y	Y	I	9.2 ± 1.3	47.0 ± 2.0
SVS13C	03:29:01.970	+31:15:38.053	PerC8	Y	Y	0	1.5 ± 0.2	21.0 ± 1.0
SVS13B	03:29:03.077	+31:15:51.739	PerC18	⋯	Y	0	1.0 ± 1.0	20.0 ± 20.0
IRAS03363+3207	03:39:25.546	+32:17:07.088	PerC33	Y	Y	I?	⋯	⋯
EDJ2009-263	03:30:27.161	+30:28:29.613	PerC15	⋯	⋯	Flat	0.2 ± 0.1	340.0 ± 18.0
EDJ2009-285	03:32:46.942	+30:59:17.797	PerC22	⋯	⋯	II	0.5 ± 0.1	920.0 ± 18.0
IRAS03295+3050	03:32:34.066	+31:00:55.620	PerC22	⋯	⋯	II	0.2 ± 0.1	1300.0 ± 18.0
L1455IRS2	03:27:47.689	+30:12:04.314	PerC20	Y	Y	Flat	2.5 ± 0.1	740.0 ± 18.0
EDJ2009-385	03:44:18.168	+32:04:56.907	PerC34	⋯	⋯	II	0.4 ± 0.1	1200.0 ± 18.0
EDJ2009-366	03:43:59.650	+32:01:54.007	PerC31	Y	Y	II	1.8 ± 0.1	620.0 ± 18.0
EDJ2009-269	03:30:44.013	+30:32:46.812	PerC32	⋯	Y	II	1.3 ± 0.1	1200.0 ± 18.0
EDJ2009-183	03:28:59.294	+31:15:48.407	PerC8	Y	Y	Flat	3.2 ± 0.1	100.0 ± 18.0
EDJ2009-164	03:28:53.961	+31:18:09.349	PerC9	⋯	⋯	II	0.1 ± 0.1	890.0 ± 18.0
EDJ2009-156	03:28:51.028	+31:18:18.409	PerC9	Y	Y	II	0.0 ± 0.1	740.0 ± 18.0
EDJ2009-172	03:28:56.649	+31:18:35.449	PerC18	Y	⋯	II	0.4 ± 0.1	1100.0 ± 18.0
IRAS4B’	03:29:12.841	+31:13:06.893	PerC35	⋯	⋯	0	0.1 ± 0.1	20.0 ± 20.0
EDJ2009-233	03:29:17.675	+31:22:44.922	PerC5	Y	Y	II	1.4 ± 0.1	1300.0 ± 18.0
EDJ2009-235	03:29:18.258	+31:23:19.758	PerC5	Y	⋯	II	0.5 ± 0.1	650.0 ± 18.0
SVS3	03:29:10.419	+31:21:59.072	PerC10	Y	Y	II	0.5 ± 0.1	⋯
SVS13A2	03:29:03.386	+31:16:01.622	PerC8	Y	Y	0?	0.1 ± 0.1	20.0 ± 18.0
EDJ2009-173	03:28:56.963	+31:16:22.199	PerC8	⋯	Y	II	0.1 ± 0.1	1100.0 ± 18.0

Notes.

[a] Names: Per-emb-XX (Enoch et al. 2009), EDJ2009-XXX (Evans et al. 2009), SVS-X (Strom et al. 1976).

[b] Coordinates from VANDAM Ka-band observations (Tobin et al. 2016).

[c] Name of the observational field where source was closest to the peak of the primary beam response.

[d] Values from Enoch et al. (2009), Sadavoy et al. (2014), and Young et al. (2015).

(This table is available in machine-readable form.)

Radio continuum emission from protostars is a unique tracer of the ionized component of the protostellar jet. Radio emission from protostars often appears as an unresolved and compact counterpart to the infrared and submillimeter detections. With high-resolution observations, extended radio emission is often elongated along the direction of the large-scale jets (e.g., Curiel et al. 1989; Anglada 1995), suggesting it is tracing the base of the collimated jet. The radio jets from protostars are most often found toward those in the intermediate- and high-mass regime (e.g., Rodríguez & Reipurth 1989; Curiel et al. 1993; Girart et al. 2002), but examples of low-mass protostars with radio jets are known as well (e.g., Rodríguez et al. 1997; Tychoniec et al. 2018).

Emission at centimeter wavelengths can track various processes in the protostellar environment. The radio spectral index (α; where $F_\nu \sim \nu^\alpha$) can be used to distinguish between different types of emission. Thermal dust emission usually has a steep spectrum with $\alpha = 2 + \beta$, where $\beta \lesssim 1$ for dense disks with large grains (Kwon et al. 2009; Testi et al. 2014). Dust emission is still detectable at ~1 cm, but is not expected to contribute significantly at the C-band. The free–free emission from ionized gas has a spectral index with typical values from -0.1 to 2.0 (Panagia & Felli 1975; Rodríguez et al. 2003). Spectral indices below -0.1 are indicative of non-thermal emission generally associated with synchrotron emission resulting from high-velocity electrons interacting with magnetic fields (e.g., Rybicki & Lightman 1979). This mechanism has been verified as a possibility because polarization in a protostellar radio jet with a negative spectral index has been detected (Carrasco-González et al. 2010). More evolved pre-main sequence stars can exhibit negative spectral indices due to the gyrosynchrotron emission from the stellar coronae (e.g., Dzib et al. 2013).

Understanding the contribution of different mechanisms of emission at radio wavelengths is essential not only to analyze ionized jets but also to analyze the dust emission at radio wavelengths. The free–free emission can significantly contribute to the continuum at shorter wavelengths, thereby increasing the measured flux densities. Any free–free contamination must be removed in order to obtain accurate measurements of dust properties and masses of the youngest protostellar disks.

Table 2
Summary of the Observed Fields

Name	Extragalactic (6.4 cm)	Protostars (6.4 cm)	YSOc (6.4 cm)	rms (6.4 cm) (mJy beam^{-1})	Beam Size and PA (6.4 cm)	Extragalactic (4 cm)	Protostars (4 cm)	YSOc (4 cm)	rms (4 cm) (mJy beam^{-1})	Beam Size and PA (4 cm)
PerC1	7	5	0	0.0053	$0\farcs36 \times 0\farcs52$ −76.40	9	3	1	0.0041	$0\farcs23 \times 0\farcs34$ −76.03
PerC2	11	4	0	0.0050	$0\farcs34 \times 0\farcs48$ 79.18	7	4	0	0.0040	$0\farcs22 \times 0\farcs31$ 78.94
PerC3	25	1	0	0.0050	$0\farcs35 \times 0\farcs38$ −82.95	11	1	0	0.0038	$0\farcs23 \times 0\farcs25$ 89.22
PerC4	12	2	0	0.0049	$0\farcs35 \times 0\farcs36$ −84.58	13	1	0	0.0042	$0\farcs23 \times 0\farcs24$ 87.64
PerC5	9	7	1	0.0051	$0\farcs35 \times 0\farcs39$ 62.69	8	5	1	0.0040	$0\farcs22 \times 0\farcs24$ 83.94
PerC6	11	1	0	0.0050	$0\farcs35 \times 0\farcs50$ −76.67	7	1	0	0.0040	$0\farcs22 \times 0\farcs32$ −76.80
PerC7	15	3	0	0.0049	$0\farcs35 \times 0\farcs37$ −83.60	9	1	0	0.0041	$0\farcs23 \times 0\farcs24$ −87.92
PerC8	19	20	0	0.0048	$0\farcs35 \times 0\farcs41$ 86.58	13	20	1	0.0039	$0\farcs22 \times 0\farcs26$ 87.31
PerC9	15	19	0	0.0051	$0\farcs34 \times 0\farcs38$ 88.11	10	15	0	0.0038	$0\farcs22 \times 0\farcs25$ 88.50
PerC10	15	11	2	0.0051	$0\farcs35 \times 0\farcs38$ 57.66	10	7	2	0.0040	$0\farcs23 \times 0\farcs24$ 81.70
PerC11	16	9	0	0.0050	$0\farcs36 \times 0\farcs39$ −64.98	12	3	0	0.0040	$0\farcs23 \times 0\farcs25$ −78.38
PerC12	14	0	0	0.0052	$0\farcs34 \times 0\farcs44$ 81.86	12	1	0	0.0045	$0\farcs23 \times 0\farcs28$ 74.00
PerC13	21	9	0	0.0052	$0\farcs36 \times 0\farcs42$ −83.87	14	8	0	0.0042	$0\farcs23 \times 0\farcs27$ −81.69
PerC14	17	0	0	0.0052	$0\farcs35 \times 0\farcs52$ −75.00	15	0	0	0.0040	$0\farcs22 \times 0\farcs33$ −74.99
PerC15	8	0	0	0.0055	$0\farcs35 \times 0\farcs56$ −74.66	2	0	0	0.0053	$0\farcs25 \times 0\farcs46$ −80.62
PerC16	22	1	0	0.0047	$0\farcs36 \times 0\farcs42$ −65.46	15	1	0	0.0037	$0\farcs23 \times 0\farcs26$ −81.34
PerC17	26	0	0	0.0050	$0\farcs36 \times 0\farcs41$ −63.46	17	0	0	0.0036	$0\farcs23 \times 0\farcs26$ −82.94
PerC18	6	13	1	0.0057	$0\farcs34 \times 0\farcs39$ 87.70	7	13	1	0.0042	$0\farcs22 \times 0\farcs26$ 88.68
PerC19	19	0	0	0.0053	$0\farcs34 \times 0\farcs46$ 80.66	14	1	0	0.0045	$0\farcs22 \times 0\farcs30$ 72.32
PerC20	28	4	0	0.0053	$0\farcs35 \times 0\farcs38$ 86.90	22	4	0	0.0041	$0\farcs22 \times 0\farcs24$ 88.98
PerC21	10	1	0	0.0048	$0\farcs35 \times 0\farcs49$ −76.18	10	1	0	0.0038	$0\farcs23 \times 0\farcs32$ −75.90
PerC22	12	0	0	0.0050	$0\farcs35 \times 0\farcs37$ −82.78	8	0	0	0.0038	$0\farcs23 \times 0\farcs24$ −88.25
PerC23	12	2	0	0.0050	$0\farcs34 \times 0\farcs39$ −86.53	10	2	0	0.0039	$0\farcs22 \times 0\farcs25$ −87.35
PerC24	10	1	0	0.0066	$0\farcs34 \times 0\farcs38$ −83.93	7	2	0	0.0040	$0\farcs22 \times 0\farcs25$ −84.83
PerC25	17	2	0	0.0049	$0\farcs34 \times 0\farcs36$ −78.68	12	2	0	0.0037	$0\farcs25 \times 0\farcs26$ 75.30
PerC26	16	1	0	0.0048	$0\farcs34 \times 0\farcs36$ −65.17	14	1	0	0.0037	$0\farcs22 \times 0\farcs23$ −63.02
PerC27	20	0	0	0.0048	$0\farcs34 \times 0\farcs36$ −75.53	18	0	0	0.0037	$0\farcs22 \times 0\farcs24$ −72.96
PerC28	14	0	0	0.0051	$0\farcs36 \times 0\farcs40$ −32.98	12	1	0	0.0041	$0\farcs23 \times 0\farcs25$ −74.85
PerC29	19	7	0	0.0053	$0\farcs36 \times 0\farcs45$ −86.34	12	7	0	0.0042	$0\farcs23 \times 0\farcs29$ −83.56
PerC31	13	5	0	0.0051	$0\farcs34 \times 0\farcs50$ 77.98	12	5	0	0.0040	$0\farcs22 \times 0\farcs32$ 78.46
PerC32	9	0	0	0.0054	$0\farcs35 \times 0\farcs53$ −75.83	7	2	0	0.0043	$0\farcs22 \times 0\farcs35$ −75.47
PerC33	14	1	0	0.0050	$0\farcs35 \times 0\farcs53$ −75.80	8	1	0	0.0040	$0\farcs22 \times 0\farcs34$ −75.40
PerC34	14	4	0	0.0053	$0\farcs35 \times 0\farcs50$ −76.70	12	2	0	0.0041	$0\farcs22 \times 0\farcs32$ −76.92
PerC35	18	19	0	0.0048	$0\farcs35 \times 0\farcs42$ 84.35	16	18	0	0.0039	$0\farcs23 \times 0\farcs27$ 85.51
PerC36	14	5	0	0.0068	$0\farcs38 \times 0\farcs59$ −67.14	7	3	0	0.0055	$0\farcs25 \times 0\farcs39$ −69.37
PerC37	6	13	0	0.0068	$0\farcs38 \times 0\farcs56$ −67.40	5	12	0	0.0055	$0\farcs25 \times 0\farcs37$ −69.58
PerC38	24	4	0	0.0049	$0\farcs34 \times 0\farcs37$ −84.82	18	5	0	0.0040	$0\farcs22 \times 0\farcs24$ 80.28
PerC39	29	0	0	0.0049	$0\farcs35 \times 0\farcs37$ −84.52	17	0	1	0.0040	$0\farcs22 \times 0\farcs24$ 82.26

To date, numerous studies have examined radio emission from protostars. Several authors have compiled existing observations and identified general trends between radio emission and protostellar properties (e.g., Anglada 1995; Furuya et al. 2003; Wu et al. 2004; Shirley et al. 2007), while others conducted surveys of molecular clouds. However, surveys thus far have lacked in sensitivity, resolution, and/or sample size (e.g., Reipurth et al. 2004; AMI Consortium et al. 2011; Dzib et al. 2013; Pech et al. 2016).

The VLA Nascent Disk and Multiplicity (VANDAM) Survey (Tobin et al. 2015a) is able to overcome previous limitations by targeting the largest homogeneous sample of protostars at 0.8, 1.0, 4.1, and 6.4 cm observing wavelengths. The VANDAM survey targeted all known Class 0 and Class I protostars in the Perseus molecular cloud, providing unbiased observations of the radio jets from those sources. Perseus is a natural choice for this survey, hosting not only the greatest number of young stellar objects among the nearby clouds but also the largest fraction of Class 0 and Class I protostars (Evans et al. 2009). The 235 pc distance to Perseus (Hirota et al. 2011) guarantees high spatial resolution observations.

In this paper, we present C-band observations (4.1 and 6.4 cm) from the NSF's Karl G. Jansky Very Large Array of all known protostars in the Perseus molecular cloud, including flux densities and derived spectral indices. We also calculate masses of compact dust emission at 9 mm from Ka-band observations, taking into account the free–free contributions based on the C-band data. Furthermore, we compare those parameters with protostellar properties such as bolometric luminosity and temperature, molecular and atomic far-infrared line luminosities, and outflow force.

1.1. The Sample

A total of 95 protostars were targeted by the VANDAM survey in C-band, summarized in Table 1. The sample was selected using *Spitzer*, *Herschel*, and Bolocam observations (Enoch et al. 2009; Evans et al. 2009; Sadavoy et al. 2014). The sources have bolometric luminosities between 0.1 $L_\odot$ and 33 $L_\odot$, spanning the low-mass regime. For a detailed description of the source sample selection, see Tobin et al. (2016). The non-detection of three Class II sources in Ka-band: EDJ2009-161, EDJ2009-333, and EDJ2009-268 resulted in them being excluded from the C-band observations. On the other hand, serendipitous Ka-band detections of the Class II sources EDJ2009-233, EDJ2009-173, and EDJ2009-235, as well as the pre-main sequence binary system SVS3, are included in the C-band sample.

2. Observations and Analysis

We conducted C-band observations with the VLA in A-configuration between 2014 February 28 and 2014 April 12. The C-band data (4.1 and 6.4 cm) were taken in 8 bit mode, yielding 2 GHz of bandwidth divided into sixteen 128 MHz sub-bands with 2 MHz channels and full polarization products.

We centered our 1 GHz basebands at 4.7 and 7.4 GHz, thus avoiding some persistent radio frequency interference in these bands. Taking observations in two different frequencies enables measurement of the spectral index, which is crucial in the characterization of the sources and for discriminating between protostars and extragalactic sources. Radio source 3C48 was both the absolute flux density and bandpass calibrator, and J0336+3218 was the complex gain calibrator. The estimated absolute flux calibration uncertainty is ∼5%; it is not included in the reported flux density errors. This error will not influence the spectral index, as it is obtained from observations at two ends of the same band, and thus limited only by the uncertainty (~2%) of the flux calibrator model (Perley & Butler 2017). Further details of the calibration and data reduction of the C-band observations are described in the previous VANDAM papers (Tobin et al. 2015a; Tychoniec et al. 2018)

The large primary beam of the C-band observations—5′ and 7$'\!.$2 FWHM for 4.1 and 6.4 cm, respectively—means that fewer pointings are necessary, as compared to Ka-band observations; 38 fields were observed in total. Due to the overlap of the fields, some sources have multiple detections. In those cases, the detection with the lowest distance to the primary beam center was used in the analysis. The typical size of the synthesized beam was 0$''\!.$3–0$''\!.$4, with a typical rms noise of 4–6 μJy. Separate characteristics of each field are provided in Table 2. We used the AEGEAN source finder version r903 (Hancock et al. 2012) to identify sources in all the fields with a specific *seed* threshold, defining the lowest peak value for the source to be claimed real, set to 6σ. With the CASA (version 4.2.2; McMullin et al. 2007) *imstat* procedure, we obtained rms over the whole image and used it as an input in the source finder code. Fields C15, C16, and C21, have prominent radio galaxies that created artifacts in the maps. For these fields, we measured the noise value manually in an area unaffected by the bright sources. Frames were also cross-checked manually for the protostars not detected by the source finder code and detections over 3σ at protostellar positions were added to the sample.

Based on the method described above, a list of objects was created and we performed 2D Gaussian fitting with the CASA task *imfit* to measure flux densities and corresponding errors. Unresolved sources with relatively faint emission (below 15σ) were fit using Gaussians with position angle and sizes that matched the synthesized beam to avoid unrealistic fit parameters. For sources with extended emission, the source finder code provided multiple peaks of emission that were subsequently used in the *imfit* task as the Gaussian peaks. For these sources, the resulting flux density is the sum of all components. Finally, we corrected fluxes for the primary beam attenuation.

In this work, we explore correlations between measured flux densities and protostellar properties. Due to a large number of non-detections of known protostars, properly accounting for upper limits enables us to derive more accurate correlations from the data. For correlations, we use the Space Telescope Data Analysis System (STSDAS) *statistics* package, which allows one to analyze data sets with upper and/or lower limits. To estimate the correlation strengths, we use Spearman's rank correlation coefficient (ρ), obtained with the STSDAS *spearman* procedure, which also provides the probability of no correlation (P). The Expectation-Maximization algorithm (EM) is used to obtain parameters of the best linear fit to the data with the procedure *emmethod*. For equations and implementation of the data censoring, see Isobe et al. (1986). To determine whether two sets of values are statistically different, we use a log-rank test and a Kaplan–Meier (KM) estimator to produce cumulative distribution functions. Both procedures are implemented within the LIFELINES package for Python (Davidson-Pilon 2017), which takes upper limits into account.

Table 3
C-band Observation Results

Name	R.A. (J2000)	Decl. (J2000)	$F_{\nu,\mathrm{int}}$[a] (6.4 cm) (mJy)	$F_{\nu,\mathrm{peak}}$[b] (6.4 cm) (mJy beam^{-1})	rms (6.4 cm) (mJy beam^{-1})	$F_{\nu,\mathrm{int}}$[a] (4.1 cm) (mJy)	$F_{\nu,\mathrm{peak}}$[b] (4.1 cm) (mJy beam^{-1})	rms (4.1 cm) (mJy beam^{-1})	Sp. Index Int.[c]	Sp. Index Peak[d]
Per-emb-1	03:43:56.805	+32:00:50.201	0.0508 ± 0.0065	0.0476	0.0052	0.0651 ± 0.0059	0.0539	0.0043	0.55 ± 0.34	0.27 ± 0.30
Per-emb-2	03:32:17.927	+30:49:47.825	0.0365 ± 0.0065	0.0278	0.0050	0.0508 ± 0.0056	0.0426	0.0039	0.73 ± 0.46	0.94 ± 0.44
Per-emb-2-A	03:32:17.931	+30:49:47.705	0.0365 ± 0.0065	0.0278	0.0050	0.0508 ± 0.0056	0.0426	0.0039	0.73 ± 0.46	0.94 ± 0.44
Per-emb-2-B	03:32:17.926	+30:49:47.750	−77.0 ± −77.0	−77.0	−77.0	−77.0 ± −77.0	−77.0	−77.0	…	…
Per-emb-3	03:29:00.574	+31:12:00.204	0.1012 ± 0.0215	0.0784	0.0068	0.0763 ± 0.0073	0.0673	0.0055	−0.62 ± 0.51	−0.33 ± 0.26
Per-emb-4	03:28:39.101	+31:06:01.800	<0.0160 ± 0.0053	<0.0160	0.0053	<0.0140 ± 0.0047	<0.0140	0.0047	…	…
Per-emb-5	03:31:20.938	+30:45:30.273	<0.0197 ± 0.0000	<0.0000	0.0000	0.0283 ± 0.0184	0.0252	0.0040	>0.80 ± 1.44	>−99.00 ± −99.00
Per-emb-5-A	03:31:20.943	+30:45:30.271	<0.0197 ± 0.0066	<0.0000	0.0066	0.0283 ± 0.0184	0.0252	0.0040	>0.80 ± 1.61	>−99.00 ± −99.00
Per-emb-5-B	03:31:20.935	+30:45:30.246	−77.0 ± −77.0	−77.0	−77.0	−77.0 ± −77.0	−77.0	−77.0	…	…
Per-emb-6	03:33:14.404	+31:07:10.714	0.0664 ± 0.0057	0.0669	0.0050	0.0706 ± 0.0051	0.0691	0.0042	0.14 ± 0.25	0.07 ± 0.21
Per-emb-7	03:30:32.681	+30:26:26.480	<0.0174 ± 0.0058	<0.0174	0.0058	<0.0183 ± 0.0061	<0.0183	0.0061	…	…
Per-emb-8	03:44:43.981	+32:01:35.210	0.2788 ± 0.0122	0.1323	0.0049	0.3132 ± 0.0166	0.1240	0.0037	0.26 ± 0.15	−0.14 ± 0.10
Per-emb-9	03:29:51.831	+31:39:05.904	0.0420 ± 0.0094	0.0324	0.0050	0.0277 ± 0.0050	0.0281	0.0040	−0.92 ± 0.63	−0.31 ± 0.46
Per-emb-10	03:33:16.424	+31:06:52.063	<0.0148 ± 0.0049	<0.0148	0.0049	0.0334 ± 0.0054	0.0312	0.0041	>1.80 ± 0.81	>1.65 ± 0.79
Per-emb-11	03:43:57.064	+32:03:04.788	0.0366 ± 0.0058	0.0376	0.0052	0.0469 ± 0.0061	0.0425	0.0046	0.55 ± 0.45	0.27 ± 0.39
Per-emb-11-A	03:43:57.064	+32:03:04.787	<0.0158 ± 0.0053	<0.0158	0.0053	<0.0137 ± 0.0046	<0.0137	0.0046	…	…
Per-emb-11-B	03:43:56.881	+32:03:02.977	0.0366 ± 0.0058	0.0376	0.0052	0.0469 ± 0.0061	0.0425	0.0046	0.55 ± 0.45	0.27 ± 0.39
Per-emb-11-C	03:43:57.687	+32:03:09.975	<0.0159 ± 0.0053	<0.0159	0.0053	<0.0140 ± 0.0047	<0.0140	0.0047	…	…
Per-emb-12	03:29:10.536	+31:13:30.933	0.1557 ± 0.0144	0.1026	0.0049	0.2550 ± 0.0139	0.1297	0.0039	1.09 ± 0.24	0.52 ± 0.12
Per-emb-12-A	03:29:10.536	+31:13:30.926	0.0539 ± 0.0085	0.0466	0.0049	0.1166 ± 0.0081	0.0917	0.0039	1.70 ± 0.38	1.49 ± 0.25
Per-emb-12-B	03:29:10.427	+31:13:32.098	0.1017 ± 0.0059	0.1026	0.0049	0.1384 ± 0.0057	0.1297	0.0039	0.68 ± 0.16	0.52 ± 0.12
Per-emb-13	03:29:12.015	+31:13:08.031	0.0618 ± 0.0058	0.0590	0.0049	0.0776 ± 0.0070	0.0549	0.0039	0.50 ± 0.29	−0.16 ± 0.24
Per-emb-14	03:29:13.547	+31:13:58.150	0.0193 ± 0.0031	0.0261	0.0049	0.0591 ± 0.0093	0.0357	0.0040	2.47 ± 0.50	0.69 ± 0.48
Per-emb-15	03:29:04.054	+31:14:46.236	0.0547 ± 0.0077	0.0386	0.0050	0.0528 ± 0.0154	0.0217	0.0041	−0.08 ± 0.71	−1.27 ± 0.51
Per-emb-16	03:43:50.978	+32:03:24.101	<0.0149 ± 0.0050	<0.0149	0.0050	<0.0119 ± 0.0040	<0.0119	0.0040	…	…
Per-emb-17	03:27:39.104	+30:13:03.067	0.0471 ± 0.0056	0.0495	0.0054	0.0596 ± 0.0089	0.0582	0.0042	0.52 ± 0.42	0.36 ± 0.29
Per-emb-17-A	03:27:39.104	+30:13:03.078	0.0471 ± 0.0056	0.0495	0.0054	0.0596 ± 0.0089	0.0582	0.0042	0.52 ± 0.42	0.36 ± 0.29
Per-emb-17-B	03:27:39.115	+30:13:02.839	<0.0161 ± 0.0053	<0.0161	0.0053	<0.0125 ± 0.0042	<0.0125	0.0042	…	…
Per-emb-18	03:29:11.258	+31:18:31.072	0.1919 ± 0.0090	0.1326	0.0058	0.1957 ± 0.0059	0.1505	0.0043	0.04 ± 0.12	0.28 ± 0.11
Per-emb-18-A	03:29:11.254	+31:18:31.061	0.1919 ± 0.0090	0.1326	0.0058	0.1957 ± 0.0059	0.1505	0.0043	0.04 ± 0.12	0.28 ± 0.11
Per-emb-18-B	03:29:11.261	+31:18:31.072	−77.0 ± −77.0	−77.0	−77.0	−77.0 ± −77.0	−77.0	−77.0	…	…
Per-emb-19	03:29:23.497	+31:33:29.172	0.0560 ± 0.0087	0.0429	0.0049	0.0371 ± 0.0059	0.0321	0.0042	−0.91 ± 0.49	−0.64 ± 0.38
Per-emb-20	03:27:43.276	+30:12:28.780	0.1477 ± 0.0083	0.1093	0.0054	0.1384 ± 0.0124	0.1098	0.0042	−0.14 ± 0.23	0.01 ± 0.14
Per-emb-21	03:29:10.668	+31:18:20.191	<0.0173 ± 0.0057	<0.0173	0.0057	<0.0127 ± 0.0042	<0.0127	0.0042	…	…
Per-emb-22	03:25:22.409	+30:45:13.257	0.1426 ± 0.0147	0.0978	0.0052	0.1806 ± 0.0149	0.0957	0.0042	0.52 ± 0.29	−0.05 ± 0.15
Per-emb-22-A	03:25:22.409	+30:45:13.253	0.1067 ± 0.0069	0.0978	0.0052	0.1348 ± 0.0072	0.0957	0.0042	0.51 ± 0.18	−0.05 ± 0.15
Per-emb-22-B	03:25:22.352	+30:45:13.151	0.0359 ± 0.0079	0.0360	0.0052	0.0459 ± 0.0077	0.0384	0.0042	0.54 ± 0.61	0.14 ± 0.40
Per-emb-23	03:29:17.211	+31:27:46.302	0.0363 ± 0.0060	0.0356	0.0050	0.0483 ± 0.0057	0.0432	0.0043	0.63 ± 0.45	0.43 ± 0.38
Per-emb-24	03:28:45.297	+31:05:41.693	<0.0159 ± 0.0053	<0.0159	0.0053	0.0222 ± 0.0037	0.0266	0.0046	>0.74 ± 0.82	>1.13 ± 0.83
Per-emb-25	03:26:37.510	+30:15:27.812	0.0510 ± 0.0091	0.0326	0.0048	0.0641 ± 0.0059	0.0507	0.0038	0.50 ± 0.44	0.97 ± 0.36
Per-emb-26	03:25:38.874	+30:44:05.283	0.0581 ± 0.0068	0.0557	0.0054	0.0911 ± 0.0049	0.0937	0.0045	0.99 ± 0.28	1.15 ± 0.24
Per-emb-27	03:28:55.569	+31:14:37.025	0.0589 ± 0.0067	0.0527	0.0051	0.1085 ± 0.0110	0.0744	0.0044	1.34 ± 0.34	0.76 ± 0.25
Per-emb-27-A	03:28:55.569	+31:14:37.022	0.0589 ± 0.0067	0.0527	0.0051	0.0846 ± 0.0056	0.0744	0.0044	0.80 ± 0.29	0.76 ± 0.25
Per-emb-27-B	03:28:55.563	+31:14:36.407	<0.0153 ± 0.0051	<0.0153	0.0051	0.0239 ± 0.0054	0.0271	0.0044	>0.98 ± 0.89	>1.26 ± 0.82
Per-emb-28	03:43:51.007	+32:03:08.042	0.0207 ± 0.0053	0.0208	0.0050	0.0272 ± 0.0053	0.0228	0.0040	0.60 ± 0.71	0.20 ± 0.65
Per-emb-29	03:33:17.877	+31:09:31.816	<0.0166 ± 0.0055	<0.0166	0.0055	<0.0165 ± 0.0055	<0.0165	0.0055	…	…

Table 3
(Continued)

Name	R.A. (J2000)	Decl. (J2000)	$F_{\nu,\rm int}$ [a] (6.4 cm) (mJy)	$F_{\nu,\rm peak}$ [b] (6.4 cm) (mJy beam^{-1})	rms (6.4 cm) (mJy beam^{-1})	$F_{\nu,\rm int}$ [a] (4.1 cm) (mJy)	$F_{\nu,\rm peak}$ [b] (4.1 cm) (mJy beam^{-1})	rms (4.1 cm) (mJy beam^{-1})	Sp. Index Int.[c]	Sp. Index Peak[d]
Per-emb-30	03:33:27.303	+31:07:10.159	0.2747 ± 0.0171	0.1542	0.0055	0.2815 ± 0.0254	0.1681	0.0055	0.05 ± 0.24	0.19 ± 0.11
Per-emb-31	03:28:32.547	+31:11:05.151	<0.0162 ± 0.0054	<0.0162	0.0054	<0.0151 ± 0.0050	<0.0151	0.0050	…	…
Per-emb-32	03:44:02.403	+32:02:04.734	<0.0155 ± 0.0052	<0.0155	0.0052	<0.0126 ± 0.0042	<0.0126	0.0042	…	…
Per-emb-32-A	03:44:02.403	+32:02:04.729	<0.0155 ± 0.0052	<0.0155	0.0052	<0.0126 ± 0.0042	<0.0126	0.0042	…	…
Per-emb-32-B	03:44:02.632	+32:01:59.451	<0.0155 ± 0.0052	<0.0155	0.0052	<0.0126 ± 0.0042	<0.0126	0.0042	…	…
Per-emb-33	03:25:36.379	+30:45:14.727	0.1648 ± 0.0139	0.1154	0.0053	0.1386 ± 0.0071	0.1041	0.0042	−0.38 ± 0.22	−0.23 ± 0.13
Per-emb-33-A	03:25:36.380	+30:45:14.722	0.0259 ± 0.0057	0.0282	0.0053	<0.0127 ± 0.0042	<0.0127	0.0042	<−1.57 ± 0.88	<−1.75 ± 0.84
Per-emb-33-B	03:25:36.380	+30:45:14.722	<0.0618 ± 0.0206	<0.0618	0.0206	<1.6581 ± 0.5527	<1.6581	0.5527	…	…
Per-emb-33-C	03:25:36.321	+30:45:14.913	0.1389 ± 0.0082	0.1154	0.0053	0.1386 ± 0.0071	0.1041	0.0042	−0.00 ± 0.17	−0.23 ± 0.13
Per-emb-34	03:30:15.162	+30:23:49.232	<0.0153 ± 0.0051	<0.0153	0.0051	0.0269 ± 0.0087	0.0178	0.0041	>1.25 ± 1.02	>0.34 ± 0.89
Per-emb-35	03:28:37.090	+31:13:30.787	0.0710 ± 0.0084	0.0626	0.0051	0.1109 ± 0.0110	0.0750	0.0043	0.98 ± 0.34	0.40 ± 0.22
Per-emb-35-A	03:28:37.090	+31:13:30.787	0.0576 ± 0.0056	0.0626	0.0051	0.0815 ± 0.0054	0.0750	0.0043	0.76 ± 0.26	0.40 ± 0.22
Per-emb-35-B	03:28:37.219	+31:13:31.751	0.0134 ± 0.0028	0.0240	0.0051	0.0294 ± 0.0056	0.0271	0.0043	1.73 ± 0.62	0.27 ± 0.58
Per-emb-36	03:28:57.373	+31:14:15.772	0.2433 ± 0.0192	0.1267	0.0051	0.2523 ± 0.0169	0.1037	0.0044	0.08 ± 0.23	−0.44 ± 0.13
Per-emb-36-A	03:28:57.373	+31:14:15.764	0.2433 ± 0.0192	0.1267	0.0051	0.2523 ± 0.0169	0.1037	0.0044	0.08 ± 0.23	−0.44 ± 0.13
Per-emb-36-B	03:28:57.370	+31:14:16.072	<0.0152 ± 0.0051	<0.0152	0.0051	<0.0132 ± 0.0044	<0.0132	0.0044	…	…
Per-emb-37	03:29:18.964	+31:23:14.304	<0.0153 ± 0.0051	<0.0153	0.0051	<0.0122 ± 0.0041	<0.0122	0.0041	…	…
Per-emb-38	03:32:29.197	+31:02:40.759	<0.0150 ± 0.0050	<0.0150	0.0050	<0.0115 ± 0.0038	<0.0115	0.0038	…	…
Per-emb-39	03:33:13.781	+31:20:05.204	<0.0155 ± 0.0052	<0.0155	0.0052	<0.0129 ± 0.0043	<0.0129	0.0043	…	…
Per-emb-40	03:33:16.669	+31:07:54.901	0.1129 ± 0.0102	0.0956	0.0049	0.1232 ± 0.0081	0.1014	0.0041	0.19 ± 0.25	0.13 ± 0.14
Per-emb-40-A	03:33:16.669	+31:07:54.902	0.0940 ± 0.0055	0.0956	0.0049	0.1106 ± 0.0051	0.1014	0.0041	0.36 ± 0.17	0.13 ± 0.14
Per-emb-40-B	03:33:16.679	+31:07:55.269	0.0189 ± 0.0047	0.0265	0.0049	0.0125 ± 0.0030	0.0175	0.0041	−0.91 ± 0.76	−0.91 ± 0.66
Per-emb-41	03:33:20.341	+31:07:21.354	<0.0148 ± 0.0049	<0.0148	0.0049	<0.0123 ± 0.0041	<0.0123	0.0041	…	…
Per-emb-42	03:25:39.135	+30:43:57.908	<0.0164 ± 0.0054	<0.0164	0.0054	<0.0138 ± 0.0046	<0.0138	0.0046	…	…
Per-emb-43	03:42:02.160	+31:48:02.080	<0.0149 ± 0.0050	<0.0149	0.0050	<0.0125 ± 0.0042	<0.0125	0.0042	…	…
Per-emb-44	03:29:03.763	+31:16:03.808	0.1236 ± 0.0132	0.0736	0.0050	0.2015 ± 0.0108	0.0958	0.0042	1.08 ± 0.26	0.58 ± 0.18
Per-emb-44-A	03:29:03.766	+31:16:03.810	0.0590 ± 0.0057	0.0736	0.0050	0.0929 ± 0.0048	0.0958	0.0042	1.00 ± 0.24	0.58 ± 0.18
Per-emb-44-B	03:29:03.742	+31:16:03.789	0.0645 ± 0.0075	0.0709	0.0050	0.1086 ± 0.0060	0.0850	0.0042	1.15 ± 0.28	0.40 ± 0.19
Per-emb-45	03:33:09.569	+31:05:31.192	<0.0178 ± 0.0059	<0.0178	0.0059	<0.0200 ± 0.0067	<0.0200	0.0067	…	…
Per-emb-46	03:28:00.414	+30:08:01.013	<0.0142 ± 0.0047	<0.0142	0.0047	0.0152 ± 0.0031	0.0205	0.0037	>0.15 ± 0.86	>0.81 ± 0.84
Per-emb-47	03:28:34.507	+31:00:50.990	<0.0158 ± 0.0053	<0.0158	0.0053	0.0393 ± 0.0100	0.0242	0.0045	>2.01 ± 0.93	>0.94 ± 0.84
Per-emb-48	03:27:38.268	+30:13:58.448	0.0721 ± 0.0076	0.0572	0.0055	0.0616 ± 0.0051	0.0632	0.0045	−0.35 ± 0.30	0.22 ± 0.26
Per-emb-48-A	03:27:38.277	+30:13:58.558	<0.0166 ± 0.0055	<0.0166	0.0055	<0.0135 ± 0.0045	<0.0135	0.0045	…	…
Per-emb-48-B	03:27:38.258	+30:13:58.319	0.0721 ± 0.0076	0.0572	0.0055	0.0616 ± 0.0051	0.0632	0.0045	−0.35 ± 0.30	0.22 ± 0.26
Per-emb-49	03:29:12.956	+31:18:14.306	0.0477 ± 0.0102	0.0284	0.0058	0.0590 ± 0.0096	0.0333	0.0043	0.47 ± 0.59	0.36 ± 0.54
Per-emb-49-A	03:29:12.952	+31:18:14.289	0.0119 ± 0.0027	0.0232	0.0058	0.0337 ± 0.0047	0.0333	0.0043	2.29 ± 0.59	0.80 ± 0.62
Per-emb-49-B	03:29:12.975	+31:18:14.396	0.0358 ± 0.0075	0.0284	0.0058	0.0253 ± 0.0050	0.0256	0.0043	−0.76 ± 0.63	−0.23 ± 0.59
Per-emb-50	03:29:07.768	+31:21:57.128	0.1096 ± 0.0080	0.0899	0.0053	0.1355 ± 0.0061	0.1199	0.0045	0.47 ± 0.19	0.63 ± 0.15
Per-emb-51	03:28:34.536	+31:07:05.520	<0.0177 ± 0.0059	<0.0177	0.0059	<0.0182 ± 0.0061	<0.0182	0.0061	…	…
Per-emb-52	03:28:39.699	+31:17:31.882	<0.0160 ± 0.0053	<0.0160	0.0053	<0.0129 ± 0.0043	<0.0129	0.0043	…	…
Per-emb-53	03:47:41.591	+32:51:43.672	0.0192 ± 0.0043	0.0265	0.0048	0.0284 ± 0.0044	0.0307	0.0037	0.86 ± 0.60	0.33 ± 0.48
Per-emb-54	03:29:01.548	+31:20:20.497	0.0387 ± 0.0080	0.0313	0.0055	0.0730 ± 0.0063	0.0658	0.0049	1.40 ± 0.49	1.64 ± 0.42
Per-emb-55	03:44:43.298	+32:01:31.235	0.0423 ± 0.0064	0.0386	0.0049	0.0559 ± 0.0052	0.0470	0.0037	0.61 ± 0.39	0.44 ± 0.33
Per-emb-55-A	03:44:43.297	+32:01:31.223	<0.0147 ± 0.0049	<0.0147	0.0049	<0.0111 ± 0.0037	<0.0111	0.0037	…	…
Per-emb-55-B	03:44:43.333	+32:01:31.636	0.0423 ± 0.0064	0.0386	0.0049	0.0559 ± 0.0052	0.0470	0.0037	0.61 ± 0.39	0.44 ± 0.33
Per-emb-56	03:47:05.450	+32:43:08.239	<0.0144 ± 0.0048	<0.0144	0.0048	<0.0112 ± 0.0037	<0.0112	0.0037	…	…

Table 3
(Continued)

Name	R.A. (J2000)	Decl. (J2000)	$F_{\nu,\rm int}$[a] (6.4 cm) (mJy)	$F_{\nu,\rm peak}$[b] (6.4 cm) (mJy beam^{-1})	rms (6.4 cm) (mJy beam^{-1})	$F_{\nu,\rm int}$[a] (4.1 cm) (mJy)	$F_{\nu,\rm peak}$[b] (4.1 cm) (mJy beam^{-1})	rms (4.1 cm) (mJy beam^{-1})	Sp. Index Int.[c]	Sp. Index Peak[d]
Per-emb-57	03:29:03.331	+31:23:14.573	0.0179 ± 0.0044	0.0233	0.0053	<0.0133 ± 0.0044	<0.0133	0.0044	<−0.66 ± 0.91	<−1.24 ± 0.89
Per-emb-58	03:28:58.422	+31:22:17.480	<0.0154 ± 0.0051	<0.0154	0.0051	<0.0123 ± 0.0041	<0.0123	0.0041	⋯	⋯
Per-emb-59	03:28:35.039	+30:20:09.884	<0.0151 ± 0.0050	<0.0151	0.0050	<0.0108 ± 0.0036	<0.0108	0.0036	⋯	⋯
Per-emb-60	03:29:20.068	+31:24:07.488	<0.0153 ± 0.0051	<0.0153	0.0051	<0.0122 ± 0.0040	<0.0122	0.0040	⋯	⋯
Per-emb-61	03:44:21.357	+31:59:32.514	<0.0164 ± 0.0055	<0.0164	0.0055	<0.0135 ± 0.0045	<0.0135	0.0045	⋯	⋯
Per-emb-62	03:44:12.976	+32:01:35.419	0.0529 ± 0.0070	0.0503	0.0056	0.0725 ± 0.0067	0.0598	0.0049	0.70 ± 0.36	0.38 ± 0.30
Per-emb-63	03:28:43.270	+31:17:32.930	0.0985 ± 0.0070	0.0844	0.0052	0.0988 ± 0.0047	0.0940	0.0039	0.01 ± 0.19	0.24 ± 0.16
Per-emb-64	03:33:12.851	+31:21:24.020	0.3704 ± 0.0073	0.3086	0.0050	0.3856 ± 0.0061	0.3076	0.0038	0.09 ± 0.06	−0.01 ± 0.04
Per-emb-65	03:28:56.315	+31:22:27.797	<0.0158 ± 0.0053	<0.0158	0.0053	<0.0132 ± 0.0044	<0.0132	0.0044	⋯	⋯
Per-emb-66	03:43:45.149	+32:03:58.607	<0.0155 ± 0.0052	<0.0155	0.0052	<0.0133 ± 0.0044	<0.0133	0.0044	⋯	⋯
Per-bolo-58	03:29:25.463	+31:28:14.880	<0.0151 ± 0.0050	<0.0151	0.0050	<0.0135 ± 0.0045	<0.0135	0.0045	⋯	⋯
Per-bolo-45	03:29:07.699	+31:17:16.800	<0.0173 ± 0.0057	<0.0173	0.0057	<0.0182 ± 0.0061	<0.0182	0.0061	⋯	⋯
L1451-MMS	03:25:10.244	+30:23:55.058	<0.0155 ± 0.0052	<0.0155	0.0052	<0.0121 ± 0.0040	<0.0121	0.0040	⋯	⋯
L1448IRS2E	03:25:25.660	+30:44:56.695	<0.0157 ± 0.0052	<0.0157	0.0052	<0.0128 ± 0.0043	<0.0128	0.0043	⋯	⋯
B1-bN	03:33:21.209	+31:07:43.665	<0.0149 ± 0.0050	<0.0149	0.0050	<0.0126 ± 0.0042	<0.0126	0.0042	⋯	⋯
B1-bS	03:33:21.355	+31:07:26.372	<0.0149 ± 0.0050	<0.0149	0.0050	<0.0126 ± 0.0042	<0.0126	0.0042	⋯	⋯
L1448IRS1	03:25:09.448	+30:46:21.932	0.0577 ± 0.0078	0.0593	0.0068	0.0742 ± 0.0063	0.0729	0.0055	0.55 ± 0.35	0.45 ± 0.30
L1448IRS1-A	03:25:09.448	+30:46:21.932	0.0577 ± 0.0078	0.0593	0.0068	0.0742 ± 0.0063	0.0729	0.0055	0.55 ± 0.35	0.45 ± 0.30
L1448IRS1-B	03:25:09.409	+30:46:20.603	<0.0205 ± 0.0068	<0.0205	0.0068	<0.0166 ± 0.0055	<0.0166	0.0055	⋯	⋯
L1448NW	03:25:35.670	+30:45:34.192	0.0247 ± 0.0038	0.0288	0.0053	0.0549 ± 0.0106	0.0307	0.0043	1.76 ± 0.54	0.14 ± 0.51
L1448NW-A	03:25:35.669	+30:45:34.109	0.0247 ± 0.0038	0.0288	0.0053	0.0401 ± 0.0060	0.0307	0.0043	1.06 ± 0.48	0.14 ± 0.51
L1448NW-B	03:25:35.672	+30:45:34.356	<0.0160 ± 0.0053	<0.0160	0.0053	0.0149 ± 0.0046	0.0268	0.0043	>−0.16 ± 1.00	>1.14 ± 0.82
L1448IRS3A	03:25:36.499	+30:45:21.880	0.4922 ± 0.0149	0.3717	0.0053	0.5074 ± 0.0149	0.3607	0.0043	0.07 ± 0.09	−0.07 ± 0.04
SVS13C	03:29:01.970	+31:15:38.053	1.0676 ± 0.0218	0.6812	0.0049	1.2095 ± 0.0296	0.6753	0.0039	0.28 ± 0.07	−0.02 ± 0.02
SVS13B	03:29:03.077	+31:15:51.739	<0.0224 ± 0.0075	<0.0224	0.0075	0.0541 ± 0.0101	0.0385	0.0084	>1.94 ± 0.84	>1.19 ± 0.88
IRAS03363+3207	03:39:25.546	+32:17:07.088	0.0222 ± 0.0048	0.0230	0.0050	0.0492 ± 0.0049	0.0467	0.0040	1.75 ± 0.52	1.56 ± 0.52
EDJ2009-263	03:30:27.161	+30:28:29.613	<0.0168 ± 0.0056	<0.0168	0.0056	<0.0168 ± 0.0056	<0.0168	0.0056	⋯	⋯
EDJ2009-285	03:32:46.942	+30:59:17.797	<0.0331 ± 0.0110	<0.0331	0.0110	<0.1088 ± 0.0362	<0.1088	0.0362	⋯	⋯
IRAS03295+3050	03:32:34.066	+31:00:55.620	<0.0169 ± 0.0056	<0.0169	0.0056	<0.0155 ± 0.0052	<0.0155	0.0052	⋯	⋯
L1455IRS2	03:27:47.689	+30:12:04.314	0.0342 ± 0.0086	0.0188	0.0057	0.0308 ± 0.0063	0.0288	0.0049	−0.23 ± 0.71	0.94 ± 0.77
EDJ2009-385	03:44:18.168	+32:04:56.907	<0.0158 ± 0.0053	<0.0158	0.0053	<0.0123 ± 0.0041	<0.0123	0.0041	⋯	⋯
EDJ2009-366	03:43:59.650	+32:01:54.007	0.0331 ± 0.0068	0.0273	0.0051	0.0521 ± 0.0124	0.0262	0.0040	1.00 ± 0.69	−0.09 ± 0.53
EDJ2009-269	03:30:44.013	+30:32:46.812	<0.0163 ± 0.0054	<0.0163	0.0054	0.0556 ± 0.0153	0.0199	0.0043	>2.70 ± 0.95	>0.44 ± 0.88
EDJ2009-269-A	03:30:44.014	+30:32:46.813	<0.0163 ± 0.0054	<0.0000	0.0054	0.0358 ± 0.0102	0.0199	0.0043	>1.73 ± 0.97	>−99.00 ± −99.00
EDJ2009-269-B	03:30:43.975	+30:32:46.583	<0.0163 ± 0.0054	<0.0163	0.0054	0.0198 ± 0.0051	0.0199	0.0043	>0.42 ± 0.93	>0.44 ± 0.88
EDJ2009-183	03:28:59.294	+31:15:48.407	0.0488 ± 0.0069	0.0424	0.0049	0.0499 ± 0.0048	0.0498	0.0040	0.05 ± 0.38	0.36 ± 0.31
EDJ2009-183-A	03:28:59.294	+31:15:48.406	0.0488 ± 0.0069	0.0424	0.0049	0.0499 ± 0.0048	0.0498	0.0040	0.05 ± 0.38	0.36 ± 0.31
EDJ2009-183-B	03:28:59.374	+31:15:48.401	<0.0146 ± 0.0049	<0.0146	0.0049	<0.0120 ± 0.0040	<0.0120	0.0040	⋯	⋯
EDJ2009-164	03:28:53.961	+31:18:09.349	<0.0174 ± 0.0058	<0.0174	0.0058	<0.0158 ± 0.0053	<0.0158	0.0053	⋯	⋯
EDJ2009-156	03:28:51.028	+31:18:18.409	0.0175 ± 0.0054	0.0200	0.0055	0.0295 ± 0.0042	0.0362	0.0046	1.15 ± 0.75	1.31 ± 0.67
EDJ2009-156-A	03:28:51.028	+31:18:18.409	<0.0166 ± 0.0055	<0.0166	0.0055	<0.0140 ± 0.0047	<0.0140	0.0047	⋯	⋯
EDJ2009-156-B	03:28:51.111	+31:18:15.443	0.0175 ± 0.0054	0.0200	0.0055	0.0295 ± 0.0042	0.0362	0.0046	1.15 ± 0.75	1.31 ± 0.67
EDJ2009-172	03:28:56.649	+31:18:35.449	0.0297 ± 0.0068	0.0271	0.0074	<0.0242 ± 0.0080	<0.0242	0.0080	<−0.45 ± 0.89	<−0.26 ± 0.95
EDJ2009-173	03:28:56.963	+31:16:22.199	<0.0152 ± 0.0051	<0.0152	0.0051	0.0316 ± 0.0048	0.0352	0.0044	>1.60 ± 0.81	>1.84 ± 0.78
SVS13A2	03:29:03.386	+31:16:01.622	0.0743 ± 0.0056	0.0768	0.0050	0.1023 ± 0.0051	0.0938	0.0041	0.70 ± 0.20	0.44 ± 0.17
IRAS4B’	03:29:12.841	+31:13:06.893	<0.0146 ± 0.0049	<0.0146	0.0049	<0.0119 ± 0.0040	<0.0119	0.0040	⋯	⋯

Table 3
(Continued)

Name	R.A. (J2000)	Decl. (J2000)	$F_{\nu,\mathrm{int}}$[a] (6.4 cm) (mJy)	$F_{\nu,\mathrm{peak}}$[b] (6.4 cm) (mJy beam^{-1})	rms (6.4 cm) (mJy beam^{-1})	$F_{\nu,\mathrm{int}}$[a] (4.1 cm) (mJy)	$F_{\nu,\mathrm{peak}}$[b] (4.1 cm) (mJy beam^{-1})	rms (4.1 cm) (mJy beam^{-1})	Sp. Index Int.[c]	Sp. Index Peak[d]
EDJ2009-233	03:29:17.675	+31:22:44.922	0.1002 ± 0.0078	0.0794	0.0052	0.1161 ± 0.0059	0.1004	0.0043	0.33 ± 0.21	0.52 ± 0.17
EDJ2009-235	03:29:18.258	+31:23:19.758	0.0192 ± 0.0056	0.0199	0.0051	<0.0121 ± 0.0040	<0.0121	0.0040	<−1.01 ± 0.97	<−1.10 ± 0.93
SVS3	03:29:10.419	+31:21:59.072	0.6720 ± 0.0136	0.4126	0.0056	0.7219 ± 0.0268	0.4945	0.0051	0.16 ± 0.09	0.40 ± 0.04
SVS3-A	03:29:10.419	+31:21:59.072	0.2562 ± 0.0074	0.2188	0.0056	0.2005 ± 0.0183	0.1700	0.0052	−0.54 ± 0.21	−0.56 ± 0.09
SVS3-B	03:29:10.369	+31:21:58.963	0.4158 ± 0.0062	0.4126	0.0056	0.5213 ± 0.0085	0.4945	0.0051	0.50 ± 0.05	0.40 ± 0.04

Notes. Flag −77 is used when non-detection results from the source being unresolved.

[a] $F_{\nu,\mathrm{int}}$—Integrated flux resulting from area under 2D Gaussian fit to the source.

[b] $F_{\nu,\mathrm{peak}}$—Peak value of the flux density on the source.

[c] Sp. Index (Int.)—Spectral index calculated with the integrated flux.

[d] Sp. Index (Peak)—Spectral index calculated with the peak flux.

(This table is available in machine-readable form.)

Table 4
Young Stellar Object Candidates

Name[a]	R.A. (J2000)	Decl. (J2000)	$F_{\nu,\mathrm{int}}$ (6.4 cm) (mJy)	$F_{\nu,\mathrm{peak}}$ (6.4 cm) (mJy beam^{-1})	rms (6.4 cm) (mJy beam^{-1})	$F_{\nu,\mathrm{int}}$ (4.1 cm) (mJy)	$F_{\nu,\mathrm{peak}}$ (4.1 cm) (mJy beam^{-1})	rms (4.1 cm) (mJy beam^{-1})	Sp. Index Int.	Sp. Index Peak
FOW2011-6	03:44:20.41	+32:01:58.65	1.0652 ± 0.0290	0.7647	0.0199	…	…	…	…	…
2MASSJ03283692	03:28:36.95	+31:17:35.28	0.3637 ± 0.0296	0.2805	0.0250	…	…	…	…	…
RAC97-VLA38	03:28:50.74	+31:22:25.27	1.5280 ± 0.0247	1.1583	0.0176	…	…	…	…	…
2MASSJ03285097	03:28:50.98	+31:23:47.85	0.7210 ± 0.0216	0.5409	0.0162	…	…	…	…	…
2MASSJ03290031	03:29:00.33	+31:13:38.49	0.0895 ± 0.0133	0.0882	0.0128	…	…	…	…	…
2MASSJ03290462	03:29:04.62	+31:20:28.74	<0.0203 ± 0.0068	<0.0203	0.0068	0.0347 ± 0.0064	0.0391	0.0064	>1.18 ± 0.84	>1.44 ± 0.36
OTS2008-68	03:29:15.88	+31:16:21.49	0.1270 ± 0.0112	0.0844	0.0068	0.0943 ± 0.0372	0.0410	0.0095	−0.66 ± 0.89	−1.59 ± 0.54
RAC97-VLA31	03:29:16.62	+31:16:48.83	0.1006 ± 0.0072	0.1026	0.0073	0.0656 ± 0.0106	0.0796	0.0115	−0.94 ± 0.39	−0.56 ± 0.36
Cl*IC348LRL49	03:43:57.61	+32:01:37.38	0.4191 ± 0.0067	0.4135	0.0059	0.4043 ± 0.0070	0.3981	0.0061	−0.08 ± 0.05	−0.08 ± 0.05
GMM2008-38	03:29:22.27	+31:13:54.37	0.3824 ± 0.0362	0.2791	0.0152	…	…	…	…	…
EDJ2009-374	03:44:05.87	+32:00:29.57	<0.0191 ± 0.0064	<0.0191	0.0064	0.0314 ± 0.0075	0.0411	0.0066	>1.09 ± 0.90	>1.69 ± 0.36
EDJ2009-182	03:28:59.27	+31:20:35.8	0.0457 ± 0.0075	0.0430	0.0054	0.0310 ± 0.0058	0.0301	0.0047	−0.85 ± 0.54	−0.78 ± 0.44
EDJ2009-186	03:29:01.63	+31:20:18.78	0.0561 ± 0.0084	0.0379	0.0055	0.0583 ± 0.0203	0.0190	0.0049	0.08 ± 0.83	−1.52 ± 0.66
EDJ2009-202	03:29:05.77	+31:16:39.58	0.0546 ± 0.0080	0.0461	0.0065	0.0940 ± 0.0067	0.0763	0.0057	1.20 ± 0.36	1.11 ± 0.35
EDJ2009-175	03:28:57.14	+31:14:20.9	0.0792 ± 0.0137	0.0854	0.0081	0.0779 ± 0.0112	0.0643	0.0087	−0.04 ± 0.50	−0.63 ± 0.36
EDJ2009-314	03:41:57.46	+31:48:36.54	<0.0146 ± 0.0049	<0.0146	0.0049	0.0299 ± 0.0054	0.0284	0.0040	>1.58 ± 0.84	>1.46 ± 0.31
EDJ2009-247	03:29:26.83	+31:26:47.31	0.0558 ± 0.0102	0.0454	0.0073	0.0599 ± 0.0344	0.0421	0.0104	0.15 ± 1.33	−0.17 ± 0.65
EDJ2009-374	03:44:05.87	+32:00:29.57	<0.0191 ± 0.0064	<0.0191	0.0064	0.0314 ± 0.0075	0.0411	0.0066	<1.09 ± 0.90	<1.69 ± 0.36
EDJ2009-182	03:28:59.27	+31:20:35.8	0.0457 ± 0.0075	0.0430	0.0054	0.0310 ± 0.0058	0.0301	0.0047	−0.85 ± 0.54	−0.78 ± 0.44
EDJ2009-186	03:29:01.63	+31:20:18.78	0.0561 ± 0.0084	0.0379	0.0055	0.0583 ± 0.0203	0.0190	0.0049	0.08 ± 0.83	−1.52 ± 0.66
EDJ2009-202	03:29:05.77	+31:16:39.58	0.0546 ± 0.0080	0.0461	0.0065	0.0940 ± 0.0067	0.0763	0.0057	1.20 ± 0.36	1.11 ± 0.35
EDJ2009-175	03:28:57.14	+31:14:20.9	0.0792 ± 0.0137	0.0854	0.0081	0.0779 ± 0.0112	0.0643	0.0087	−0.04 ± 0.50	−0.63 ± 0.36
EDJ2009-314	03:41:57.46	+31:48:36.54	<0.0146 ± 0.0049	<0.0146	0.0049	0.0299 ± 0.0054	0.0284	0.0040	<1.58 ± 0.84	<1.46 ± 0.31
EDJ2009-247	03:29:26.83	+31:26:47.31	0.0558 ± 0.0102	0.0454	0.0073	0.0599 ± 0.0344	0.0421	0.0104	0.15 ± 1.33	−0.17 ± 0.65

Note.

[a] References. FOW2011—Forbrich et al. (2011), RAC97—Rodríguez et al. (1999), 2MASS—2-Micron All Sky Survey (Cutri et al. (2003)), l*IC348LRL—Luhman et al. (1998), EDJ2009—Evans et al. (2009), OTS2008—Oasa et al. (2008), GMM2008—Gutermuth et al. (2008).

Table 5
Known Non-protostellar Sources

Type[a]	Name[b]	R.A. (J2000)	Decl. (J2000)	$F_{\nu,\rm int}$ (6.4 cm) (mJy)	$F_{\nu,\rm peak}$ (6.4 cm) (mJy/b)	rms (6.4 cm) (mJy/b)	$F_{\nu,\rm int}$ (4.1 cm) (mJy)	$F_{\nu,\rm peak}$ (4.1 cm) (mJy/b)	rms (4.1 cm) (mJy/b)	Sp. Index Int.	Sp. Index Peak
*iC	Cl*IC348LRL1888	03:44:19.78	+31:59:18.85	0.0535 ± 0.0073	0.0454	0.0055	0.0507 ± 0.0064	0.0426	0.0045	−0.11 ± 0.41	−0.14 ± 0.35
Rad	FOW2011-7	03:44:31.47	+32:00:39.43	0.3100 ± 0.0455	0.0685	0.0067	0.1292 ± 0.0608	0.0312	0.0077	−1.93 ± 1.08	−1.37 ± 0.59
*	PSZ2003J034436.5	03:44:36.46	+32:03:13.60	0.1227 ± 0.0147	0.1019	0.0108	<0.0910 ± 0.0303	<0.0910	0.0303	<−0.66 ± 0.78	<−0.25 ± 0.77
X	CXOPZ134	03:44:36.90	+32:01:23.30	1.1031 ± 0.0188	0.9293	0.0131	…	…	…	…	…
Rad	RAC97-VLA37	03:28:37.2	+31:21:25.45	0.5419 ± 0.0148	0.4454	0.0121	…	…	…	…	…
X	WMW2010120	03:28:59.66	+31:25:42.88	0.1378 ± 0.0125	0.1207	0.0109	0.1812 ± 0.1133	0.1366	0.0409	0.60 ± 1.39	0.27 ± 0.69
Rad	RAC97-VLA32	03:29:20.70	+31:15:49.69	0.7378 ± 0.0531	0.4459	0.0346	…	…	…	…	…
Rad	FOW201126	03:29:30.93	+31:22:11.85	1.2263 ± 0.0273	0.8864	0.0180	…	…	…	…	…
X	XMMUJ032821.5	03:28:21.39	+31:14:40.26	0.5440 ± 0.0171	0.4205	0.0142	…	…	…	…	…
Rad	RAC97VLA36	03:28:32.79	+31:14:45.71	0.4585 ± 0.0721	0.1196	0.0276	…	…	…	…	…
Rad	RAC97VLA12	03:28:59.85	+31:14:02.89	0.1897 ± 0.0137	0.1609	0.0127	…	…	…	…	…
cor	EYG2006Bolo3	03:25:10.49	+30:44:47.48	<0.0195 ± 0.0065	<0.0195	0.0065	0.0323 ± 0.0082	0.0449	0.0074	>1.11 ± 0.92	>1.84 ± 0.36
Rad	AR2002IRS2VLA1	03:25:18.58	+30:44:36.94	0.3649 ± 0.0296	0.1616	0.0082	0.2773 ± 0.1057	0.0506	0.0139	−0.60 ± 0.86	−1.45 ± 0.77
Rad	AR2002IRS2VLA3	03:25:22.07	+30:46:05.48	1.1928 ± 0.0570	0.0474	0.0073	<0.4628 ± 0.0098	<0.0295	0.0098	<−2.09 ± 0.15	<−2.09 ± 0.06
Rad	AR2002IRS2VLA5	03:25:31.91	+30:44:37.97	0.2020 ± 0.0190	0.1690	0.0155	…	…	…	…	…
Rad	NVSSJ033009+303248	03:30:09.10	+30:32:49.70	62.0973 ± 0.3761	42.6842	0.0252	…	…	…	…	…
IR	SSTc2dJ033046.4	03:30:46.37	+30:32:43.19	0.2872 ± 0.0230	0.2261	0.0191	…	…	…	…	…
Rad	NVSSJ032742+301140-E	03:27:41.49	+30:11:47.14	8.6257 ± 0.3190	1.3899	0.0127	…	…	…	…	…
X	XMMUJ032742.2	03:27:42.25	+30:11:39.84	0.2220 ± 0.0113	0.2241	0.0117	…	…	…	…	…
Rad	NVSSJ032742+301140-W	03:27:42.76	+30:11:33.99	7.2426 ± 0.3638	0.4162	0.0111	…	…	…	…	…
Rad	NVSSJ032744+300717-N	03:27:43.98	+30:07:18.68	12.7310 ± 1.4865	0.5025	0.0155	…	…	…	…	…
Rad	NVSSJ032744+300717-S	03:27:44.16	+30:07:15.02	<0.0210 ± 0.0070	<0.0210	0.0070	0.8259 ± 0.1140	0.5452	0.0104	>8.09 ± 0.79	>7.18 ± 0.04
Rad	NVSSJ032804+300820	03:28:04.86	+30:08:19.65	13.7439 ± 0.1846	8.0450	0.0259	…	…	…	…	…
Rad	NVSSJ032827+302616-N	03:28:27.50	+30:26:18.52	8.5889 ± 1.0183	2.6233	0.0189	…	…	…	…	…
Rad	NVSSJ032827+302616-S	03:28:27.52	+30:26:12.55	19.7856 ± 0.2594	10.7675	0.0181	…	…	…	…	…
Rad	RAC97-VLA23	03:29:07.17	+31:17:08.98	0.0774 ± 0.0078	0.0616	0.0056	0.0611 ± 0.0200	0.0335	0.0057	−0.52 ± 0.76	−1.34 ± 0.43
X	GFT200276	03:29:15.64	+31:18:51.78	0.0585 ± 0.0066	0.0579	0.0060	0.0494 ± 0.0060	0.0398	0.0047	−0.38 ± 0.37	−0.83 ± 0.35
Rad	RAC97-VLA35	03:29:23.89	+31:16:20.68	0.4748 ± 0.0469	0.0463	0.0107	<0.3431 ± 0.0376	<0.1127	0.0376	<−0.72 ± 0.77	<0.50 ± 0.78
IR	2MASSJ03283173+3059158	03:28:31.75	+30:59:15.79	0.0405 ± 0.0072	0.0378	0.0057	0.0446 ± 0.0061	0.0472	0.0055	0.21 ± 0.49	0.49 ± 0.42
Rad	RZP2014JVLA4	03:43:57.08	+32:03:29.64	0.0619 ± 0.0067	0.0595	0.0056	0.0341 ± 0.0052	0.0400	0.0052	−1.31 ± 0.41	−0.88 ± 0.35
Rad	RZP2014JVLA7	03:44:01.66	+32:04:39.53	0.0475 ± 0.0071	0.0502	0.0066	0.0378 ± 0.0200	0.0334	0.0082	−0.50 ± 1.21	−0.90 ± 0.61
Rad	NVSSJ032628+301618	03:26:28.36	+30:16:18.72	24.8228 ± 0.6660	11.3131	0.0055	13.1329 ± 0.2796	5.5648	0.0054	−1.40 ± 0.08	−6.81 ± 0.02
X	XMMUJ032643.8	03:26:43.79	+30:08:23.77	16.2594 ± 0.2031	10.2420	0.0282	…	…	…	…	…
PoC	LMG94Per7C	03:32:29.00	+31:02:12.15	<0.0152 ± 0.0051	<0.0152	0.0051	0.0151 ± 0.0048	0.0242	0.0039	>−0.00 ± 1.02	>1.03 ± 0.36
Rad	NVSSJ033119+304726	03:31:19.07	+30:47:27.70	35.9500 ± 1.8061	8.5635	0.0074	16.6793 ± 0.6315	3.7696	0.0054	−1.69 ± 0.14	−0.33 ± 0.01
TT*	Cl*IC348LRL1939	03:44:52.74	+32:00:56.39	<0.0166 ± 0.0055	<0.0166	0.0055	0.0310 ± 0.0051	0.0331	0.0050	>1.37 ± 0.82	>1.52 ± 0.33
*	PSZ2003J034453.0	03:44:52.98	+32:05:07.62	0.4971 ± 0.0089	0.4573	0.0083	0.4946 ± 0.0173	0.4533	0.0154	−0.01 ± 0.09	−0.02 ± 0.09
*	PSZ2003J034453.9	03:44:53.85	+32:04:36.18	0.2244 ± 0.0096	0.1855	0.0076	0.1542 ± 0.0149	0.1285	0.0120	−0.83 ± 0.23	−0.81 ± 0.22
*iC	IC34818	03:45:07.73	+32:00:27.18	0.1370 ± 0.0142	0.1144	0.0116	…	…	…	…	…
TT*	Cl*IC348LRL11	03:45:07.98	+32:04:01.82	0.3662 ± 0.0187	0.2654	0.0144	…	…	…	…	…
Rad	RR98HH366VLA2	03:47:27.68	+32:52:30.57	0.2346 ± 0.0068	0.2518	0.0063	0.1524 ± 0.0079	0.1487	0.0075	−0.95 ± 0.13	−1.16 ± 0.12
PoC	KJT20073	03:47:42.61	+32:52:27.30	<0.0147 ± 0.0049	<0.0147	0.0049	0.0283 ± 0.0047	0.0306	0.0039	>1.45 ± 0.82	>1.61 ± 0.28
Rad	RR98HH366VLA4	03:47:52.55	+32:52:01.11	1.8373 ± 0.0071	1.7049	0.0056	1.3871 ± 0.0075	1.2874	0.0056	−0.62 ± 0.01	−0.62 ± 0.01
X	CXOUJ034426.1	03:44:26.18	+32:01:13.76	0.0797 ± 0.0122	0.0976	0.0145	…	…	…	…	…
Or*	CXOPZ32	03:44:16.76	+32:09:56.66	2.4096 ± 0.0305	1.3464	0.0115	0.5116 ± 0.0591	0.3168	0.0378	−3.41 ± 0.26	−3.19 ± 0.26
Or*	V*V904Per	03:44:21.66	+32:06:24.78	0.0465 ± 0.0062	0.0482	0.0057	0.0323 ± 0.0060	0.0315	0.0050	−0.80 ± 0.50	−0.94 ± 0.44

Table 5
(Continued)

Type[a]	Name[b]	R.A. (J2000)	Decl. (J2000)	$F_{\nu,\mathrm{int}}$ (6.4 cm) (mJy)	$F_{\nu,\mathrm{peak}}$ (6.4 cm) (mJy/b)	rms (6.4 cm) (mJy/b)	$F_{\nu,\mathrm{int}}$ (4.1 cm) (mJy)	$F_{\nu,\mathrm{peak}}$ (4.1 cm) (mJy/b)	rms (4.1 cm) (mJy/b)	Sp. Index Int.	Sp. Index Peak
*iC	Cl*IC348MM42	03:44:21.74	+32:09:18.51	0.4483 ± 0.0198	0.3059	0.0096	0.1984 ± 0.0272	0.1501	0.0213	−1.80 ± 0.32	−1.57 ± 0.32
*iC	Cl*IC348MM41	03:44:22.17	+32:09:23.76	0.4219 ± 0.0197	0.2618	0.0099	0.1928 ± 0.0970	0.0942	0.0234	−1.73 ± 1.11	−2.25 ± 0.55
dS*	V*V705Per	03:44:31.19	+32:06:22.04	0.1957 ± 0.0083	0.1759	0.0071	0.1494 ± 0.0090	0.1577	0.0089	−0.59 ± 0.16	−0.24 ± 0.15
Or*	V*V913Per	03:44:32.57	+32:08:42.44	0.2461 ± 0.0126	0.2164	0.0110	0.2289 ± 0.0929	0.1531	0.0327	−0.16 ± 0.90	−0.76 ± 0.48
Or*	V*V914Per	03:44:32.73	+32:08:37.45	0.2708 ± 0.0136	0.2299	0.0108	0.2905 ± 0.0859	0.1391	0.0313	0.15 ± 0.66	−1.11 ± 0.51
**	Cl*IC348LRL9	03:44:39.14	+32:09:18.40	0.7142 ± 0.0285	0.4445	0.0189	…	…	…	…	…
Rad	RAC97VLA15	03:29:02.55	+31:13:44.37	0.0632 ± 0.0104	0.0659	0.0108	<0.0960 ± 0.0320	<0.0960	0.0320	<0.92 ± 0.82	<0.83 ± 0.82
X	GFT200299	03:29:25.89	+31:13:44.81	0.0370 ± 0.0067	0.0416	0.0063	0.0347 ± 0.0193	0.0350	0.0078	−0.14 ± 1.29	−0.38 ± 0.60
IR	ASR98	03:28:58.54	+31:12:21.00	<0.0205 ± 0.0068	<0.0205	0.0068	0.0242 ± 0.0063	0.0341	0.0057	>0.37 ± 0.93	>1.12 ± 0.37
IR	WISEJ034158.52	03:41:58.45	+31:48:56.35	0.0358 ± 0.0053	0.0334	0.0049	0.0361 ± 0.0046	0.0397	0.0040	0.02 ± 0.43	0.38 ± 0.39
*	MBO184	03:29:13.49	+31:24:40.56	0.0383 ± 0.0062	0.0378	0.0054	0.0381 ± 0.0138	0.0272	0.0047	−0.01 ± 0.87	−0.73 ± 0.50
BD*	2MASSJ03293053	03:29:30.54	+31:27:27.78	0.0799 ± 0.0066	0.0785	0.0056	0.0867 ± 0.0054	0.0988	0.0060	0.18 ± 0.23	0.51 ± 0.21
Rad	RAC97VLA6	03:28:52.50	+31:14:59.49	0.0427 ± 0.0063	0.0440	0.0062	0.0372 ± 0.0149	0.0285	0.0062	−0.30 ± 0.94	−0.95 ± 0.57

Notes.

[a] Types from the SIMBAD catalog: Rad—radio source; *iC—star in cluster; *—star; X—X-ray source; IR—infrared source; PoC—Part of Cloud; TT*—T-Tauri star; Or*—variable star of Orion type; dS*—variable star of delta Sct type; **—double or multiple star.

[b] References. Cl*IC348LRL—Luhman et al. (1998), FOW2011—Forbrich et al. (2011), PSZ2003—Preibisch et al. (2003), CXOPZ—Preibisch & Zinnecker (2001), RAC97—Rodríguez et al. (1999), WMW2010—Winston et al. (2010), XMMU—*XMM-Newton* data Unregistered, EYG2006—(Enoch et al. 2006), AR2002—Anglada & Rodríguez (2002), NVSS—The NRAO VLA Sky Survey (Condon et al. 1998), SSTc2d—Spitzer c2d Legacy (Young et al. 2004), GFT2002—Getman et al. (2002), 2MASS—Two Micron All-Sky Survey (Cutri et al. 2003), RZP2014—Rodríguez et al. (2014), LMG94—Ladd et al. (1994), RR98—Rodríguez & Reipurth (1998), KJT2007—Kirk et al. (2007), V*VXXX—General Catalog of Variable Stars (Kukarkin et al. 1971), ASR—Aspin et al. (1994), MBO—Wilking et al. (2004).

Table 6
New Detections Reported in Pech et al. (2016)

Name	R.A. (J2000)	Decl. (J2000)	$F_{\nu,\mathrm{int}}$ (6.4 cm) (mJy)	$F_{\nu,\mathrm{peak}}$ (6.4 cm) (mJy/b)	rms (6.4 cm) (mJy/b)	$F_{\nu,\mathrm{int}}$ (4.1 cm) (mJy)	$F_{\nu,\mathrm{peak}}$ (4.1 cm) (mJy/b)	rms (4.1 cm) (mJy/b)	Sp. Index Int.	Sp. Index Peak
J032903.14+312752.6	03:29:03.16	+31:27:52.58	0.0885 ± 0.0132	0.0983	0.0151	…	…	…	…	…
J032819.46+311831.0	03:28:19.48	+31:18:31.20	0.7570 ± 0.0345	0.4897	0.0223	…	…	…	…	…
J032825.98+311616.0	03:28:25.99	+31:16:16.07	0.3582 ± 0.0106	0.2967	0.0088	0.1343 ± 0.0193	0.1180	0.0167	−2.16 ± 0.32	−2.03 ± 0.32
J032832.41+311245.3	03:28:32.43	+31:12:45.52	0.1830 ± 0.0213	0.1566	0.0204	…	…	…	…	…
J034327.28+320028.1	03:43:27.31	+32:00:28.34	0.1417 ± 0.0172	0.1319	0.0148	…	…	…	…	…
J034330.40+320758.4	03:43:30.42	+32:07:58.84	0.2882 ± 0.0204	0.2194	0.0172	…	…	…	…	…
J034342.10+320225.2	03:43:42.11	+32:02:25.34	0.1072 ± 0.0094	0.0953	0.0077	0.0733 ± 0.0356	0.0495	0.0120	−0.84 ± 1.09	−1.44 ± 0.56
J034448.89+320125.0	03:44:48.89	+32:01:25.07	0.1212 ± 0.0064	0.1143	0.0051	0.0816 ± 0.0055	0.0670	0.0041	−0.87 ± 0.19	−1.18 ± 0.17
J034459.29+315658.9	03:44:59.26	+31:56:59.22	0.7574 ± 0.0487	0.1376	0.0133	…	…	…	…	…
J034423.11+320956.3	03:44:23.9	+32:09:56.45	1.4929 ± 0.0183	1.1440	0.0119	…	…	…	…	…
J032909.64+311450.5	03:29:09.67	+31:14:50.65	0.0991 ± 0.0167	0.0855	0.0139	…	…	…	…	…
J032907.13+312635.2	03:29:07.14	+31:26:35.32	0.0936 ± 0.0090	0.0820	0.0079	0.1235 ± 0.0368	0.0746	0.0130	0.61 ± 0.69	−0.21 ± 0.44

Table 7
New Detections from VANDAM Survey

Name	R.A. (J2000)	Decl. (J2000)	$F_{\nu,\mathrm{int}}$ (6.4 cm) (mJy)	$F_{\nu,\mathrm{peak}}$ (6.4 cm) (mJy/b)	rms (6.4 cm) (mJy/b)	$F_{\nu,\mathrm{int}}$ (4.1 cm) (mJy)	$F_{\nu,\mathrm{peak}}$ (4.1 cm) (mJy/b)	rms (4.1 cm) (mJy/b)	Sp. Index Int.	Sp. Index Peak
034357.31+315858.86	03:43:57.31	+31:58:58.86	0.0604 ± 0.0101	0.0624	0.0100	<0.0850 ± 0.0283	<0.0850	0.0283	<0.75 ± 0.82	<0.68 ± 0.82
034408.82+320020.63	03:44:08.82	+32:00:20.64	0.0439 ± 0.0069	0.0406	0.0060	0.0441 ± 0.0173	0.0286	0.0062	0.01 ± 0.93	−0.77 ± 0.58
034415.23+315749.09	03:44:15.24	+31:57:49.09	0.0747 ± 0.0075	0.0694	0.0065	0.1245 ± 0.0076	0.1177	0.0070	1.13 ± 0.26	1.16 ± 0.24
034422.04+320322.79	03:44:22.05	+32:03:22.79	<0.0208 ± 0.0069	<0.0208	0.0069	0.0446 ± 0.0073	0.0561	0.0084	>1.68 ± 0.82	>2.19 ± 0.33
034425.40+320249.66	03:44:25.41	+32:02:49.66	0.0367 ± 0.0066	0.0421	0.0067	0.0459 ± 0.0181	0.0308	0.0076	0.49 ± 0.96	−0.69 ± 0.65

(This table is available in its entirety in machine-readable form.)

3. Results

3.1. Detections

From the targeted protostars in Table 1, we report detections in C-band for 60 out of 95 systems (63%) in either 4.1 or 6.4 cm. Specifically, 31 out of 46 Class 0 (67%) and 21 out of 37 Class I (56%) protostars were detected. We also detect 9 of 12 (75%) of targeted Class II systems, but this sample is smaller and biased toward more embedded sources. Out of all systems, 23 have multiple stellar components (21 binary and two triple systems) as identified by Tobin et al. (2016); three of those are unresolved in C-band, which results in 117 targeted individual protostars. We detect 11 components of multiple systems (six Class 0, three Class I, and two Class II). Thus, the total number of protostars with measured flux in at least one of the wavelengths in C-band is 71, making a detection rate of 61% with 37/57 (65%) Class 0, 24/45 (53%) Class I, and 10/15 (75%) Class II protostars. For known protostars that were not detected, we used 3σ upper limits based on the rms of the field, corrected for the primary beam attenuation.

For binary systems, we additionally calculated the combined flux of all components, for comparison with parameters that were obtained for unresolved systems. For example, when comparing with outflow force, it is not possible to determine which of the close companions is the outflow driving source, and the same applies to the bolometric luminosity. Far-infrared observations have lower resolution than is available with interferometry, so one obtains the luminosity of both components. However, when comparing with bolometric temperature, we compare the flux densities separately for each component of the multiple system, assuming that both companions are at the same evolutionary stage, which is generally a good assumption (Murillo et al. 2016). A summary of the measured flux densities and spectral indices is presented in Table 3.

Apart from the targeted protostars, we serendipitously detected a plethora of radio sources within the large C-band primary beam. All of them were compared with the SIMBAD catalog. Some of them had been detected previously, and 17 sources from this sample were marked by various authors as YSO candidates. Due to their tentative classification, they are not considered in the further analysis. However, we note that eight of them have positive radio spectral indices in the C-band, as would be expected for protostars. The more evolved pre-main sequence stars may exhibit negative indices (e.g., Dzib et al. 2013), and distinguishing them from extragalactic sources is difficult by means of spectral index, thus making cross-matched catalogs important. The summary of the sources with possible protostellar nature is presented in Table 4.

In Table 5, we present 59 previously detected sources of various nature, including 16 stars (2 T-Tauri stars), 27 radio, 8 X-ray, 4 infrared unclassified radio sources, 1 brown dwarf, and 3 associated with starless cores. Negative spectral indices prevail in this sample, indicating non-thermal processes. For stars, the non-thermal emission is probably related to coronal activity, while for unclassified sources it would point to their extragalactic nature. Pech et al. (2016) reported new detections for 12 sources; we list them in Table 6.

Across the entire sample, we detect 490 new sources. Table 7 lists these new detections. We assume that most of them are extragalactic. To test this, we estimate the expected quantity of extragalactic sources based on the equations from Anglada et al. (1998) (see their Appendix) derived from number counts of radio sources (Condon 1984; Rodríguez et al. 1989b). For a detection threshold F_λ, the expected number of extragalactic sources per primary beam is:

$$N_{6.4} = 1.15\ F_{6.4}^{-0.75} \tag{1}$$

$$N_{4.1} = 0.40\ F_{4.1}^{-0.75}. \tag{2}$$

With the 6σ threshold used in the source finder, we obtain values of:

$$N_{6.4} \sim 16,\ \text{ for } F_{6.4} \geqslant 30\ \mu\text{Jy}, \tag{3}$$

$$N_{4.1} \sim 7,\ \text{ for } F_{4.1} \geqslant 24\ \mu\text{Jy}. \tag{4}$$

For the new detections, we find average numbers of $N_{6.4} \sim 15$ and $N_{4.1} \sim 11$ per field. These average values are broadly consistent with the expected number of extragalactic sources, although the 4.1 cm value is a bit high. This estimate depends on an assumed spectral index of the extragalactic sources ($\alpha = -0.7$). If some of the sources have flatter indices, we would expect even more of them to be detected at 4.1 cm than predicted.

3.2. Flux Densities from Protostars

Figure 1 shows histograms of flux densities at 4.1 and 6.4 cm from the known protostars. We use the log-rank test to estimate probabilities for Class 0 and Class I fluxes to be drawn from the same sample. We obtain high probabilities of 64% and 54% for 4.1 cm and 6.4 cm, respectively, consistent with there being no difference between the two samples. This result, combined with there being no significant difference between the fraction of detected protostars (65% for Class 0 and 53% for Class I), indicates that the radio emission mechanism should not differ between the two evolutionary classes. This result might indicate that the thermal radio jets are not driven by the release of accretion energy, which is expected to decrease from Class 0 to Class I (Fischer et al. 2017). This is in agreement with Pech et al. (2016), who show consistent fluxes between Class 0 and Class I for a smaller sample of protostars. However, other sample-limited studies suggest that the radio emission mechanisms could be different for Class 0 and Class I protostars (AMI Consortium et al. 2011).

Figure 2 compares the C-band flux densities corrected for distance (radio luminosities: $L_\lambda = F_\lambda \times D^2$) with the bolometric luminosity and temperature of protostars. The bolometric luminosity is a marker of the protostellar mass and the current accretion rate, and the bolometric temperature is often used to infer protostellar evolutionary status. The values used here are taken from multiple works analyzing spectral energy distribution of protostars in Perseus (Enoch et al. 2009; Sadavoy et al. 2014; Young et al. 2015; Murillo et al. 2016). We find no correlation with the bolometric temperature, suggesting that the radio emission is independent of the evolutionary class. Previous studies (Dzib et al. 2013, 2015; Pech et al. 2016) are consistent with this result, at least for the Class 0 to Class II regime. On the other hand, the radio luminosity shows a weak correlation with the bolometric luminosity. The EM algorithm provides following fitting parameters:

$$\log(L_{4.1\ \text{cm}}) = (-2.78 \pm 0.07) + (0.70 \pm 0.10)\log(L_{\text{bol}}),\ \rho = 0.69, \tag{5}$$

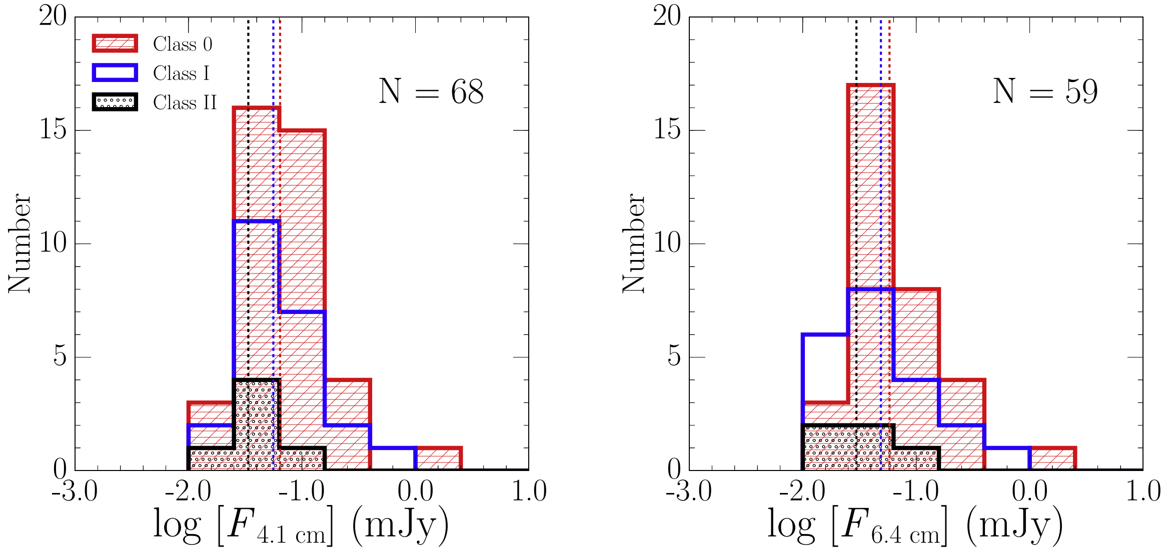

Figure 1. Distribution of flux densities for 4.1 cm (left) and 6.4 cm (right). Dashed lines show the median for each evolutionary class. The median values for 4.1 cm flux are 0.064, 0.056, and 0.034 mJy, for Class 0, Class I, and Class II. The median values for 6.4 cm flux are 0.058, 0.048, and 0.033 mJy for Class 0, Class I, and Class II.

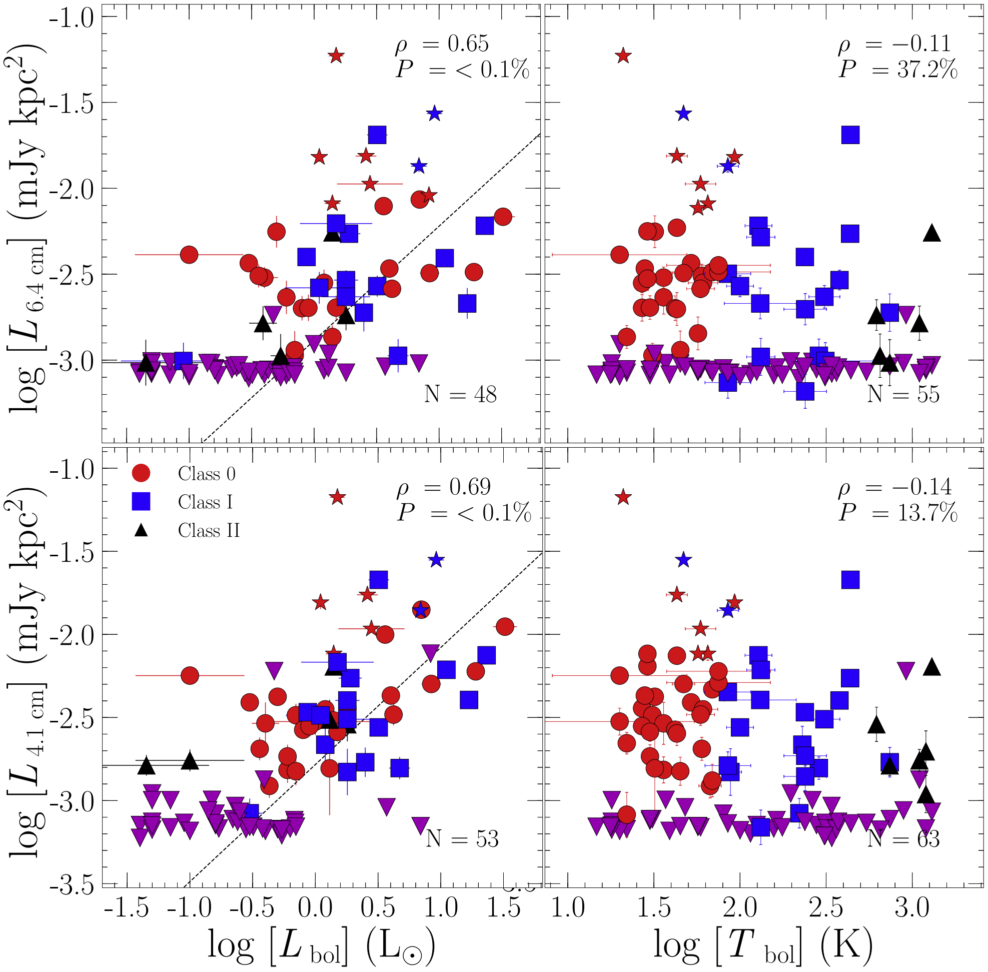

Figure 2. Luminosity at 4.1 cm (bottom) and 6.4 cm (top), compared with bolometric luminosity (left) and temperature (right). Spearman's rank correlation coefficient and probability of no correlation are shown in the top-right corner. Sources with resolved radio jets are marked as stars, and upper limits as magenta triangles.

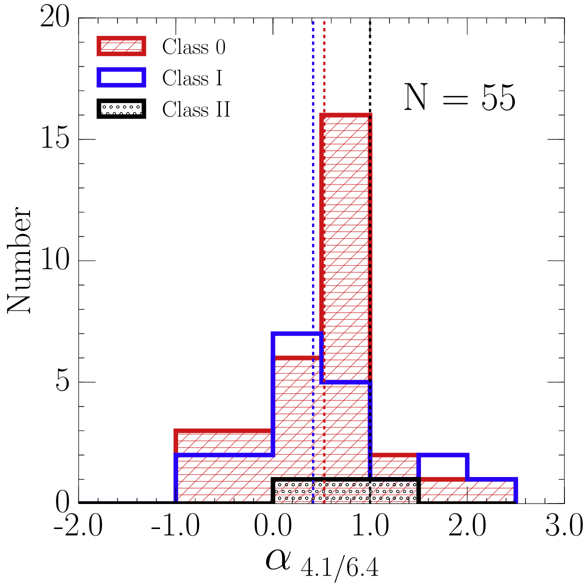

Figure 3. Distribution of spectral indices. Dashed lines show the median values for each evolutionary class. Median values are 0.52, 0.41, 0.99, 0.51 for Class 0, Class I, Class II, and the total sample, respectively. The statistical probability of Class 0 and Class I spectral indices to be drawn from the same sample is 58%.

$$\log(L_{6.4\,\mathrm{cm}}) = (-2.89 \pm 0.06) + (0.67 \pm 0.10)\log(L_{\mathrm{bol}}),\ \rho = 0.65. \quad (6)$$

3.3. Spectral Indices

With the two C-band fluxes, we calculate the radio spectral index, which is a reliable tool to discriminate between thermal and non-thermal emission processes. We measure the spectral index following:

$$\alpha = \frac{\ln(F_{\nu_1}/F_{\nu_2})}{\ln(\nu_1/\nu_2)}. \quad (7)$$

To calculate the spectral index errors, we use a standard propagation of error (Chiang et al. 2012).

Figure 3 shows histograms of the spectral indices for each evolutionary stage. The median values for each distribution are 0.52 for Class 0, 0.41 for Class I, and 0.99 for Class II; the overall median is 0.52. The result from a log-rank test for Class 0 and Class I gives a 58% probability of these two being drawn from the same sample, so there is no evidence of an evolutionary trend in the radio spectral indices. The median value for the total sample is in very good agreement with Shirley et al. (2007), who analyzed a sample of sources with wider range of luminosities and obtained a median index of 0.5. The median value is also similar to the expected spectral index of ~0.6 from an unresolved collimated wind (Reynolds 1986). The spectral index is also consistent with the value of 0.6 obtained for spherical winds of stars Panagia & Felli (1975). Thus, with a median value of $\alpha = 0.52$, we cannot determine the origin of the radio emission from the spectral index alone. Nevertheless, we can rule out some mechanisms from the radio emission. Rodríguez et al. (1993) conclude that highly negative spectral indices like $\alpha < -0.1$ are explained solely by synchrotron emission and cannot arise from free–free emission. Thus, it is important to list those protostellar sources that fall below the free–free regime. The sources with highly negative spectral indices are Per-emb-9 (-0.92 ± 0.63) and Per-emb-19 (-0.91 ± 0.49); they are Class 0 objects with low bolometric luminosity ($L_{\mathrm{bol}} < 0.6\,L_{\odot}$). The emission from these protostars is compact, but their signal to noise ratio is low, as indicated by the high error of the spectral index measurement, so they remain consistent with $\alpha > -0.1$ within 2σ uncertainty.

Figure 4 compares the observed spectral index with the radio luminosity for the known protostars in our sample. It is important to note that the most luminous radio sources (>0.01 mJy kpc^2) have spectral indices below the median for the whole sample, near the optically thin limit for the free–free emission, which is −0.1. We conclude that this is caused by the emission from optically thin regions of a jet. Interestingly, most of those sources exhibit resolved radio jets (Tychoniec et al. 2018), so lower spectral indices most likely come from the outflow positions where the emission is optically thin or non-thermal emission might contribute. Lower spectral indices from resolved jets were theoretically predicted by Reynolds (1986). The most luminous sources exhibit significantly less scatter than the lower-luminosity sources. This can be explained by shock ionization dominating the emission of the bright sources, while other, less prominent processes can contribute at low radio luminosities.

We also show the spectral index compared with bolometric luminosity and temperature in Figure 4. We find no correlation between bolometric temperature and spectral index, which suggests that the radio spectral index does not change systematically with protostellar evolution. We found a similar result in Figure 3. A trend in spectral indices with increasing bolometric luminosity can be noted by eye. Removing the four outliers and ignoring upper and lower limits seems to give more hints for correlation ($\rho = 0.49$, $P = 0.2\%$; see Figure 16 in Appendix A). On the other hand, including upper and lower limits in the statistical analysis casts doubt on any relation between the two values ($\rho = 0.12$, $P = 50\%$). This relation was also investigated by Shirley et al. (2007), with the conclusion that the optical depth of the emission is not dependent on the source luminosity. Their sample of sources with obtained spectral indices included only three sources with $L_{\mathrm{bol}} > 100\,L_{\odot}$. Even if the relation is unclear, we suggest this requires further study. The enhanced capabilities of VLA, as demonstrated in this work, can be used in a more massive cloud, where protostars with a wider range of bolometric luminosity are present. This could show whether the free–free emission becomes optically thick for sources with more ionizing radiation.

3.4. Multiple Systems

The VANDAM survey detected a large number of multiple systems in the Perseus molecular cloud. Due to the superior Ka-band resolution, a detailed analysis of multiplicity was performed with the 8 mm and 1 cm VLA observations (Tobin et al. 2016). A total of 13 new systems with separations below 500 au were detected. Here, we examine the emission at longer wavelengths toward these close multiples.

3.4.1. Comments on Systems Below 30 au:

The VLA Ka-band data showed multiplicity on ~30 au scales toward three sources: Per-emb-2, Per-emb-5, and Per-emb-18. C-band observations offer lower resolution than Ka-band, which makes detection of the closest binaries impossible.

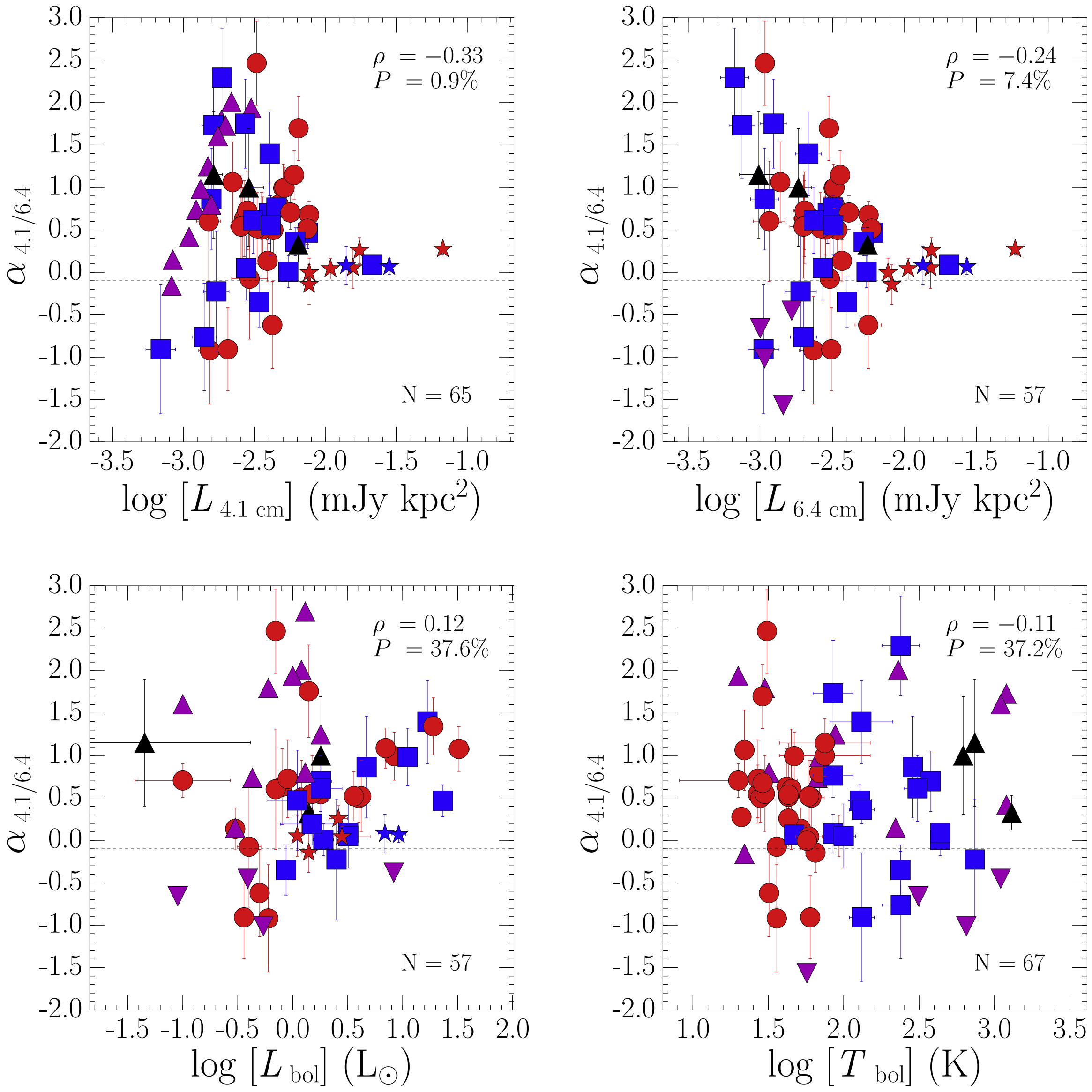

Figure 4. Spectral indices between 4.1 and 6.4 cm, compared with luminosity at 4.1 cm (top left) and 6.4 cm (top right) and with bolometric luminosity (bottom left) and temperature (bottom right). The dashed line indicates the minimum value of the spectral index for the free–free emission ($\alpha = -0.1$). Sources with resolved radio jets are marked as stars, upper limits as magenta triangles pointing down, and lower limits as magenta triangles pointing up.

We describe the C-band emission properties of those sources below.

Per-emb-2 appears slightly extended along the direction of the binary at 4.1 cm. The 6.4 cm map, however, is unresolved and peaks at the position of the Per-emb-2-B source. The spectral index map shows steeper values toward the Per-emb-2-A source, similar to the Ka-band resolved maps. Tobin et al. (2016) found a similarly steeper spectral index toward Per-emb-2-A from Ka-band data; they suggested that 2-B source is more affected by free–free emission. While unresolved, it appears that most of the C-band flux is aligned with the 2-B source but the S/N is low. Per-emb-5 is clearly detected only at 4.1 cm. Its emission is centered on the position of Per-emb-5-B, and its C-band spectral index is consistent with the flat values obtained in the Ka-band.

Per-emb-18 has a steep spectral index in the Ka-band, suggesting that the free–free emission is significantly contributing to the flux at the source position. This source has been identified as a resolved radio jet by VLA C-band observations with a position angle consistent with a large-scale H_2 outflow (Davis et al. 2008) and perpendicular to the position angle of the binary system (Tychoniec et al. 2018). The extended dust structure to the east of Per-emb-18 is seen only in the low-resolution Ka-band image, as noted by Tobin et al. (2016), and it is not detected in C-band, further suggesting that this clump is neither hosting a protostar nor powering a strong outflow.

3.4.2. Comments on Possible Close Multiples from VANDAM:

Tobin et al. (2016) reported four sources that had marginally resolved structures, but not significant enough to report a new detection. The Ka-band maps for EDJ2009-183 from Tobin et al. (2016) show extended emission that could be attributed to a protostellar component. This emission is marginally detected in the 4.1 cm map, indicating that it might a be faint thermal jet that is also supported by the C-band flat spectral index (0.05 ± 0.38). EDJ2009-156-B is completely unresolved in the C-band, but the spectral index suggests a significant

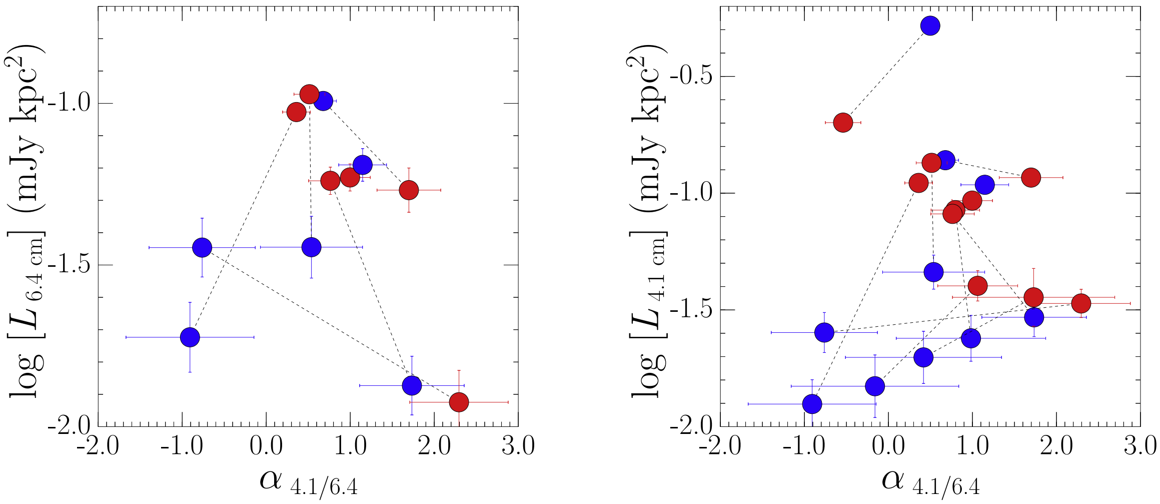

Figure 5. Plots showing 4.1 cm (left) and 6.4 cm (right) luminosity of the binary systems, compared with the spectral index. Red bullet represents the more luminous component of the binary in Ka-band observations (Tobin et al. 2016). Dashed lines are connecting components of the same system.

Table 8

Binary Systems

System	Separation ($''$)	Separation (au)	$\log(F_1/F_2)$ (6.4 cm)	$\log(F_1/F_2)$ (4.1 cm)	$\Delta\alpha$	$\log(M_{\mathrm{dust},1}/M_{\mathrm{dust},2})$
Per-emb-12	1.83	429.40	−0.28	−0.07	1.02	1.22
Per-emb-22	0.75	176.55	0.47	0.47	0.02	0.44
Per-emb-27	0.62	145.74	>0.59	0.55	>0.18	0.68
Per-emb-33 (A+C)	0.98	229.62	−0.73	<−1.04	>1.57	0.66
Per-emb-35	1.91	448.40	0.63	0.44	0.97	−0.17
Per-emb-40	0.39	91.92	0.70	0.95	1.27	0.64
Per-emb-44	0.30	70.53	−0.04	−0.07	0.15	0.51
Per-emb-49	0.31	73.52	−0.48	0.12	3.06	0.55
L1448NW	0.25	58.98	<0.03	0.43	<1.22	−0.01
EDJ2009-269	0.54	127.78	⋯	0.26	⋯	−0.10
SVS3	0.65	152.77	−0.21	−0.41	1.04	⋯

contribution of free–free emission to the Ka-band. Per-emb-25 is slightly extended in the 4.1 cm map. Interestingly it is peaked at the position of the possible companion, not at the well-detected primary source, making it a strong candidate for a binary. A steep spectral slope in the C-band does not indicate a large contribution from free–free emission. Per-emb-52 is a non-detection, preventing further interpretation of the Ka-band data.

3.4.3. Systems with Separation >30–500 au:

Tobin et al. (2016) found 19 systems with sources separated by 30 au to 500 au. We detect 10 (50%) of these systems in at least one of the C-band sub-bands. We also identify an additional source in SVS3 that was not detected in the Ka-band. A comparison of their fluxes, spectral indices, and dust masses is presented in Table 8. Some of the detected multiples have very similar fluxes, whereas one of the companions dominates the radio emission for others. There is no dependence between flux differences and separation. We also find variations in spectral index between the companions. While most of the compact dust differences are moderate, there is the notable example of Per-emb-12, where the A component has a mass $\sim$17 times greater than the B component. In the case of Per-emb-12, the B source has greater flux in the C-band, while in Ka-band the A companion is an order of magnitude brighter. Figure 5 illustrates the differences in flux densities and spectral index between the multiple systems.

3.5. Non-detections

Radio emission coincident with protostars is well-established as a common phenomenon. In this section, we investigate the nature of protostellar sources where we note the absence of emission at the C-band. The most natural explanation for the non-detection arises from the sensitivity of our observations. Even though our sensitivity is quite good, $\sim$5 μJy rms, we still may miss the lowest luminosity protostars. The correlation between radio and bolometric luminosity shows that sources with low bolometric luminosities should have lower C-band fluxes (Anglada 1995; Shirley et al. 2007). Indeed, most of our non-detections (except Per-emb-29 and Per-emb-21) have bolometric luminosities below 0.7 $L_{\odot}$. On the other hand, many of the sources below that threshold have significant radio flux. All the First Hydrostatic Starless Core candidates and Very Low Luminosity Objects: B1-bN (Hirano et al. 1999; Pezzuto et al. 2012; Gerin et al. 2015), Per-bolo-58 (Enoch et al. 2010), L1451-MMS (Pineda et al. 2011), Per-bolo-45 (Schnee et al. 2012), and L1448IRS2E (Chen et al. 2010), were not detected, probably due to their low luminosity. In contrast, Per-emb-29 and Per-emb-21 are not detected in our C-band observations. Per-emb-21 has $L_{\odot} = 6.9$, Per-emb-29

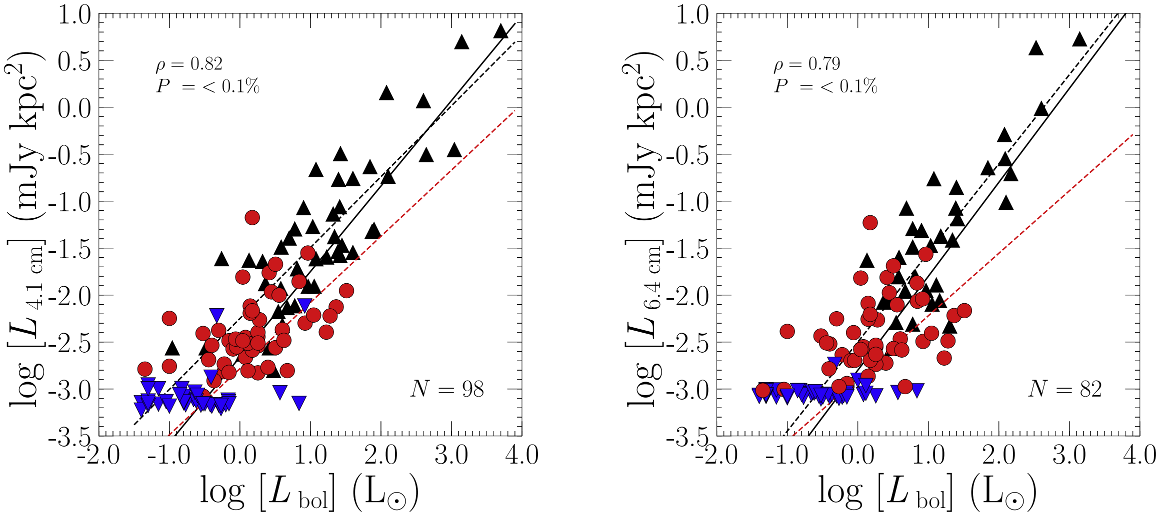

Figure 6. Radio luminosities plotted against bolometric luminosities of the sources. Red circles represent VANDAM sources, black triangles are the sources from Shirley et al. (2007), and blue triangles are upper limits of the VANDAM data. Red and black dashed lines show the linear fits to the VANDAM and Shirley et al. (2007) samples, respectively. The solid line represents the fit to the merged sample. Spearman's rank correlation coefficient and the probability of no correlation for the merged sample are shown in the left top corner.

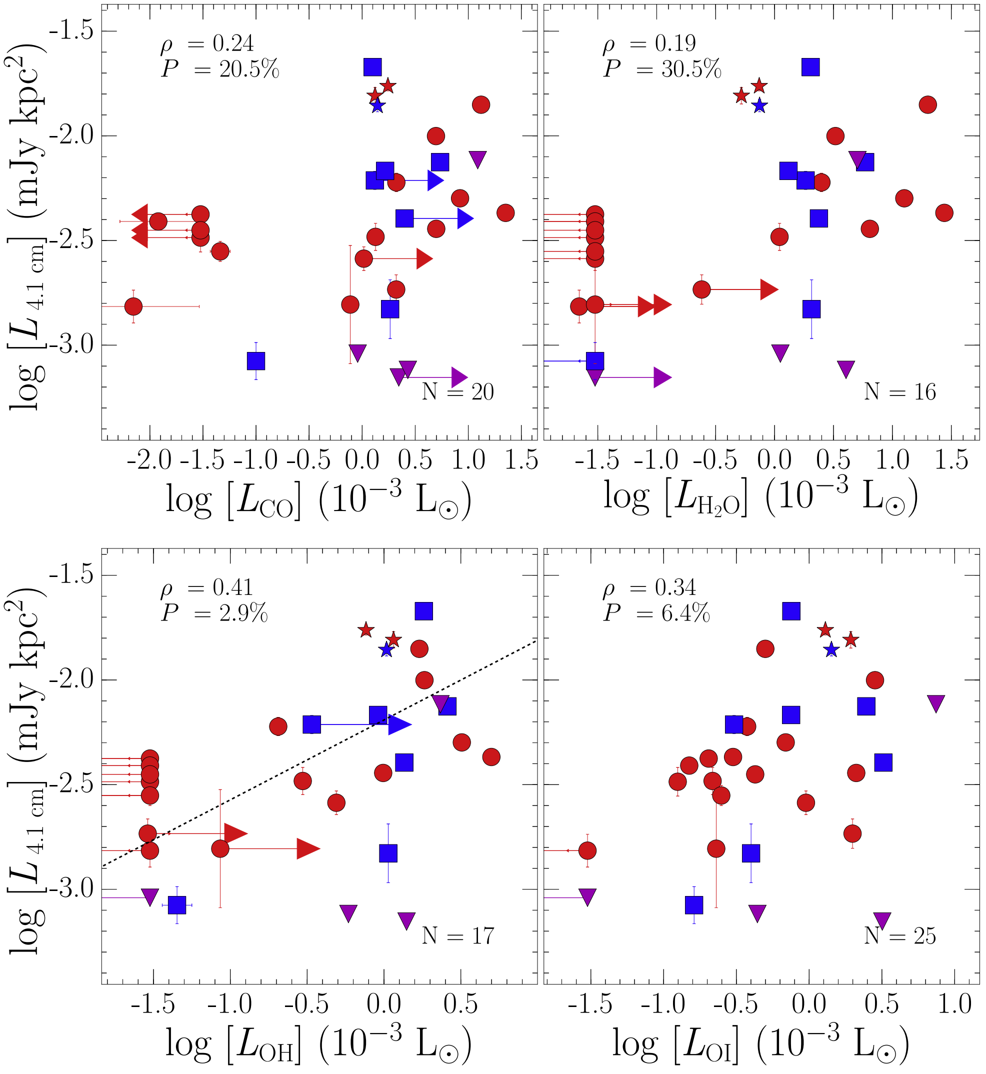

Figure 7. Luminosity at 4.1 cm, compared with CO (top left), H_2O (top right), [O I] (bottom left), and OH (bottom right) far-IR line luminosity. Upper limits for radio luminosities are plotted as magenta triangles, and lower or upper limits for *Herschel* line luminosities are indicated with arrows. Spearman's rank correlation coefficient and the probability of no correlation are shown in the right top corner (for a combined sample of Class 0 and Class I protostars).

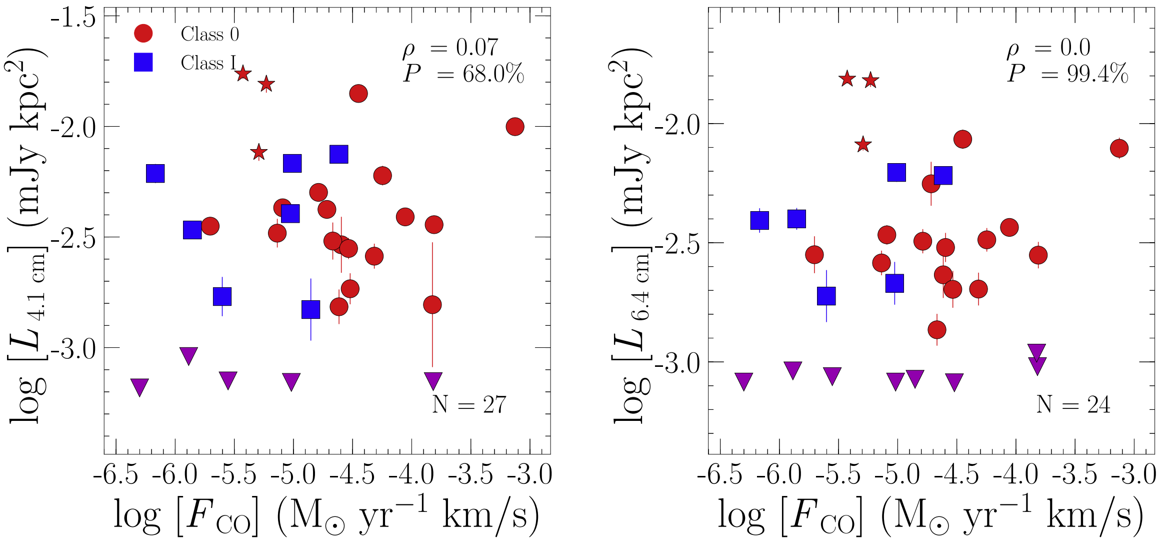

Figure 8. Radio luminosity at 4.1 cm (left) and 6.4 cm (right), compared with outflow force from various observations of CO. Upper limits are marked as magenta triangles. The Spearman's rank correlation coefficient and the probability of no correlation are shown in the top-right corner.

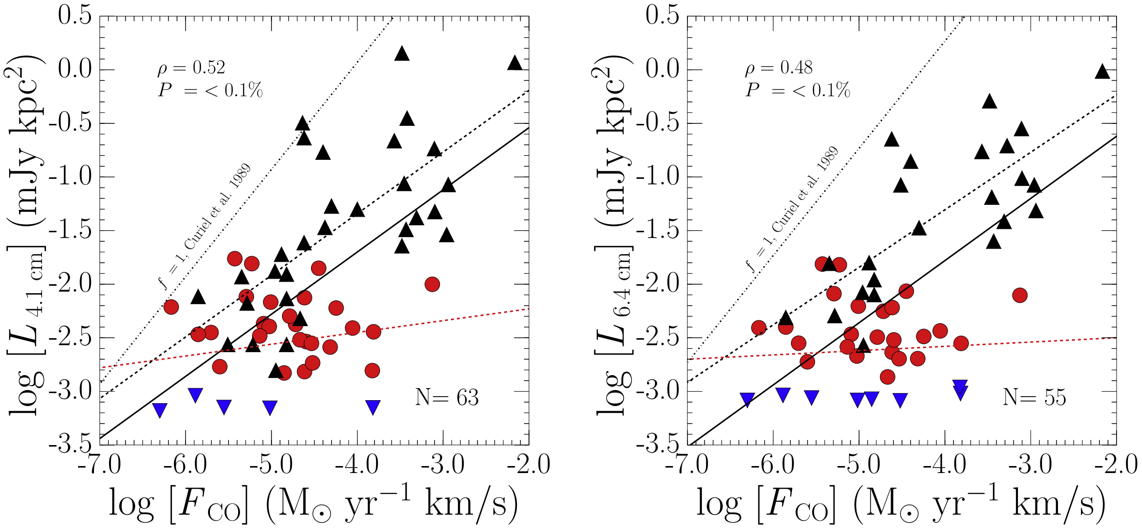

Figure 9. Radio luminosity at 4.1 cm (left) and 6.4 cm (right), plotted against outflow force from CO observations. Red and black dashed lines shows linear fits to the VANDAM and Shirley et al. (2007) samples, respectively. Solid lines represent fits to the merged sample. Black dashed–dotted line represents the expected C-band fluxes from the outflow force alone, assuming 100% efficiency, following Curiel et al. (1989). This line corresponds to the maximum C-band fluxes that can be produced from the CO outflows.

has $L_\odot = 3.7$, and we would expect them both to have a significant radio flux. It is possible that moderate long-term variability of the free–free emission is tightly connected to the episodic nature of the outflow/accretion events.

3.6. Updating Radio and Bolometric Luminosity Correlations

Radio emission from low-mass protostars cannot be explained by photoionization because the ionizing flux from the stars is too low (Rodríguez et al. 1989a; Cabrit & Bertout 1992; Anglada 1995). Instead, radio emission is attributed to shocks from the jets, which is supported by similar position angles between radio and molecular emission from the outflows (Anglada 1995, and references therein). Correlation of the radio flux and the bolometric luminosity also supports this hypothesis, as more luminous sources are expected to power more energetic outflows (Bontemps et al. 1996; Wu et al. 2004), therefore producing stronger ionizing shocks.

The most up-to-date and complete comparison of the radio flux and bolometric luminosity was provided by Shirley et al. (2007), who compiled data from various works (Anglada 1995; Anglada et al. 1998; Furuya et al. 2003; Eiroa et al. 2005). We are able to improve upon this characterization by using the VANDAM sample alone, as well as by combining it with data from Shirley et al. (2007). The VANDAM observations include lower luminosity protostars than those used in Shirley et al. (2007), hence we can extend the analysis of the bolometric and radio luminosity correlation.

We updated the distances and scaled the bolometric luminosities from Shirley et al. (2007), consisting of 45 sources at 3.6 cm and 34 at 6 cm. We merged the samples with the 4.1 cm and 6.4 cm sources from VANDAM, which resulted

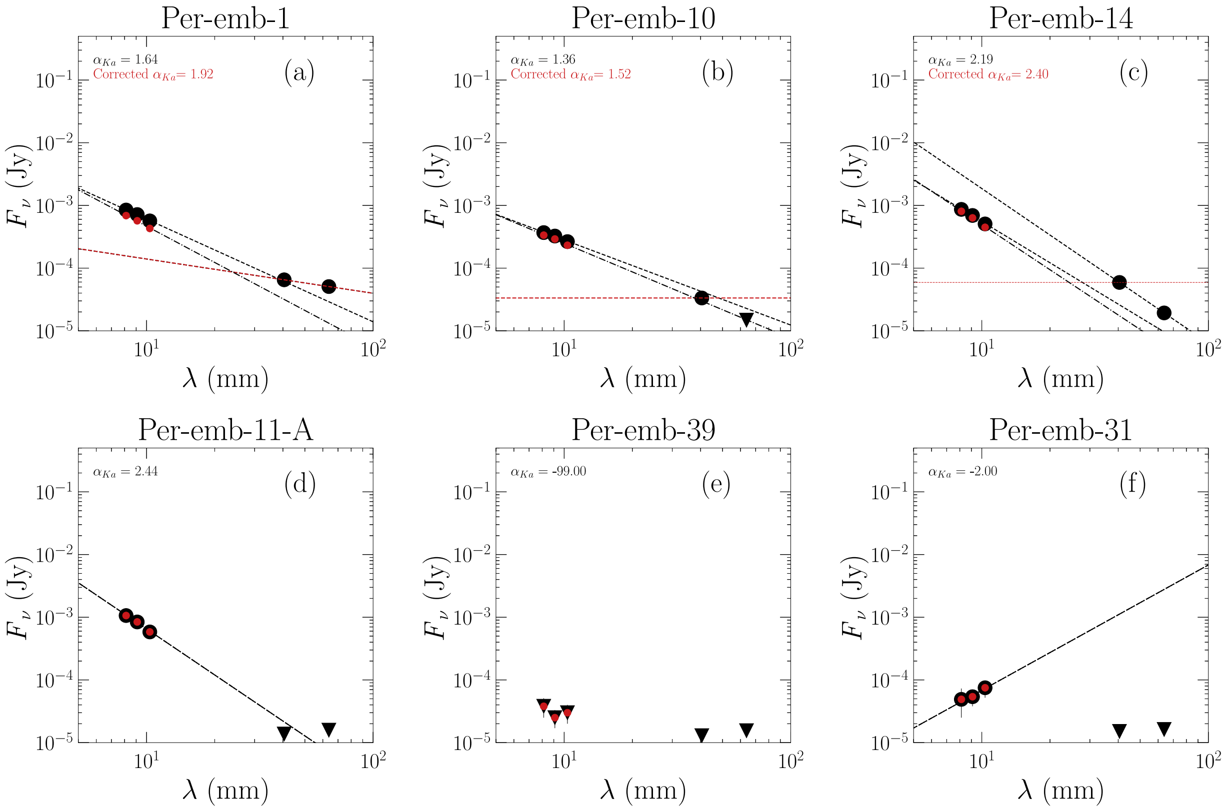

Figure 10. Example radio spectral energy distributions for our disk candidates. Each panel shows a different case in which we corrected the Ka-band data for free–free contamination. See text for details. Black bullets represent Ka-band and C-band flux densities, and triangles are upper limits. Red bullets mark the corrected Ka-band flux densities. Dotted lines are linear fits to the original data, and the red line represents the function from which the free–free contribution was estimated. Dashed–dotted line marks fit to the corrected Ka-band flux densities.

in a sample size of 98 and 82 for each wavelength respectively (detections only) In Figure 6 we compare the radio luminosities of the combined sample with the bolometric luminosities of the sources. We found stronger correlations for the merged VANDAM and Shirley sample, with the following linear fitting parameters:

$$\log(L_{4.1\text{ cm}}) = (-2.66 \pm 0.06) + (0.91 \pm 0.06)\log(L_{\text{bol}}),\ \rho = 0.82, \quad (8)$$

$$\log(L_{6.4\text{ cm}}) = (-2.80 \pm 0.07) + (1.00 \pm 0.07)\log(L_{\text{bol}}),\ \rho = 0.79. \quad (9)$$

The correlation for the merged sample appears robust and does not differ significantly from the correlation from Shirley et al. (2007). On the other hand, the linear fit parameters to the VANDAM data are different than for the merged sample, even considering the errors. The somewhat weak correlation in the VANDAM sample alone (see Equations (5) and (6)) results from the scatter within the sample, which can be explained by the variable nature of free–free emission. Moreover, a small contribution from the synchrotron emission can cause additional scatter (e.g., Tychoniec et al. 2018). Only by analyzing protostars spanning several orders of magnitude in luminosity can one derive a robust trend. For example, extended thermal jets can give a temporal rise to the flux. The Perseus results fill out the low-luminosity end of the overall distribution significantly better than before. Morata et al. (2015) analyzed a sample of proto-brown dwarfs, showing that they have radio fluxes higher than expected from their bolometric luminosities. This possibly suggests that correlation is flatter at the very low luminosities, but it is not evident with our data.

4. Correlations with Molecular Outflow Tracers

4.1. Far-infrared Line Emission

To characterize the relationship between radio emission and outflows, we use tracers of jets and outflows from observations of far-infrared molecular and atomic lines. The far-infrared regime is crucial to understand the cooling processes of gas in star-forming clouds; because it predominantly traces warm gas, emission at these wavelengths is expected to probe the currently shocked material (e.g., Nisini et al. 2002; Karska et al. 2013; Manoj et al. 2013, 2016). Thus, we expect to observe a correlation between far-infrared line luminosities and radio luminosity, which is likely tracing the shock-ionized gas.

We compare the VANDAM observations with data obtained by the Photoconductor Array Camera and Spectrometer (PACS) instrument (Poglitsch et al. 2010) onboard the *Herschel Space Observatory* (Pilbratt et al. 2010). The data come from two *Herschel* key programs: WISH (van Dishoeck et al. 2011) and DIGIT (Green et al. 2013), as well as from an open time program called WILL (Mottram et al. 2017). The PACS spectrometer is an integral field unit instrument with 25 spatial pixels (so-called spaxels) a field of view of ~50″; each spaxel is 9.″4 × 9.″4, corresponding to a physical resolution of about 2200 au at the distance to Perseus. The wavelength coverage of the PACS instrument (55–210 μm) allows one to study some of the key far-IR cooling agents of the shocked gas, e.g., CO, H_2O, OH, [O I]. Almost half of the sources analyzed

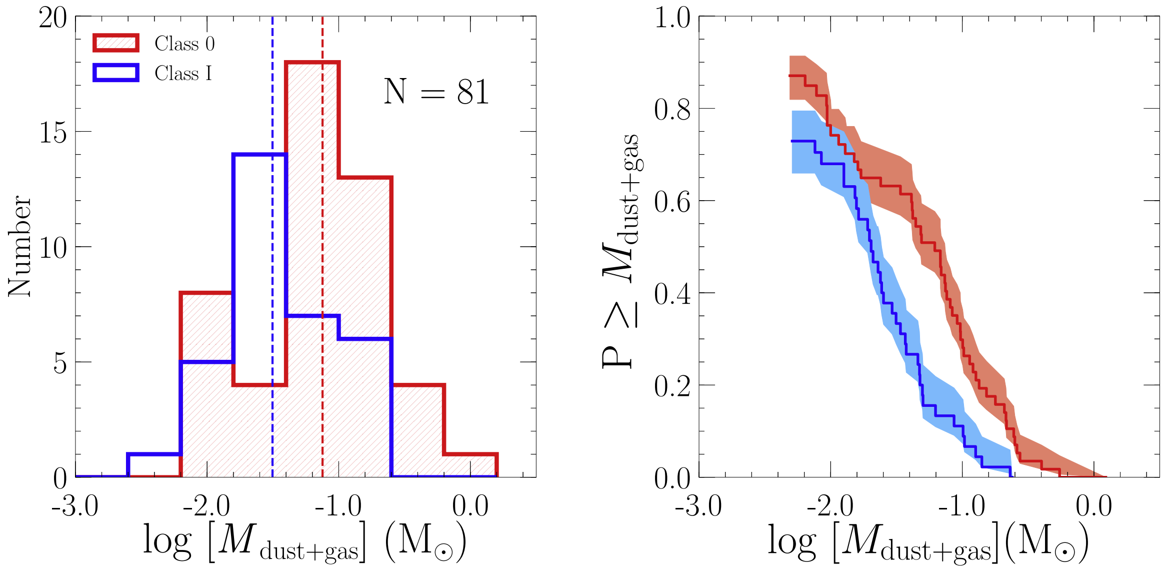

Figure 11. Left: Histogram of disk masses for each evolutionary class, obtained with a fixed temperature of dust, $T = 30$ K. Medians are shown with dashed lines, with respective colors. Median values are 0.075 $M_\odot$, 0.031 $M_\odot$, and 0.049 $M_\odot$ for Class 0, Class I, and the total sample, respectively. The statistical probability of Class 0 and Class I values of the disk mass being drawn from the same sample is 2.5%. Right: Cumulative distribution obtained via the K-M method, with 1σ errors shown.

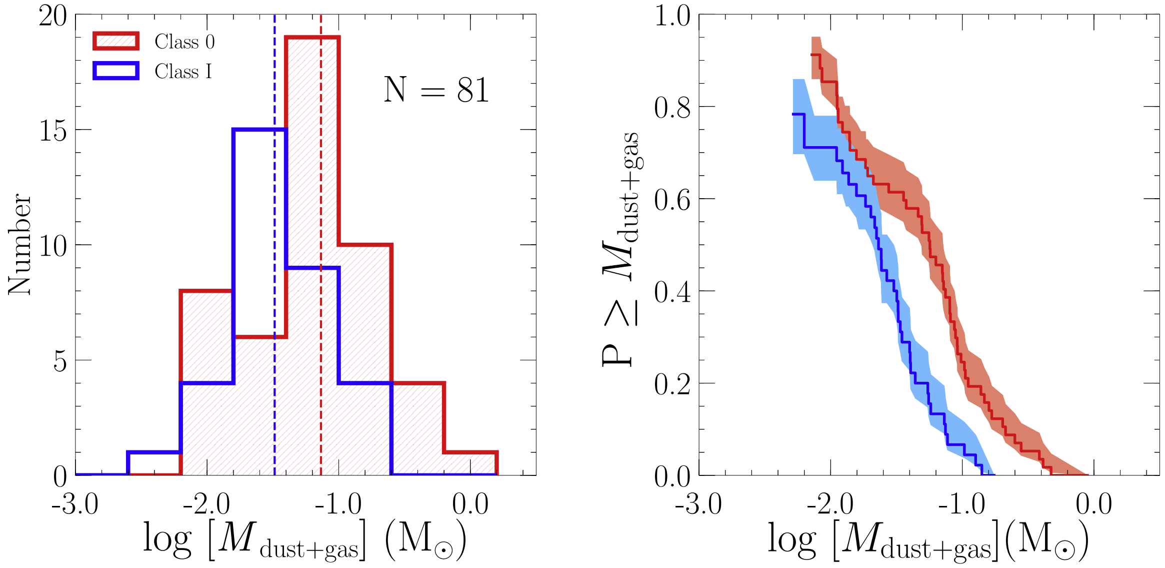

Figure 12. Similar to Figure 11, but for masses calculated using temperatures determined via $T_{\rm dust} = 30$ [K] × $(L_{\rm bol}/L\odot)^{1/4}$. Median values are 0.073 $M_\odot$, 0.033 $M_\odot$, and 0.055 $M_\odot$ for Class 0, Class I, and the total sample, respectively. We find a statistical probability of 1.5% that the Class 0 and Class I disk masses are drawn from the same sample.

within the sample show extended emission on scales of $\sim 10^4$ au, most commonly in [O I] (Karska et al. 2018). By contrast, VLA observations in the C-band primarily trace the emission from the inner 60 au. Comparing such different scales, as represented by radio and infrared observations, can be challenging. PACS observations trace the outflow history averaged over the past 10^2–10^3 years, while the VLA gives insight on timescales as short as a few years (e.g., Hull et al. 2016). We can then analyze how the nature of the outflow varies in time.

In Figure 7, we compare the radio luminosity at 4.1 cm with far-infrared luminosities of carbon monoxide (CO; $J_{\rm up} > 14$), water vapor (H_2O), oxygen [O I], and hydroxyl radical (OH). Similar figures with 6.4 cm luminosities are given in the Appendix A (Figure 17). The line luminosities are calculated by co-adding fluxes of the lines detected within the PACS wavelength range, and scaled with distance. We generally see very weak correlations or no evidence of correlations between radio luminosity and far-IR line luminosities. Nevertheless, we explore possible relations. The radio luminosity at 4.1 cm is weakly correlated with OH ($\rho = 0.41$, $P = 2.9\%$), with a stronger relation for Class I ($\rho = 0.64$, $P = 7.0\%$); and with [O I] ($\rho = 0.34$, $P = 6.4\%$), also showing a stronger dependence for Class I ($\rho = 0.52$, $P = 13.9\%$). For 6.4 cm, we can only see a weak correlation with OH ($\rho = 0.43$, $P = 2.1\%$) and [O I] ($\rho = 0.33$, $P = 8.0\%$). No correlation with $\rho > 0.4$ is

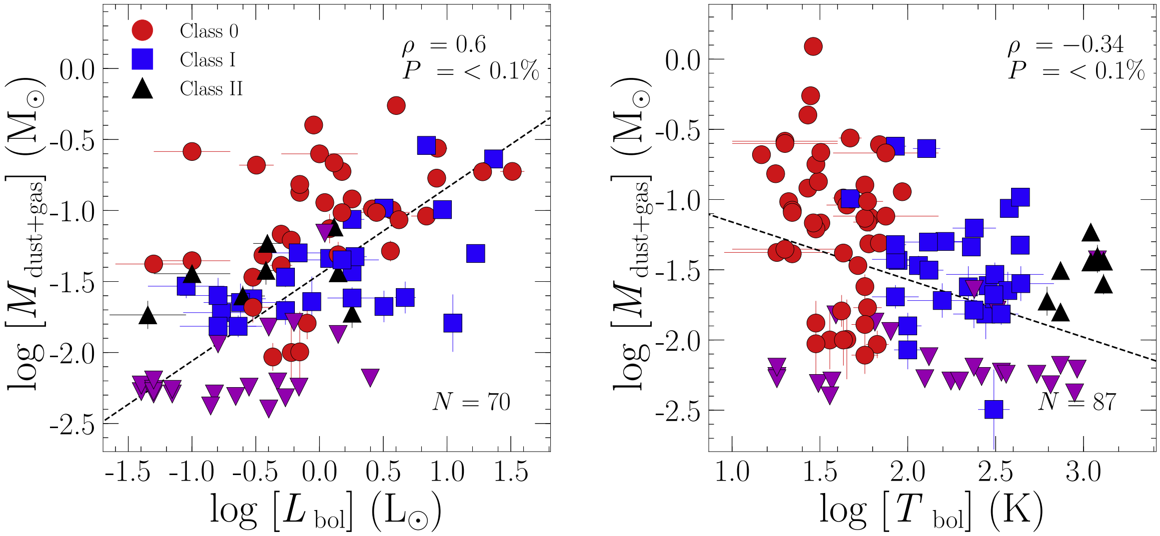

Figure 13. Disk mass compared with bolometric luminosity (left) and temperature (right). Upper limits are marked as magenta triangles. Spearman's rank correlation coefficient and the probability of no correlation are shown in the top-right corner. Dashed lines represents the EM algorithm fit to the data. Note that for bolometric luminosity, all multiple systems are combined together, while for bolometric temperature, each component is considered separately but with the same bolometric temperature, which results in different sample sizes.

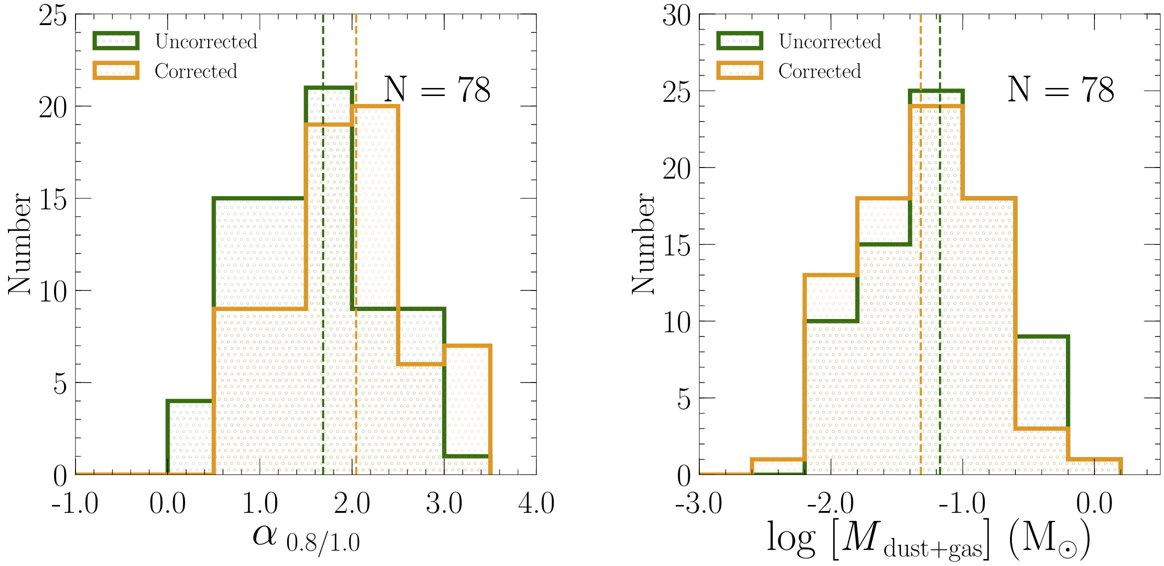

Figure 14. Histograms of Ka-band spectral index (left) and disk masses (right). Values not corrected for free–free contribution are shown in green, and the corrected ones are in yellow. Median values and log-rank probabilities of being drawn from the same sample are: 1.69 (uncorrected), 2.04 (corrected), and 0.6% for the spectral index distributions and 0.067 $M_\odot$ (uncorrected), 0.048 $M_\odot$ (corrected), and 37% for the disk masses.

observed for H_2O and CO line luminosities and radio luminosity. Correlation coefficients are summarized in Table 9.

The correlation between radio luminosity and the far-IR line luminosities may be linked to the correlations of those quantities with bolometric luminosity. Karska et al. (2013) show that the correlation of bolometric luminosity and far-IR lines are relatively weak (e.g., $r = 0.63$ for CO, $r = 0.53$ for [O I]); the extension over many orders of magnitude in source luminosity shows that the correlation is significant: $r > 0.92$ for CO (San José-García et al. 2013). Accordingly, on the scale of one cloud and with a narrow range of protostellar luminosities, many other phenomena, such as long-term variability of both radio and far-IR emission, can result in a large scatter.

Moderate correlation of radio luminosity with OH and [O I], juxtaposed with there being none for CO and H_2O, is interesting because it informs us about the physical origin of the emission. As discussed above, ionization that produces free–free emission is expected to come from shocks. Shocks are divided into two main types: J-type (jump) shocks, with a sharp jump in conditions between pre- and post-shock gas, and C-type (continuous) shocks where the change in temperature and density is less dramatic and occurs in a continuous manner (e.g., Draine et al. 1983; Hollenbach & McKee 1989; Neufeld & Dalgarno 1989).

Observations of OH and [O I] with *Herschel* are interpreted as arising in dissociative J-type shocks (van Kempen et al. 2010; Wampfler et al. 2013); up to 50% of CO emission may result from them as well, as well as less than 10% of the

Table 9
Correlations between Radio Flux with Line Luminosities

	CO	H_2O	OH	[O I]
4.1 cm				
Class 0	0.31	0.24	0.3	0.27
Class I	−0.19	−0.10	**0.64**	**0.52**
Class 0+I	0.24	0.19	**0.41**	0.34
6.4 cm				
Class 0	0.26	0.39	**0.43**	0.28
Class I	−0.18	−0.13	**0.52**	**0.54**
Class 0+I	0.16	0.28	**0.43**	0.33

Notes. Spearman's rank correlation coefficient (ρ) is listed. Bold font is for correlations $\rho > 0.4$. Significant correlations ($P < 5\%$) are underlined.

H_2O (Karska et al. 2014, Mottram et al. 2014). Comparing this to our results, we can infer that ionization that results in free–free emission is likely caused by J-type shocks. Alternatively, UV radiation from accretion shocks or a central protostar could explain some of the ionization. In that case, C-type shocks with significant UV contribution could cause the observed ionization.

The observed scatter and weak correlations between far-infrared line and radio continuum fluxes suggest that the ionized collimated jet close to the protostar is not directly related to the large-scale outflow. This is most likely related to the different physical scales compared here: far-IR lines observed with *Herschel* trace material excited in multiple ejection events, while the free–free emission probed by the VLA corresponds only to the most recent ejection. This could potentially be related to the accretion activity, but a correlation of radio emission and accretion bursts observed through infrared variability has not yet been established (Galván-Madrid et al. 2015).

4.2. Molecular Outflow Force

The discovery of correlations between the outflow force and the radio luminosity was crucial for linking the free–free emission from the protostars to the jet/outflow (e.g., Cabrit & Bertout 1992; Anglada 1995). We examine this relation for the protostars in Perseus, and add this subset to the sample of known protostellar radio sources with calculated outflow forces to solidify the correlation.

Outflow forces for Perseus protostars were taken from Mottram et al. (2017) and Hatchell et al. (2007), who used CO 3–2 James Clerk Maxwell Telescope observations to measure them. We present a comparison of the radio luminosity and outflow force in Figure 8. No significant correlation is observed in these comparisons. When using different observations for outflow forces, there is a risk of introducing additional error through different scales observed and different methods used. This issue can even introduce errors as great as an order of magnitude (van der Marel et al. 2013).

The lack of correlations of radio luminosity with outflow force/momentum differs with a number of other studies (e.g., Cabrit & Bertout 1992; Anglada 1995; Shirley et al. 2007), but all those works used a much wider range of protostellar luminosities to derive their correlations. It is important to keep in mind that the molecular outflow force is probed over much greater scales than radio emission, as noted above. This means that, while radio emission probes very recent ejection activity, the molecular outflow is averaged over much longer timescales.

To determine if the relation remains valid for a wider range of luminosities, we combine the VANDAM sample with data collected by Shirley et al. (2007), and plot them together in Figure 9. We updated distances to the sources included in the sample based on the most recent observations. We again find that the merged sample produces a correlation consistent with that of Shirley et al. (2007). As we noted for bolometric luminosity, the correlations are more clear when spanning more orders of magnitude in source luminosity. For the merged VANDAM and Shirley et al. (2007) sample, we fit linear functions with the EM algorithm:

$$\log(L_{4.1\ \mathrm{cm}}) = (0.62 \pm 0.45) + (0.58 \pm 0.09)\log(F_{\mathrm{CO}}),\ \rho = 0.52, \qquad (10)$$

$$\log(L_{6.4\ \mathrm{cm}}) = (0.54 \pm 0.49) + (0.58 \pm 0.11)\log(F_{\mathrm{CO}}),\ \rho = 0.48. \qquad (11)$$

The AMI Consortium et al. (2011, 2012) observed a weaker correlation between the 1.8 cm radio luminosity and the outflow force. Those authors checked whether the outflow force is sufficient to produce the observed radio flux by calculating the minimum outflow force needed for ionization based on an equation from Curiel et al. (1989):

$$\log L_\nu = 4.24 + \log[F_{\mathrm{out}} f (5\mathrm{GHz}/\nu)], \qquad (12)$$

where f is the ionization efficiency factor. The AMI Consortium et al. (2011) concluded that their sample had outflow forces that were too small to produce the observed radio flux, although the emission at 1.8 cm is likely to have contributions from dust. Here, we perform a similar analysis, and the minimum outflow force necessary to produce the observed C-band fluxes is plotted in Figure 9. The $f = 1$ case is shown by the dotted line. This case represents the upper limit of the expected C-band fluxes based on 100% outflow efficiency. Thus, we find that the outflow force can easily produce the observed C-band radio emission for both the VANDAM and the Shirley et al. (2007) samples. We note that the energy produced by the outflow is enough to generate the observed radio flux for all the sources, both from Perseus as well as the Shirley et al. (2007) sample.

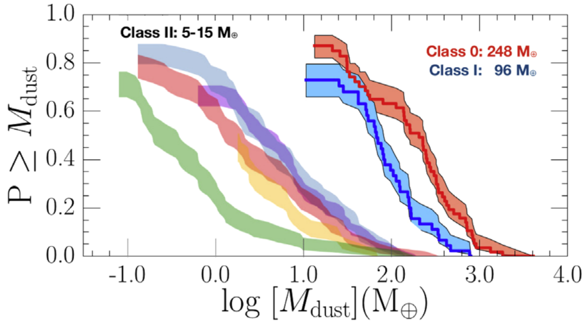

Figure 15. Cumulative distributions of disk masses in units of Earth mass. Class II distributions for four regions adapted from Ansdell et al. (2017). Different Class II star-forming regions are presented: Taurus (purple) (Andrews et al. 2013), Lupus (blue) (Ansdell et al. 2016), Chamaeleon I (red) (Pascucci et al. 2016), σ Orionis (yellow) (Ansdell et al. 2017), and Upper Sco (green) (Barenfeld et al. 2016).

5. Mass of the Protostellar Disks

5.1. Calculating the Mass

Two of the key questions in star formation are: (1) how early do disks form, and (2) how do they evolve and form planets? The properties of the youngest disks are still not defined very well. The unprecedented resolution of the VANDAM survey in the Ka-band (15 au) revealed several resolved disk candidates (Segura-Cox et al. 2016; Tobin et al. 2016), but follow-up kinematic data are needed to determine whether or not these structures are rotationally supported disks. The 9 mm Ka-band emission comes from $<0\farcs5$ scales and likely originates from a disk or compact inner envelope. The observations of the most point-like disk candidates are not consistent with envelope profiles (D. Segura-Cox et al. 2018, in preparation). Therefore, compact dust emission at 9 mm is likely tracing genuine disks. Calculating disk masses for an unbiased sample of very young protostars can provide important insights on the early stages of their evolution.

Disk mass can be estimated from the thermal dust emission, assuming the dust is optically thin. Ka-band observations are sensitive to radiation coming from cold and large grains in regions with high densities, which is most likely a direct progenitor of the disk, if not the disk itself. However, continuum emission in the Ka-band may also include a substantial thermal free–free component that can contribute to the emission even at wavelengths shorter than those measured by Ka-band (e.g., Choi 2009). Thus, to accurately estimate the disk mass, one must remove any free–free contamination from the Ka-band fluxes. For the VANDAM survey, we expect free–free emission to contribute significantly to the Ka-band emission for many sources because the median spectral indices for the sample between 8 mm and 1 cm are below 2 (Tobin et al. 2016). These values are lower than the typical spectral indices expected for dust, $\alpha = 2 + \beta$, where $\beta < 1$ is expected for dense disks (e.g., Draine 2006; Kwon et al. 2009; Testi et al. 2014). In this section, we assess the contribution of free–free emission on the Ka-band flux to subtract it and hence derive dust-only flux densities to calculate the masses of the embedded disks.

We fit a linear function to C-band logarithmic fluxes and then assumed that the value of this function at 9 mm is the free–free contribution to the total 9 mm flux. We use the Ka-band 9 mm flux density taken in the B configuration because the beam size is comparable to that of C-band observations taken in the A configuration. Figure 10 represents each of the cases in our sample. In case (a), both C-band fluxes are well-detected and we determined the free–free contribution in the Ka-bands from the C-band spectral index; in case (b), the source is detected at one C-band wavelength. To calculate the free–free contribution in case (b), we use the detected C-band flux and assume a free–free spectral index of 0. For case (c), we find a steeper slope for the C-band fluxes than the Ka-band fluxes, which can arise if the free–free emission is optically thick (Ghavamian & Hartigan 1998). Because we expect any free–free emission at the Ka-band to be optically thin, we use the 4.1 cm fluxes and an assumed spectral index of zero. In case (d), neither of the C-band fluxes are detected and we assume there is no free–free contamination at Ka-band for these sources. In case (e), we have non-detections in both the C- and Ka-bands, and we calculate upper limits of these disk masses assuming no free–free contamination. For case (f), we obtain a negative or flat spectral index in the Ka-band, which suggests the radio emission is not tracing dust even at 9 mm, and we provide an upper limit.

We consider the disk masses from these sources as upper limits and remove no free–free emission. Radio spectra for all of the sources are presented in Appendix C. For close binaries unresolved by the C-band (Per-emb-2, Per-emb-5, Per-emb-18), we assume they share a common disk and treat them as single protostars. This analysis is subject to many uncertainties. Free–free emission with a positive slope should turn over at wavelengths shorter than 4 cm, which would decrease the amount of the actual contribution. Ka- and C-band observations were taken at different epochs (eight months later) and variability of the free–free emission may have affected the analysis. The contribution of synchrotron emission may also have affected the spectral index. Finally, measured disk masses from Ka-band observations should be considered lower limits because the emissions at 8 mm and 1 cm are sensitive to the largest dust grains in the innermost parts of the disk (Segura-Cox et al. 2016). Nevertheless, we can still compare the disk properties across the VANDAM sample and identify trends with evolution, given that they are observed uniformly.

After correcting the Ka-band fluxes for free–free contamination, we calculate the mass of the disk, following the equation from Hildebrand (1983):

$$M = \frac{D^2 F_\lambda}{\kappa_\lambda B_\lambda(T_{\rm dust})}, \tag{13}$$

where D is the distance to the protostar ($\sim$235 pc), F_λ is the flux density from thermal dust emission, κ_λ is the dust opacity, and $B(T_{\rm dust})$ is the Planck blackbody function for an assumed dust temperature of 30 K, a typical temperature assumed for cold dust (Whitney et al. 2003). The value of κ_λ is based on the Ossenkopf & Henning (1994) dust opacity models:

$$\kappa_\lambda = 0.00899\left(\frac{1.3\ {\rm mm}}{\lambda}\right)^\beta\ {\rm cm^2\ g^{-1}}. \tag{14}$$

Here, values of $\lambda = 9$ mm and $\beta = 1$ (Andrews et al. 2009), which are typical for disks, assuming a gas-to-dust mass ratio

Table 10
Protostellar Disk Masses

Name	F_ν (9 mm) (mJy)	F_ν (corrected) (mJy)	$F_{\rm dust}/F_{9\ \rm mm}$ %	$M_{\rm gas+dust}$ (9 mm) ($M_\odot$)	$M_{\rm gas+dust}$ (corrected) ($M_\odot$)	Flag[a]
Per-emb-1	0.72	0.57	79	0.152 ± 0.004	0.121 ± 0.004	a
Per-emb-2	2.04	1.89	92	0.432 ± 0.019	0.400 ± 0.019	a
Per-emb-2-A	…	…	…	…	…	…
Per-emb-2-B	…	…	…	…	…	…
Per-emb-3	0.35	0.32	91	0.074 ± 0.004	0.068 ± 0.004	a
Per-emb-4	<0.02	<0.02	…	<0.005 ± 0.002	<0.005 ± 0.002	e
Per-emb-5	1.05	1.02	97	0.223 ± 0.007	0.217 ± 0.007	b
Per-emb-5-A	…	…	…	…	…	…
Per-emb-5-B	…	…	…	…	…	…
Per-emb-6	0.25	0.16	64	0.052 ± 0.004	0.034 ± 0.004	a
Per-emb-7	<0.02	<0.02	…	<0.005 ± 0.002	<0.005 ± 0.002	e
Per-emb-8	0.94	0.48	51	0.200 ± 0.006	0.103 ± 0.006	a
Per-emb-9	0.05	0.05	86	0.011 ± 0.005	0.010 ± 0.005	a
Per-emb-10	0.33	0.29	89	0.069 ± 0.004	0.062 ± 0.004	b
Per-emb-11	0.99	0.89	89	0.211 ± 0.016	0.188 ± 0.016	a
Per-emb-11-A	0.84	0.84	100	0.178 ± 0.006	0.178 ± 0.006	d
Per-emb-11-B	0.09	0.04	48	0.019 ± 0.005	0.009 ± 0.005	c
Per-emb-11-C	0.06	0.06	100	0.013 ± 0.005	0.013 ± 0.005	d
Per-emb-12	7.98	6.69	83	1.693 ± 0.021	1.419 ± 0.021	a
Per-emb-12-A	7.28	5.80	79	1.544 ± 0.014	1.231 ± 0.014	a
Per-emb-12-B	0.70	0.32	45	0.149 ± 0.007	0.068 ± 0.007	a
Per-emb-13	2.75	2.59	94	0.583 ± 0.012	0.548 ± 0.012	a
Per-emb-14	0.69	0.63	91	0.147 ± 0.006	0.134 ± 0.006	c
Per-emb-15	0.07	0.02	28	0.014 ± 0.005	0.004 ± 0.005	f
Per-emb-16	0.07	0.07	100	0.015 ± 0.006	0.015 ± 0.006	f
Per-emb-17	0.54	0.41	75	0.114 ± 0.006	0.086 ± 0.006	a
Per-emb-17-A	0.46	0.33	71	0.097 ± 0.004	0.069 ± 0.004	a
Per-emb-17-B	0.08	0.08	100	0.017 ± 0.002	0.017 ± 0.002	d
Per-emb-18	0.67	0.46	68	0.141 ± 0.007	0.097 ± 0.007	a
Per-emb-18-A	…	…	…	…	…	…
Per-emb-18-B	…	…	…	…	…	…
Per-emb-19	0.24	0.23	95	0.051 ± 0.005	0.048 ± 0.005	a
Per-emb-20	0.17	0.06	36	0.037 ± 0.005	0.013 ± 0.005	f
Per-emb-21	0.43	0.43	100	0.091 ± 0.005	0.091 ± 0.005	d
Per-emb-22	0.64	0.24	38	0.135 ± 0.009	0.052 ± 0.009	a
Per-emb-22-A	0.49	0.20	40	0.103 ± 0.004	0.042 ± 0.004	a
Per-emb-22-B	0.15	0.05	31	0.032 ± 0.004	0.010 ± 0.004	a
Per-emb-23	0.12	0.08	61	0.026 ± 0.004	0.016 ± 0.004	c
Per-emb-24	0.07	0.04	66	0.014 ± 0.002	0.009 ± 0.002	b
Per-emb-25	0.49	0.35	72	0.103 ± 0.018	0.074 ± 0.018	a
Per-emb-26	1.69	1.29	76	0.359 ± 0.005	0.274 ± 0.005	a
Per-emb-27	1.69	0.88	52	0.359 ± 0.008	0.187 ± 0.008	a
Per-emb-27-A	1.44	1.16	80	0.305 ± 0.004	0.246 ± 0.004	a
Per-emb-27-B	0.26	0.23	90	0.054 ± 0.004	0.049 ± 0.004	b
Per-emb-28	0.07	0.05	63	0.016 ± 0.007	0.010 ± 0.007	c
Per-emb-29	0.47	0.47	100	0.101 ± 0.004	0.101 ± 0.004	d
Per-emb-30	0.84	0.54	63	0.178 ± 0.004	0.114 ± 0.004	a
Per-emb-31	0.05	0.05	100	0.011 ± 0.005	0.011 ± 0.005	f
Per-emb-32	0.10	0.10	100	0.021 ± 0.005	0.021 ± 0.005	d
Per-emb-32-A	0.04	0.04	100	0.008 ± 0.002	0.008 ± 0.002	d
Per-emb-32-B	0.06	0.06	100	0.013 ± 0.003	0.013 ± 0.003	d
Per-emb-33	0.88	0.80	91	0.186 ± 0.012	0.169 ± 0.012	a
Per-emb-33-A	0.62	0.60	95	0.132 ± 0.007	0.127 ± 0.007	b
Per-emb-33-B	0.35	0.35	100	0.074 ± 0.007	0.074 ± 0.007	d
Per-emb-33-C	0.25	0.11	45	0.053 ± 0.005	0.024 ± 0.005	a
Per-emb-34	0.20	0.17	86	0.043 ± 0.004	0.037 ± 0.004	b
Per-emb-35	0.56	0.08	13	0.118 ± 0.007	0.016 ± 0.007	a
Per-emb-35-A	0.35	0.10	27	0.074 ± 0.004	0.020 ± 0.004	a
Per-emb-35-B	0.21	0.18	85	0.044 ± 0.004	0.037 ± 0.004	c
Per-emb-36	1.64	1.36	82	0.348 ± 0.008	0.287 ± 0.008	a
Per-emb-36-A	1.42	1.13	79	0.300 ± 0.005	0.240 ± 0.005	a
Per-emb-36-B	0.23	0.23	100	0.048 ± 0.003	0.048 ± 0.003	d

Table 10
(Continued)

Name	F_ν (9 mm) (mJy)	F_ν (corrected) (mJy)	$F_{\rm dust}/F_{9\ \rm mm}$ %	$M_{\rm gas+dust}$ (9 mm) ($M_\odot$)	$M_{\rm gas+dust}$ (corrected) ($M_\odot$)	Flag[a]
Per-emb-37	0.19	0.19	100	0.041 ± 0.004	0.041 ± 0.004	d
Per-emb-38	0.16	0.16	100	0.034 ± 0.005	0.034 ± 0.005	d
Per-emb-39	<0.03	<0.03	⋯	<0.005 ± 0.002	<0.005 ± 0.002	e
Per-emb-40	0.38	0.21	56	0.080 ± 0.006	0.045 ± 0.006	a
Per-emb-40-A	0.34	0.15	43	0.071 ± 0.003	0.031 ± 0.003	a
Per-emb-40-B	0.04	0.04	91	0.008 ± 0.003	0.008 ± 0.003	f
Per-emb-41	0.09	0.09	100	0.019 ± 0.005	0.019 ± 0.005	d
Per-emb-42	0.24	0.24	100	0.050 ± 0.005	0.050 ± 0.005	d
Per-emb-43	<0.02	<0.02	⋯	<0.005 ± 0.002	<0.005 ± 0.002	e
Per-emb-44	1.89	0.89	46	0.402 ± 0.012	0.188 ± 0.012	a
Per-emb-44-A	1.43	1.01	70	0.302 ± 0.004	0.215 ± 0.004	a
Per-emb-44-B	0.47	0.36	76	0.099 ± 0.007	0.076 ± 0.007	c
Per-emb-45	<0.02	<0.02	⋯	<0.005 ± 0.002	<0.005 ± 0.002	e
Per-emb-46	0.13	0.11	88	0.027 ± 0.008	0.024 ± 0.008	b
Per-emb-47	0.26	0.22	84	0.054 ± 0.006	0.046 ± 0.006	b
Per-emb-48	0.14	0.11	74	0.030 ± 0.009	0.023 ± 0.009	a
Per-emb-48-A	0.08	0.08	100	0.016 ± 0.005	0.016 ± 0.005	d
Per-emb-48-B	0.07	0.03	45	0.014 ± 0.004	0.006 ± 0.004	f
Per-emb-49	0.45	0.33	73	0.094 ± 0.008	0.069 ± 0.008	f
Per-emb-49-A	0.33	0.30	89	0.070 ± 0.004	0.063 ± 0.004	c
Per-emb-49-B	0.12	0.11	93	0.025 ± 0.004	0.023 ± 0.004	f
Per-emb-50	1.36	1.09	79	0.289 ± 0.007	0.231 ± 0.007	a
Per-emb-51	<0.03	<0.03	⋯	<0.005 ± 0.003	<0.005 ± 0.003	e
Per-emb-52	0.07	0.07	100	0.015 ± 0.006	0.015 ± 0.006	d
Per-emb-53	0.22	0.12	52	0.046 ± 0.006	0.024 ± 0.006	a
Per-emb-54	0.31	0.23	76	0.065 ± 0.005	0.050 ± 0.005	c
Per-emb-55	0.17	0.11	67	0.036 ± 0.004	0.024 ± 0.004	c
Per-emb-55-A	0.10	0.10	100	0.021 ± 0.002	0.021 ± 0.002	d
Per-emb-55-B	0.07	0.02	21	0.015 ± 0.002	0.003 ± 0.002	c
Per-emb-56	0.09	0.09	100	0.020 ± 0.004	0.020 ± 0.004	d
Per-emb-57	0.16	0.14	88	0.033 ± 0.006	0.029 ± 0.006	b
Per-emb-58	0.08	0.08	100	0.016 ± 0.005	0.016 ± 0.005	f
Per-emb-59	<0.03	<0.03	⋯	<0.006 ± 0.003	<0.006 ± 0.003	e
Per-emb-60	<0.03	<0.03	⋯	<0.006 ± 0.003	<0.006 ± 0.003	e
Per-emb-61	0.11	0.11	100	0.022 ± 0.007	0.022 ± 0.007	d
Per-emb-62	0.61	0.41	66	0.130 ± 0.006	0.087 ± 0.006	a
Per-emb-63	0.32	0.22	69	0.069 ± 0.005	0.047 ± 0.005	a
Per-emb-64	0.93	0.49	52	0.197 ± 0.006	0.104 ± 0.006	a
Per-emb-65	0.12	0.12	100	0.025 ± 0.007	0.025 ± 0.007	d
Per-emb-66	<0.03	<0.03	⋯	<0.006 ± 0.003	<0.006 ± 0.003	e
Per-bolo-58	<0.03	<0.03	⋯	<0.005 ± 0.003	<0.005 ± 0.003	e
Per-bolo-45	<0.03	<0.03	⋯	<0.005 ± 0.002	<0.005 ± 0.002	e
L1451-MMS	0.20	0.20	100	0.042 ± 0.004	0.042 ± 0.004	d
L1448IRS2E	<0.03	<0.03	⋯	<0.006 ± 0.003	<0.006 ± 0.003	e
B1-bN	0.98	0.98	100	0.209 ± 0.007	0.209 ± 0.007	d
B1-bS	0.72	0.72	100	0.153 ± 0.011	0.153 ± 0.011	d
L1448IRS1	0.84	0.67	79	0.178 ± 0.010	0.142 ± 0.010	a
L1448IRS1-A	0.77	0.60	77	0.162 ± 0.005	0.126 ± 0.005	a
L1448IRS1-B	0.07	0.07	100	0.016 ± 0.004	0.016 ± 0.004	d
L1448NW	0.99	0.23	23	0.210 ± 0.010	0.049 ± 0.010	a
L1448NW-A	0.59	0.40	66	0.126 ± 0.005	0.084 ± 0.005	a
L1448NW-B	0.40	0.38	96	0.084 ± 0.005	0.081 ± 0.005	b
L1448IRS3A	1.04	0.48	46	0.220 ± 0.006	0.101 ± 0.006	a
SVS13C	2.28	0.46	19	0.483 ± 0.007	0.097 ± 0.007	a
SVS13B	1.24	1.18	95	0.262 ± 0.007	0.251 ± 0.007	b
IRAS03363+3207	0.71	0.66	93	0.151 ± 0.005	0.141 ± 0.005	c
EDJ2009-263	0.07	0.07	100	0.015 ± 0.003	0.015 ± 0.003	d
EDJ2009-285	<0.03	<0.03	⋯	<0.006 ± 0.003	<0.006 ± 0.003	e
IRAS03295+3050	0.12	0.12	100	0.025 ± 0.004	0.025 ± 0.004	d
L1455IRS2	0.05	0.03	58	0.011 ± 0.004	0.007 ± 0.004	f
EDJ2009-385	0.18	0.18	100	0.038 ± 0.009	0.038 ± 0.009	d
EDJ2009-366	0.14	0.09	63	0.030 ± 0.004	0.019 ± 0.004	c

Table 10
(Continued)

Name	F_ν (9 mm) (mJy)	F_ν (corrected) (mJy)	$F_{\rm dust}/F_{\rm 9\ mm}$ %	$M_{\rm gas+dust}$ (9 mm) ($M_\odot$)	$M_{\rm gas+dust}$ (corrected) ($M_\odot$)	Flag[a]
EDJ2009-269	0.42	0.36	86	0.088 ± 0.012	0.076 ± 0.012	b
EDJ2009-269-A	0.21	0.18	83	0.045 ± 0.005	0.037 ± 0.005	f
EDJ2009-269-B	0.20	0.19	90	0.043 ± 0.006	0.039 ± 0.006	b
EDJ2009-183	0.15	0.10	64	0.033 ± 0.005	0.021 ± 0.005	a
EDJ2009-183-A	0.11	0.06	52	0.024 ± 0.003	0.013 ± 0.003	a
EDJ2009-183-B	0.04	0.04	100	0.009 ± 0.003	0.009 ± 0.003	d
EDJ2009-164	<0.02	<0.02	⋯	<0.004 ± 0.002	<0.004 ± 0.002	e
EDJ2009-156	0.25	0.09	34	0.053 ± 0.004	0.018 ± 0.004	a
EDJ2009-156-A	0.15	0.15	100	0.031 ± 0.002	0.031 ± 0.002	d
EDJ2009-156-B	0.10	0.07	71	0.022 ± 0.002	0.016 ± 0.002	c
EDJ2009-172	0.31	0.28	90	0.065 ± 0.006	0.059 ± 0.006	b
EDJ2009-173	0.20	0.17	84	0.043 ± 0.003	0.036 ± 0.003	b
SVS13A2	0.31	0.21	67	0.066 ± 0.006	0.044 ± 0.006	c
IRAS4B’	1.23	1.23	100	0.260 ± 0.013	0.260 ± 0.013	d
EDJ2009-233	0.36	0.17	47	0.076 ± 0.005	0.036 ± 0.005	a
EDJ2009-235	0.04	0.02	54	0.009 ± 0.003	0.005 ± 0.003	f
SVS3	0.24	0.00	0	0.052 ± 0.010	0.000 ± 0.010	f
SVS3-A	0.21	0.13	58	0.046 ± 0.007	0.027 ± 0.007	f
SVS3-B	<0.03	<0.03	⋯	<0.006 ± 0.003	<0.000 ± 0.003	f

Notes.

[a] Flags: a—regular fit; b—one of the C-band channels with non-detection; c—excess of the free–free emission; d—non-detection in both C-band channels; e—non-detection in both Ka- and C-band; f—flat or negative spectral index in Ka-band; Flags d, e, and f, were treated as upper limits in the analysis.

(This table is available in machine-readable form.)

of 100:1, gives a value: $\kappa_{\rm 9\ mm} = 0.00128\,{\rm cm}^2\,{\rm g}^{-1}$. Table 10 lists the calculated disk masses for the VANDAM sources.

The calculated masses are consistent with those obtained by Segura-Cox et al. (2016) for seven sources from the VANDAM sample. Segura-Cox et al. (2016) used the same Ka-band data to model the disk structure and removed free–free contamination using a point-source model of free–free emission. For Per-emb-8, however, Segura-Cox et al. (2016) modeled a higher disk mass of 0.12–0.24 $M_\odot$, where we obtained a value of $0.097 \pm 0.006\,M_\odot$ with our free–free correction. This source exhibits particularly strong, extended free–free emission with a resolved radio jet (Tychoniec et al. 2018), such that the free–free emission contributes roughly 43% of the Ka-band continuum. For Per-emb-12-A (IRAS 4A), Cox et al. (2015) obtained 2.3 $M_\odot$ from uncorrected VANDAM data (they used $\beta = 1.3$, which further increases the estimated mass). With our corrected Ka-band fluxes, we find a mass of 1.2 $M_\odot$, which is still remarkably large, but more consistent with the typical masses ($<1\,M_\odot$) of the low-mass protostellar disks (e.g., Jørgensen et al. 2009; Enoch et al. 2011).

Figure 11 shows the distribution of mass for each evolutionary stage and the cumulative distribution obtained with the Kaplan–Meier estimator, for Class 0 and Class I only. We notice a clear decrease in mass between Class 0 and Class I, with median values of 0.075 $M_\odot$ and 0.031 $M_\odot$, respectively. The log-rank test was used to ascertain the probability of drawing Class 0 and Class I data sets from the same sample. We find a probability of only 2.5%, indicating that Class 0 and Class I mass distributions are statistically different. The sample size of Class II sources is too small to draw statistical conclusions (the median mass is 0.036 $M_\odot$). The median mass for the combined Class 0 and I sample is 0.049 $M_\odot$.

As a constant dust temperature for all the sources is a very simplistic assumption, we also tried to account for the source luminosity by scaling the assumed dust temperature with the bolometric luminosity: $T_{\rm dust} = 30\quad[{\rm K}] \times (L_{\rm bol}/L_\odot)^{1/4}$. Figure 12 shows the mass distribution in this case. Obtained values are still consistent with an evolutionary decrease of masses, with a log-rank test indicating a 1.5% chance of Class 0 and Class I distributions being drawn from the same sample. Taking into account the inescapable limitations, it is clear that disk mass does not grow between Class 0 and Class I, which suggests that disks form early during the star formation process and have the highest masses at an early age.

Figure 13 shows disk masses compared with bolometric temperature and luminosity. We observe a weak correlation ($\rho = 0.60$, $P < 0.01\%$) between the disk mass and the bolometric luminosity (Figure 13). As the latter is used as a proxy of protostellar mass (with many caveats), this result is reminiscent of the correlation between the disk mass and stellar mass observed for the more evolved disks (Natta et al. 2000; Williams & Cieza 2011; Ansdell et al. 2017). A noticeable decrease of disk mass with bolometric temperature can be seen, hinting at a dependency between disk mass and evolution ($\rho = -0.34$, $P < 0.1\%$), as already apparent from the distributions of disk masses for Class 0 and Class I discussed above.

Finally, we assess the impact of the free–free emission on the calculated disk masses and spectral indices in the Ka-band.

Figure 14 presents the distributions of masses and spectral indices with and without correction. When the correction is not applied, the spectral indices between 8 mm and 1 cm are flatter (median spectral index drops from 2.04 to 1.69) and the disk masses increase (from $0.048\,M_{\odot}$ to $0.067\,M_{\odot}$). The spectral index change is statistically significant (log-rank: 0.6%), while mass change is less robust (log-rank: 37%). Thus, the free–free contribution can, to some extent, explain the shallower-than-expected spectral indices observed in the Ka-band Tobin et al. (2016), and it seems that the masses of the disks are slightly overestimated without correction for the free–free contribution.

5.2. Evolutionary Trend in Dust Mass

The advent of the Atacama Large Millimeter/submillimeter Array (ALMA) has made it possible to study the gas and dust content of protoplanetary disks with unprecedented sensitivity. Surveys of Class II disks at different mean ages show that the disk dust mass consistently decreases with age within the Class II population (Ansdell et al. 2016, 2017; Barenfeld et al. 2016). The other outstanding conclusion from those pioneering surveys was that there is not enough dust content to form gas giant planet cores even in the youngest Class II disks (e.g., Ansdell et al. 2016). Studying even younger embedded disks could answer important questions: does the decrease of the dust mass with age happen as early as from Class 0 to Class I, i.e., in the first 0.5 Myr; is the dust mass in the embedded disks sufficient to allow the formation of the cores of gas giants?

Tobin et al. (2015b) find a median mass of $\sim 0.05\,M_{\odot}$ for 9 Class 0 protostars in Perseus. They note that the value is about an order of magnitude higher than the disk masses for Class II objects by Andrews & Williams (2005), and about 5 times larger than the median mass for Class I disks from Jørgensen et al. (2009). With the much greater sample of VANDAM sources, we confirm a decrease in disk mass with evolutionary class. However, Jørgensen et al. (2009) pointed out that some of the assumptions used to derive mass, such as constant opacity and temperature, could confuse the real picture. They considered models provided by Visser et al. (2009) that suggest that dust temperature decreases from Class 0 to Class I due to the systematic decrease in the luminosity between Class 0 and Class I. After applying factors to simulate the evolutionary effects, Jørgensen et al. (2009) find that the apparent trend between Class 0 and Class I masses becomes insignificant. Fischer et al. (2017) recently showed a decrease in bolometric luminosity for a large sample of protostars in Orion, which might occur due to the decrease of the envelope emission, while protostellar luminosity still increases. Dunham et al. (2014) suggest using different temperatures for Class 0 and Class I disks based on pure hydrodynamical simulations. However, our attempt to take into account the possible difference in luminosity between the two evolutionary classes still yields a statistically significant difference between disk masses of Class 0 and Class I protostars.

Figure 15 shows a comparison between VANDAM results and the Class II surveys presented in Ansdell et al. (2017). The observed decrease of mass between Class 0 and Class I protostars, and further to Class II, shows that a significant fraction of dust is dispersed or incorporated into larger bodies. If the latter scenario is considered, the amount of dust-only mass available for planet formation ($248\,M_{\oplus}$[15]) is enough to form solid cores for the giant planets. The further decrease in mass to $96\,M_{\oplus}$ in Class I shows that significant grain growth could occur at those early stages (Miotello et al. 2014; Sheehan & Eisner 2017). Recent ALMA surveys of Class II disks yield masses of 5–15 $M_{\oplus}$ for different star-forming regions (e.g., Ansdell et al. 2016; Barenfeld et al. 2016; Pascucci et al. 2016). It shows that, if the core accretion is considered as a planet formation route, it may begin very early in Class 0, and the physical conditions at those early stages should be considered in planet formation models.

6. Conclusions

We observed all known (84) Class 0 and I protostellar systems in the Perseus molecular cloud with the VLA at C-band (4.1 and 6.4 cm). The major conclusions of this work are as follows:

1. The detection rate is 61% for Class 0 and 53% for Class I protostars. Neither flux densities nor spectral indices show a significant difference between the two evolutionary stages, indicating that strength and nature of the emission is independent of evolution, at least through the protostellar phase.
2. The spectral index from 4.1 to 6.4 cm for the detected protostars has a median value of $\alpha_{\rm median} = 0.51$, consistent with moderately optically thick thermal free–free emission. The C-band spectral index shows no correlation with protostellar bolometric luminosity and temperature. Sources with resolved thermal jets have typically lower spectral indices consistent with optically thin emission from the jet, in addition to being the brightest free–free objects.
3. We detect all components in half of the close (<500 au) binary systems present in a sample. Protostellar companions within the same system can have very different flux densities and spectral indices. There are also examples of systems where a brighter Ka-band component appears fainter in the C-band.
4. We greatly extended the group of the protostars characterized at centimeter wavelengths, especially at the low-luminosity end. However, the radio luminosity from the protostars only in Perseus is weakly correlated with bolometric luminosity; by combining these data with previous observations spanning a larger range of $L_{\rm bol}$, we obtained a good correlation. The linear fit for the Perseus-only sample shows a flatter relation between radio and bolometric luminosity than for the merged sample.
5. We investigate correlations between the radio luminosity and molecular and atomic far-IR line luminosity from *Herschel*. We obtain moderate correlations for OH and [O I]. Comparing this result with shock models, we conclude that the ionization observed as free–free emission is predominantly a result of J-type shocks. Extending this analysis to a sample of high-mass protostars could provide further insight.
6. We update the correlation between the radio luminosity and outflow force from protostars. Within the range of luminosities in Perseus, there is no correlation, but inclusion of a greater range of radio luminosities and outflow forces results in a moderate correlation, consistent with previous studies. We find that the molecular outflow forces are sufficient to produce the obtained radio fluxes in our sample. This shows that, while shock ionization generally is a viable explanation of free–free emission, molecular outflows have different characteristics than a thermal radio jet, likely due to the different scales probed.

---

[15] Values converted to Earth masses and without multiplying by 100 to exclude gas mass.

7. We calculate the disk masses around protostars, using Ka-band (9 mm) flux densities corrected for free–free contribution from the C-band. A statistically significant difference is observed between Class 0 and Class I disk masses, with the median disk mass being more than a factor of two higher for Class 0 protostars (median dust mass 248 $M_{\oplus}$ in Class 0). By the Class II phase, the median disk dust mass has dropped by an order of magnitude. This result suggests that protoplanetary disks have their highest masses at early times—with a dust mass reservoir sufficient to form giant planet cores—and that grains can grow rapidly in the embedded phase. The C-band contribution lowers between 8 mm and 1 cm, while the measured disk mass is not significantly changed.

The authors thank the anonymous referee, whose comments enhanced the quality of the manuscript. The authors wish to thank Y. Shirley and J. Mottram for sharing data from their previous works, and G. Anglada for insightful comments on the draft. Ł.T. thanks S. van Terwisga and A. Bosman for stimulating discussions. Astrochemistry in Leiden is supported by the Netherlands Research School for Astronomy (NOVA), by a Royal Netherlands Academy of Arts and Sciences (KNAW) professor prize, and by the European Union A-ERC grant 291141 CHEMPLAN. Ł.T. is supported by the Leiden/ESA Astrophysics Program for Summer Students (LEAPS). J.J.T. acknowledges support from the Homer L. Dodge endowed chair, and J.J.T. and Ł.T. acknowledge support from grant 639.041.439 from the Netherlands Organisation for Scientific Research (NWO). J.J.T. acknowledges past support provided by NASA through Hubble Fellowship grant #*HST*-HF-51300.01-A awarded by the Space Telescope Science Institute, which is operated by the Association of Universities for Research in Astronomy, Inc., for NASA, under contract NAS 5-26555. A.K. acknowledges support from the Polish National Science Center grant 2016/21/D/ST9/01098. Ł.T. and A.K. acknowledge support from the HECOLS International Associated Laboratory, supported in part by the Polish NCN grant DEC-2013/08/M/ST9/00664. Z.Y.L. is supported in part by NASA NNX 14AB38G, NSF AST-1313083 and AST-1716259. The National Radio Astronomy Observatory is a facility of the National Science Foundation operated under cooperative agreement by Associated Universities, Inc. This research made use of NASA's Astrophysics Data System.

Facility: VLA.

Software: Astropy (Astropy Collaboration et al. 2013), APLpy (Robitaille & Bressert 2012), Matplotlib (Hunter 2007), MPFIT (Markwardt 2009), lifelines (Davidson-Pilon 2017), AEGEAN (Hancock et al. 2012), CASA (McMullin et al. 2007), STSDAS, ds9.

Appendix A
Additional Correlations

Figure 16 shows a spectral index plotted against bolometric luminosities, but with upper/lower limits excluded and with four outliers removed: Per-emb-14, EDJ2009-156, SVS13A2, L1448NW.

Figure 17 presents the radio luminosity at 6.4 cm plotted against far-IR line luminosities. The relations at 6.4 cm are similar to those obtained at 4.1 cm.

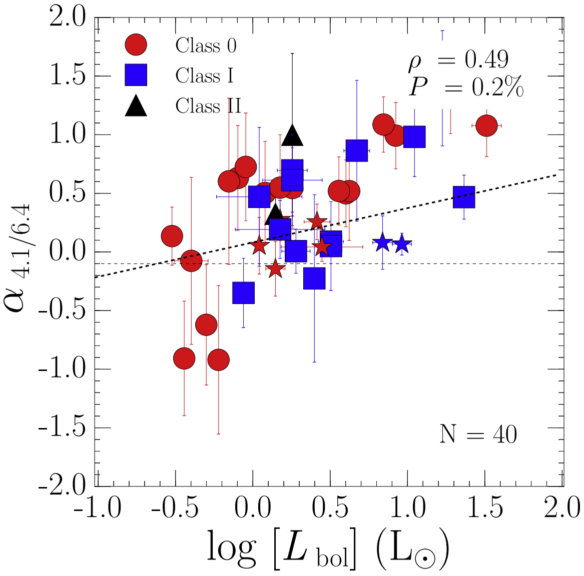

Figure 16. Left: Spectral index compared with bolometric luminosity with four outliers removed: Per-emb-14, EDJ2009-156, SVS13A2, L1448NW. Right: Spectral index compared with bolometric luminosity with upper and lower limits included.

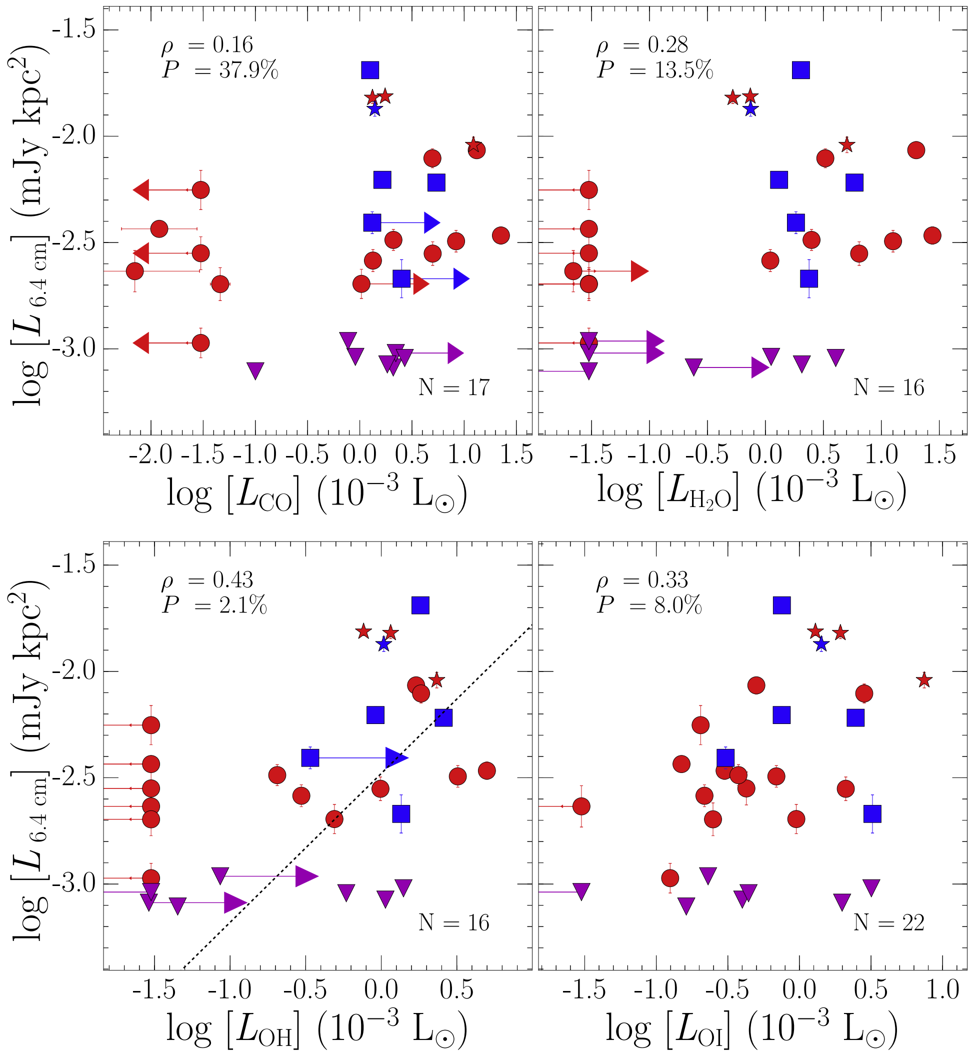

Figure 17. Luminosity at 6.4 cm compared with CO (top left), H_2O (top right), [O I] (bottom left), and OH (bottom right) line luminosities. Upper limits for radio luminosities are plotted as magenta triangles, and lower or upper limits for *Herschel* line luminosities are indicated with arrows. Spearman's rank correlation coefficient and the probability of no correlation are shown in the right top corner (for combined sample of Class 0 and Class I protostars).

Appendix B
Interesting Sources

We note the serendipitous detection of a few intriguing sources in the C-band observations, although they do not have a protostellar nature. The source SVS3—also known as IRAS 03260-3111—is a visible star illuminating the surrounding cloud. It is actually a binary first reported as such by Connelley et al. (2008). In C-band observations, we clearly see both components, with SVS3-B being the brighter of the two (Figure 18). SVS3-A was well-detected with Ka-band observations (Tobin et al. 2016) with negative spectral index. It appears to have a negative spectral index in C-band observations as well. Taken together, these factors point to this star probably being a bright synchrotron source originating from coronal activity, characteristic of more evolved sources; this is also supported by X-ray detection (Preibisch 1997; Getman et al. 2002). SVS3-B was not detected in the Ka-band observations, indicating that there is very little dust present in this component. Free–free emission associated with the source appears spherical and resolved, consistent with ionized wind from the evolved, luminous star.

Source BD +30 547 is a visible star with strong variability detected previously (Rodríguez et al. 1999). It also appears variable in our observations. We note a potential transient source appearing about 1″ north–west away from BD +30 547 in only one of the maps, from the five fields available (Figure 19).

We detect source 2MASS J03293053+3127280, which was reported previously as a brown dwarf (Wilking et al. 2004). Extremely low bolometric luminosity of this source 0.001 $L_\odot$ makes explanation of the emission difficult. The source has a positive spectral index, excluding the possibility of coronal activity, and pointing instead at a surprisingly powerful stellar wind from a brown dwarf. Recently, Rodríguez et al. (2017) have reported the detection of brown dwarfs with radio fluxes an order of magnitude more powerful than expected.

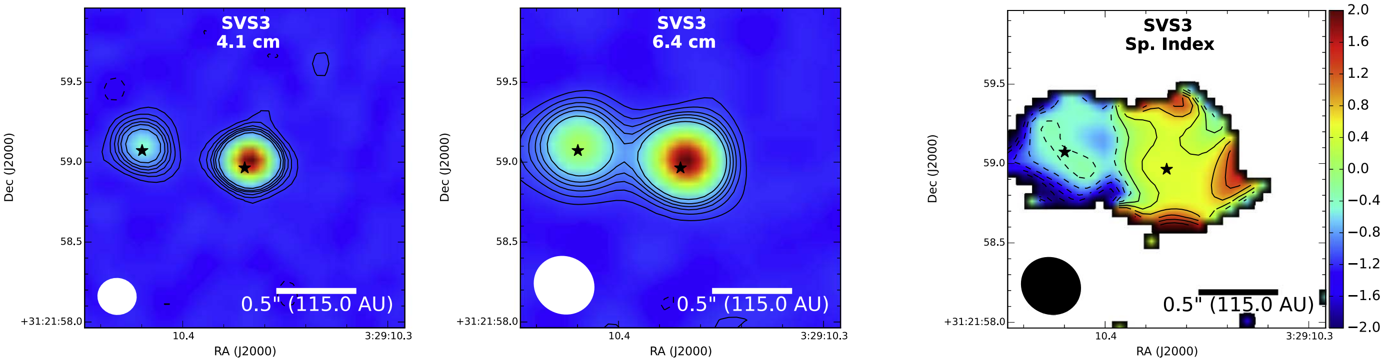

Figure 18. Maps of SVS3 system centered on a SVS3-B component. From left to right: 4.1 cm, 6.4 cm, and spectral index map.

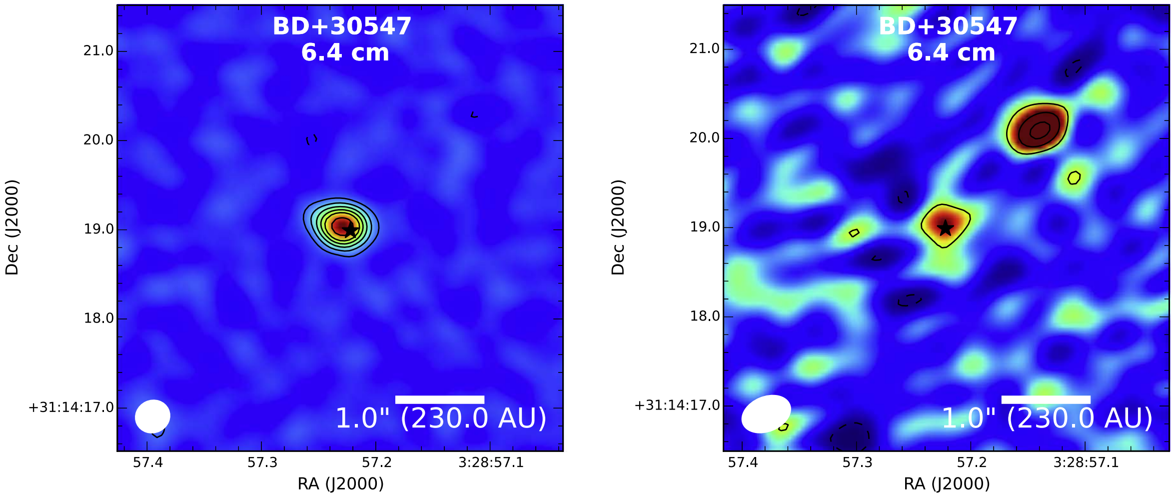

Figure 19. BD+30 547 maps at 6.4 cm from two different epochs. A significant decrease in brightness of the central source can be observed, as well as the appearance of a new source of emission north-west of the BD+30 547.

Appendix C
Free–Free and Dust Slopes

Figure 20 shows the radio spectra for all of the sources from the VANDAM survey. Linear fit to the logarithmic fluxes, applied free–free correction to the dust flux, and the flag used when considering the protostellar disk mass are shown as described in Section 5.

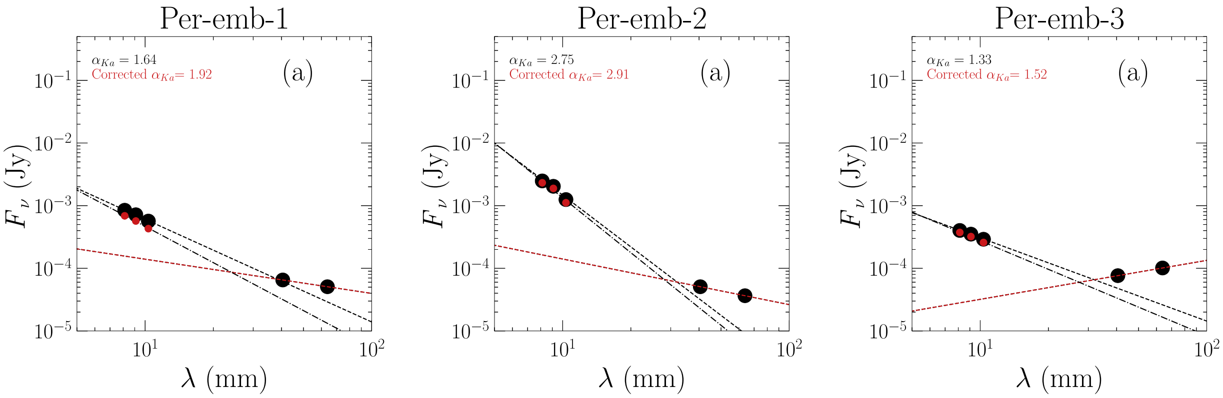

Figure 20. Radio spectral energy distributions for all protostars in VANDAM survey. Black bullets represent Ka-band and C-band flux densities, and triangles are upper limits. Red bullets mark the corrected Ka-band flux densities. Dotted lines are linear fits to the original data, and the red line represents the function from which the free–free contribution was estimated. Dashed–dotted line marks fit to the corrected Ka-band flux densities. Labels a–e indicate a different case of correcting Ka-band data for free–free contamination. All the spectra are available in the Figure Set.

(The complete figure set (137 images) is available.)

Appendix D
Protostars of the VANDAM Survey in Ka-band and C-band

Here, we present the images of all protostars targeted in the VANDAM survey. Figure 21 shows four images of each protostar obtained in the Ka-band (0.8 and 1.0 cm) and in the C-band (4.1 and 6.4 cm).

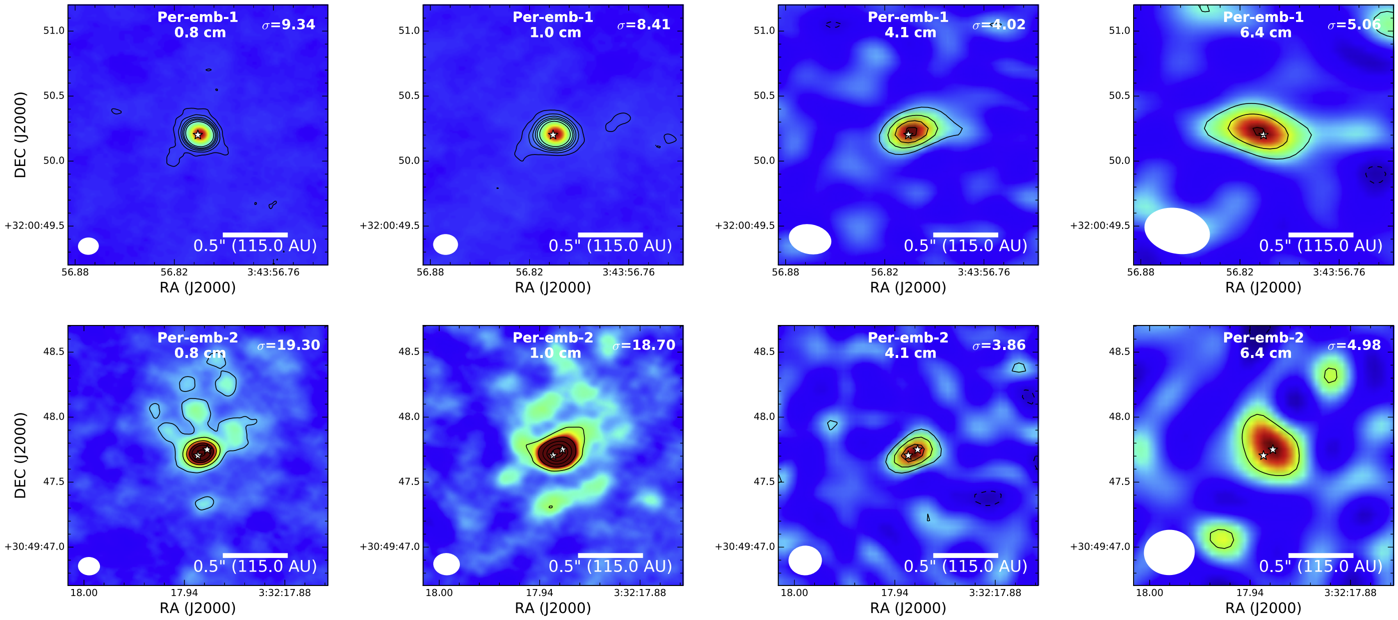

Figure 21. Images of all protostars targeted by both Ka-band (0.8 and 1.0 cm) and C-band (4.1 and 6.4 cm) observations with increasing wavelength from left to right. The contours are [−3, 3, 6, 9, 12, 15, 20] × σ where σ in mJy for each map is provided in the top-right corner.

(The complete figure set (97 images) is available.)

ORCID iDs

Łukasz Tychoniec https://orcid.org/0000-0002-9470-2358
John J. Tobin https://orcid.org/0000-0002-6195-0152
Agata Karska https://orcid.org/0000-0001-8913-925X
Claire Chandler https://orcid.org/0000-0002-7570-5596
Michael M. Dunham https://orcid.org/0000-0003-0749-9505
Kaitlin M. Kratter https://orcid.org/0000-0001-5253-1338
Leslie W. Looney https://orcid.org/0000-0002-4540-6587
Carl Melis https://orcid.org/0000-0001-9834-7579
Laura M. Pérez https://orcid.org/0000-0002-1199-9564
Sarah I. Sadavoy https://orcid.org/0000-0001-7474-6874
Dominique Segura-Cox https://orcid.org/0000-0003-3172-6763
Ewine F. van Dishoeck https://orcid.org/0000-0001-7591-1907

References

AMI Consortium, Scaife, A. M. M., Buckle, J. V., Ainsworth, R. E., et al. 2012, MNRAS, 420, 3334
AMI Consortium, Scaife, A. M. M., Hatchell, J., Davies, M., et al. 2011, MNRAS, 415, 893
Andrews, S. M., Rosenfeld, K. A., Kraus, A. L., & Wilner, D. J. 2013, ApJ, 771, 129
Andrews, S. M., & Williams, J. P. 2005, ApJ, 631, 1134
Andrews, S. M., Wilner, D. J., Hughes, A. M., Qi, C., & Dullemond, C. P. 2009, ApJ, 700, 1502
Anglada, G. 1995, RMxAC, 1, 67
Anglada, G., & Rodríguez, L. F. 2002, RMxAA, 38, 13
Anglada, G., Villuendas, E., Estalella, R., et al. 1998, AJ, 116, 2953
Ansdell, M., Williams, J. P., Manara, C. F., et al. 2017, AJ, 153, 240
Ansdell, M., Williams, J. P., van der Marel, N., et al. 2016, ApJ, 828, 46
Arce, H. G., & Sargent, A. I. 2006, ApJ, 646, 1070
Aspin, C., Sandell, G., & Russell, A. P. G. 1994, A&AS, 106, 165
Astropy Collaboration, Robitaille, T. P., Tollerud, E. J., et al. 2013, A&A, 558, A33
Bachiller, R., Martin-Pintado, J., Tafalla, M., Cernicharo, J., & Lazareff, B. 1990, A&A, 231, 174
Barenfeld, S. A., Carpenter, J. M., Ricci, L., & Isella, A. 2016, ApJ, 827, 142
Bontemps, S., Andre, P., Terebey, S., & Cabrit, S. 1996, A&A, 311, 858
Cabrit, S., & Bertout, C. 1992, A&A, 261, 274
Carrasco-González, C., Rodríguez, L. F., Anglada, G., et al. 2010, Sci, 330, 1209
Chen, X., Arce, H. G., Zhang, Q., et al. 2010, ApJ, 715, 1344
Chiang, H.-F., Looney, L. W., & Tobin, J. J. 2012, ApJ, 756, 168
Choi, M. 2009, ApJ, 705, 1730
Condon, J. J. 1984, ApJ, 287, 461
Condon, J. J., Cotton, W. D., Greisen, E. W., et al. 1998, AJ, 115, 1693
Connelley, M. S., Reipurth, B., & Tokunaga, A. T. 2008, AJ, 135, 2496
Cox, E. G., Harris, R. J., Looney, L. W., et al. 2015, ApJL, 814, L28
Curiel, S., Rodríguez, L. F., Bohigas, J., et al. 1989, ApL&C, 27, 299
Curiel, S., Rodríguez, L. F., Moran, J. M., & Canto, J. 1993, ApJ, 415, 191
Cutri, R. M., Skrutskie, M. F., van Dyk, S., et al. 2003, yCat, 2246
Davidson-Pilon, C. 2017, CamDavidsonPilon/lifelines: 0.11.1, Zenodo, doi:10.5281/zenodo.815943
Davis, C. J., Scholz, P., Lucas, P., Smith, M. D., & Adamson, A. 2008, MNRAS, 387, 954
Dionatos, O., & Güdel, M. 2017, A&A, 597, A64
Draine, B. T. 2006, ApJ, 636, 1114
Draine, B. T., Roberge, W. G., & Dalgarno, A. 1983, ApJ, 264, 485
Dunham, M. M., Vorobyov, E. I., & Arce, H. G. 2014, MNRAS, 444, 887
Dzib, S. A., Loinard, L., Mioduszewski, A. J., et al. 2013, ApJ, 775, 63
Dzib, S. A., Loinard, L., Rodríguez, L. F., et al. 2015, ApJ, 801, 91
Eiroa, C., Torrelles, J. M., Curiel, S., & Djupvik, A. A. 2005, AJ, 130, 643
Enoch, M. L., Corder, S., Duchêne, G., et al. 2011, ApJS, 195, 21
Enoch, M. L., Evans, N. J., II, Sargent, A. I., & Glenn, J. 2009, ApJ, 692, 973
Enoch, M. L., Lee, J.-E., Harvey, P., Dunham, M. M., & Schnee, S. 2010, ApJL, 722, L33
Enoch, M. L., Young, K. E., Glenn, J., et al. 2006, ApJ, 638, 293
Evans, N. J., II, Dunham, M. M., Jørgensen, J. K., et al. 2009, ApJS, 181, 321
Fischer, W. J., Megeath, S. T., Furlan, E., et al. 2017, ApJ, 840, 69
Forbrich, J., Osten, R. A., & Wolk, S. J. 2011, ApJ, 736, 25
Frank, A., Ray, T. P., Cabrit, S., et al. 2014, in Protostars and Planets VI, ed. H. Beuther et al. (Tucscon, AZ: Univ. of Arizona Press), 451
Furuya, R. S., Kitamura, Y., Wootten, A., Claussen, M. J., & Kawabe, R. 2003, ApJS, 144, 71
Galván-Madrid, R., Rodríguez, L. F., Liu, H. B., et al. 2015, ApJL, 806, L32
Gerin, M., Pety, J., Fuente, A., et al. 2015, A&A, 577, L2
Getman, K. V., Feigelson, E. D., Townsley, L., et al. 2002, ApJ, 575, 354
Ghavamian, P., & Hartigan, P. 1998, ApJ, 501, 687
Girart, J. M., Curiel, S., Rodríguez, L. F., & Cantó, J. 2002, RMxAA, 38, 169
Green, J. D., Evans, N. J., II, Jørgensen, J. K., et al. 2013, ApJ, 770, 123
Gutermuth, R. A., Myers, P. C., Megeath, S. T., et al. 2008, ApJ, 674, 336
Hancock, P. J., Murphy, T., Gaensler, B. M., Hopkins, A., & Curran, J. R. 2012, MNRAS, 422, 1812
Hatchell, J., Fuller, G. A., & Richer, J. S. 2007, A&A, 472, 187
Hildebrand, R. H. 1983, QJRAS, 24, 267
Hirano, N., Ho, P. P. T., Liu, S.-Y., et al. 2010, ApJ, 717, 58
Hirano, N., Kamazaki, T., Mikami, H., Ohashi, N., & Umemoto, T. 1999, in Star Formation 1999, ed. T. Nakamoto (Nobeyama Radio Observatory), 181
Hirota, T., Honma, M., Imai, H., et al. 2011, PASJ, 63, 1
Hollenbach, D., & McKee, C. F. 1989, ApJ, 342, 306
Hull, C. L. H., Girart, J. M., Kristensen, L. E., et al. 2016, ApJL, 823, L27
Hunter, J. D. 2007, CSE, 9, 90
Isobe, T., Feigelson, E. D., & Nelson, P. I. 1986, ApJ, 306, 490
Jørgensen, J. K., van Dishoeck, E. F., Visser, R., et al. 2009, A&A, 507, 861
Karska, A., Herczeg, G. J., van Dishoeck, E. F., et al. 2013, A&A, 552, A141
Karska, A., Kaufman, M. J., Kristensen, L. E., et al. 2018, ApJS, 235, 30
Karska, A., Kristensen, L. E., van Dishoeck, E. F., et al. 2014, A&A, 572, A9
Kirk, H., Johnstone, D., & Tafalla, M. 2007, ApJ, 668, 1042
Kukarkin, B. V., Kholopov, P. N., Pskovsky, Y. P., et al. 1971, General Catalogue of Variable Stars (3rd ed.; Moscow: Moskva)
Kwon, W., Looney, L. W., Mundy, L. G., Chiang, H.-F., & Kemball, A. J. 2009, ApJ, 696, 841
Ladd, E. F., Myers, P. C., & Goodman, A. A. 1994, ApJ, 433, 117
Luhman, K. L., Rieke, G. H., Lada, C. J., & Lada, E. A. 1998, ApJ, 508, 347
Machida, M. N. 2014, ApJL, 796, L17
Manoj, P., Green, J. D., Megeath, S. T., et al. 2016, ApJ, 831, 69
Manoj, P., Watson, D. M., Neufeld, D. A., et al. 2013, ApJ, 763, 83
Markwardt, C. B. 2009, in ASP Conf. Ser. 411, Astronomical Data Analysis Software and Systems XVIII, ed. D. A. Bohlender, D. Durand, & P. Dowler (San Francisco, CA: ASP), 251
McMullin, J. P., Waters, B., Schiebel, D., Young, W., & Golap, K. 2007, in ASP Conf. Ser. 376, Astronomical Data Analysis Software and Systems XVI, ed. R. A. Shaw, F. Hill, & D. J. Bell (San Francisco, CA: ASP), 127
Miotello, A., Testi, L., Lodato, G., et al. 2014, A&A, 567, A32
Morata, O., Palau, A., González, R. F., et al. 2015, ApJ, 807, 55
Mottram, J. C., Kristensen, L. E., van Dishoeck, E. F., et al. 2014, A&A, 572, A21
Mottram, J. C., van Dishoeck, E. F., Kristensen, L. E., et al. 2017, A&A, 600, A99
Murillo, N. M., van Dishoeck, E. F., Tobin, J. J., & Fedele, D. 2016, A&A, 592, A56
Natta, A., Grinin, V., & Mannings, V. 2000, in Protostars and Planets IV (Tucson, AZ: Univ. of Arizona Press), 559
Neufeld, D. A., & Dalgarno, A. 1989, ApJ, 340, 869
Nisini, B., Giannini, T., & Lorenzetti, D. 2002, ApJ, 574, 246
Nisini, B., Santangelo, G., Giannini, T., et al. 2015, ApJ, 801, 121
Oasa, Y., Tamura, M., Sunada, K., & Sugitani, K. 2008, AJ, 136, 1372
Offner, S. S. R., & Arce, H. G. 2014, ApJ, 784, 61
Ossenkopf, V., & Henning, T. 1994, A&A, 291, 943
Panagia, N., & Felli, M. 1975, A&A, 39, 1
Pascucci, I., Testi, L., Herczeg, G. J., et al. 2016, ApJ, 831, 125
Pech, G., Loinard, L., Dzib, S. A., et al. 2016, ApJ, 818, 116
Perley, R. A., & Butler, B. J. 2017, ApJS, 230, 7
Pezzuto, S., Elia, D., Schisano, E., et al. 2012, A&A, 547, A54
Pilbratt, G. L., Riedinger, J. R., Passvogel, T., et al. 2010, A&A, 518, L1
Pineda, J. E., Arce, H. G., Schnee, S., et al. 2011, ApJ, 743, 201
Poglitsch, A., Waelkens, C., Geis, N., et al. 2010, A&A, 518, L2
Preibisch, T. 1997, A&A, 324, 690
Preibisch, T., Stanke, T., & Zinnecker, H. 2003, A&A, 409, 147
Preibisch, T., & Zinnecker, H. 2001, AJ, 122, 866
Reipurth, B., Rodríguez, L. F., Anglada, G., & Bally, J. 2004, AJ, 127, 1736
Reynolds, S. P. 1986, ApJ, 304, 713
Robitaille, T., & Bressert, E. 2012, APLpy: Astronomical Plotting Library in Python, Astrophysics Source Code Library, ascl:1208.017

Rodríguez, L. F., Anglada, G., & Curiel, S. 1997, ApJL, 480, L125
Rodríguez, L. F., Anglada, G., & Curiel, S. 1999, ApJS, 125, 427
Rodríguez, L. F., Curiel, S., Moran, J. M., et al. 1989a, ApJL, 346, L85
Rodríguez, L. F., Marti, J., Canto, J., Moran, J. M., & Curiel, S. 1993, RMxAA, 25, 23
Rodríguez, L. F., Myers, P. C., Cruz-Gonzalez, I., & Terebey, S. 1989b, ApJ, 347, 461
Rodríguez, L. F., Porras, A., Claussen, M. J., et al. 2003, ApJL, 586, L137
Rodríguez, L. F., & Reipurth, B. 1989, RMxAA, 17, 59
Rodríguez, L. F., & Reipurth, B. 1998, RMxAA, 34, 13
Rodríguez, L. F., Zapata, L. A., & Palau, A. 2014, ApJ, 790, 80
Rodríguez, L. F., Zapata, L. A., & Palau, A. 2017, AJ, 153, 209
Rybicki, G. B., & Lightman, A. P. 1979, Radiative Processes in Astrophysics (New York: Wiley-Interscience)
Sadavoy, S. I., Di Francesco, J., André, P., et al. 2014, ApJL, 787, L18
San José-García, I., Mottram, J. C., Kristensen, L. E., et al. 2013, A&A, 553, A125
Schnee, S., Di Francesco, J., Enoch, M., et al. 2012, ApJ, 745, 18
Segura-Cox, D. M., Harris, R. J., Tobin, J. J., et al. 2016, ApJL, 817, L14
Sheehan, P. D., & Eisner, J. A. 2017, ApJ, 851, 45
Shirley, Y. L., Claussen, M. J., Bourke, T. L., Young, C. H., & Blake, G. A. 2007, ApJ, 667, 329
Shu, F., Najita, J., Ostriker, E., et al. 1994, ApJ, 429, 781
Strom, S. E., Vrba, F. J., & Strom, K. M. 1976, AJ, 81, 314
Tafalla, M., Santiago, J., Johnstone, D., & Bachiller, R. 2004, A&A, 423, L21
Testi, L., Birnstiel, T., Ricci, L., et al. 2014, in Protostars and Planets VI, ed. H. Beuther et al. (Tucson, AZ: Univ. of Arizona Press), 339
Tobin, J. J., Dunham, M. M., Looney, L. W., et al. 2015a, ApJ, 798, 61
Tobin, J. J., Looney, L. W., Wilner, D. J., et al. 2015b, ApJ, 805, 125
Tobin, J. J., Looney, L. W., Li, Z.-Y., et al. 2016, ApJ, 818, 73
Tychoniec, Ł., Tobin, J. J., Karska, A., et al. 2018, ApJ, 852, 18
van der Marel, N., Kristensen, L. E., Visser, R., et al. 2013, A&A, 556, A76
van Dishoeck, E. F., Kristensen, L. E., Benz, A. O., et al. 2011, PASP, 123, 138
van Kempen, T. A., Kristensen, L. E., Herczeg, G. J., et al. 2010, A&A, 518, L121
Visser, R., van Dishoeck, E. F., & Black, J. H. 2009, A&A, 503, 323
Wampfler, S. F., Bruderer, S., Karska, A., et al. 2013, A&A, 552, A56
Whitney, B. A., Wood, K., Bjorkman, J. E., & Cohen, M. 2003, ApJ, 598, 1079
Wilking, B. A., Meyer, M. R., Greene, T. P., Mikhail, A., & Carlson, G. 2004, AJ, 127, 1131
Williams, J. P., & Cieza, L. A. 2011, ARA&A, 49, 67
Winston, E., Megeath, S. T., Wolk, S. J., et al. 2010, AJ, 140, 266
Wu, Y., Wei, Y., Zhao, M., et al. 2004, A&A, 426, 503
Yıldız, U. A., Kristensen, L. E., van Dishoeck, E. F., et al. 2015, A&A, 576, A109
Young, C. H., Jørgensen, J. K., Shirley, Y. L., et al. 2004, ApJS, 154, 396
Young, K. E., Young, C. H., Lai, S.-P., Dunham, M. M., & Evans, N. J., II 2015, AJ, 150, 40